Functionalized inorganic liquid crystals

Doctoral Thesis

submitted to obtain the academic degree of Doctor of Natural Sciences
(Dr. rer. nat.)
of the Faculty of Biology, Chemistry & Earth Sciences
of the University of Bayreuth

Olena Khoruzhenko
from Horishni Plavni
Bayreuth, 2023

This doctoral thesis was prepared at the Department of *Inorganic Colloids for Electrochemistry Energy Storage* at the University of Bayreuth from (09/2019) until (05/2023) and was supervised by Prof. Dr. Josef Breu.

This is a full reprint of the thesis submitted to obtain the academic degree of Doctor of Natural Sciences (Dr. rer. nat.) and approved by the Faculty of Biology, Chemistry and Geosciences of the University of Bayreuth.

Form of the thesis: Cumulative thesis

Date of submission: 11.05.2023

Date of defence: 14.12.2023

Acting director: Prof. Dr. Cyrus Samimi

Doctoral committee:

Prof. Dr. Josef Breu	(reviewer)
Prof. Dr. Jürgen Senker	(reviewer)
Prof. Dr. Anna Schenk	(chair)
JProf. Dr. Meike Leiske	

TABLE OF CONTENTS

TABLE OF CONTENTS

LIST OF ABBREVIATIONS

2D	Two-dimensional
VdW	Van der Waals
CEC	Cation-exchange capacity
PXRD	Powder X-ray diffraction
Å	Angstrem 10^{-10} m
1D	One-dimensional
OI	Ordered interstratifications
pKa	Acid dissociation constant
LC	Liquid crystals
NP	Nanoparticles
BT	Blocking temperature
SPM	Superparamagnetism
OD	Zero-dimensional
DS	Double stacks
MDS	Magnetic double stacks
IR	Infra-red
NIR	Near infrared
AFM	Atomic Force Microscope
BET	Brunauer–Emmett–Teller
TEM	Transmission electron microscopy
SAXS	Small angle X-ray scattering
PNIPAm	Poly(N-isopropylacrylamide)
UV	Ultra-violet
LCST	Lower critical solution temperature
AuDS	Gold double stacks
DMAP	4-Dimethylaminopyridine
TOAB	Tetraoctylammonium bromide
LSPR	Localized Surface Plasmon Resonance

SUMMARY

Making dynamic, yet functional structures is challenging. In this thesis, we evoke the liquid crystalline properties of hectorite and the ability to form ordered interstratification structures to add additional functional properties to the liquid crystal using the functional 0D particles. We have added the magnetic and the light-conversion properties to the hectorite liquid crystal. We utilized anisotropy of 2D nanosheets and translate it to OD isotropic nanoparticles. The whole liquid crystalline system acquires functional properties of nanoparticles and preserves anisotropy from hectorite nanosheets Resulting nanosheets was used in different forms for practical application from hydrogel to coating.

The first paper describes the fabrication of anisotropic magnetic liquid crystals by combining fluorohectorite with maghemite nanoparticles. The fluorohectorite is a unique material due to its charge homogeneity and aspect ratio, which allows for ordered interstratification of Na^+ and NH_4^+ layers. Maghemite nanoparticles are intercalated between the layers of fluorohectorite, creating a magnetic double stack (MDS). The MDS exhibits liquid crystalline behavior and can be oriented perpendicular or parallel to an incoming magnetic field. The properties of the MDS are dependent on the NPs loading and their response to magnetic fields is direction-dependent. The resulting ferronematic suspension is stable in water and exhibits a highly anisotropic magnetic response that can be tuned by adjusting the starting ratio of components. Overall, this method provides a simple way to create anisotropic nanosheet-shaped colloids with adjustable interparticle interaction and magnetic properties.

In the next publication, we highlight the application of the MDS in hydrogel, where they offer the anisotropic mechanical properties and fast magnetic responsiveness. We developed anisotropic hydrogels using concepts inspired by biological tissues. We achieved this by aligning polymer chains or inorganic fillers into ordered structures within soft matrices using magnetic fields. The alignment of the MDS in the hydrogel was achieved using a static and rotating magnetic field. Hydrogels with highly ordered MDSs possess unique anisotropic optical and mechanical properties and exhibit anisotropic responses to changes in temperature. The hydrogels are useful in designing functional materials and soft actuators with versatile applications, and they exhibit multi-gait motions steered by light and magnetic fields. The combination of

various stimulus-response properties of the hydrogels has the potential to enhance the design and management of soft actuators and robots for specific applications.

Finally, the last paper focuses on the development of a wet colloid chemistry-based method to fabricate thin, transparent coatings with anisotropic heat conductivity. The coatings were made using a liquid crystalline, electrostatically stabilized suspension of DS structures with spherical gold nanoparticles sandwiched between two dielectric 1 nm thick silicate nanosheets (AuDS). The AuDS structures were deposited on a planar substrate, adopting a defined orientation to the surface and yielding anisotropic heat conductivity. The absorbance of the metasurface is tunable by modulating plasmonic coupling via a variation of nanoparticle loading. These coatings allow for fast defogging and defrosting under solar irradiation.

ZUSAMMENFASSUNG

Die Herstellung dynamischer, aber funktioneller Strukturen ist eine Herausforderung. In dieser Arbeit nutzen wir die flüssigkristallinen Eigenschaften von Hectorit und dessen Fähigkeit, geordnete Interstratifikationsstrukturen zu bilden, um dem Flüssigkristall mit Hilfe der funktionellen 0D-Partikel zusätzliche funktionelle Eigenschaften zu verleihen. Wir haben dem Hectorit-Flüssigkristall die magnetischen und die Lichtumwandlungseigenschaften hinzugefügt. Wir haben die Anisotropie von 2D-Nanoblättern genutzt und sie auf isotrope 0D-Nanopartikel übertragen. Das gesamte flüssigkristalline System erwirbt die funktionellen Eigenschaften von Nanopartikeln und bewahrt die Anisotropie von Hectorit-Nanoblättern. Die resultierenden Nanoblätter wurden in verschiedenen Formen für praktische Anwendungen von Hydrogelen bis hin zu Beschichtungen verwendet.

Die erste Arbeit beschreibt die Herstellung anisotroper, magnetischer Flüssigkristalle durch die Kombination von Fluorohectorit mit Maghemit-Nanopartikeln. Fluorohectorit ist aufgrund seiner Ladungshomogenität und seines Aspektverhältnisses, das eine geordnete Schichtung von Na^+- und NH_4^+-Schichten ermöglicht, ein einzigartiges Material. Meghemit-Nanopartikel sind zwischen den Fluorohectorit-Schichten eingelagert, wodurch magnetische Nanoblätter in Sandwichbauweise entstehen. Die MDS weisen ein LC-Verhalten auf und können senkrecht oder parallel zu einem einfallenden Magnetfeld ausgerichtet werden. Die Eigenschaften der MDS sind abhängig von der NP-Beladung und ihre Reaktion auf Magnetfelder ist richtungsabhängig. Die resultierende ferronematische Suspension ist in Wasser stabil und zeigt eine stark anisotrope magnetische Reaktion, die durch Anpassung des Ausgangsverhältnisses der Komponenten eingestellt werden kann. Insgesamt bietet diese Methode eine einfache Möglichkeit zur Herstellung anisotroper nanoblattförmiger Kolloide mit einstellbaren Wechselwirkungen zwischen den Partikeln und magnetischen Eigenschaften.

In der nächsten Veröffentlichung wird die Anwendung der MDS in Hydrogelen hervorgehoben, wo sie anisotrope mechanische Eigenschaften und eine schnelle magnetische Reaktionsfähigkeit bieten. Wir haben anisotrope Hydrogele entwickelt, wobei wir uns von Konzepten biologischer Gewebe inspirieren ließen. Wir erreichten dies, indem wir Polymerketten oder anorganische Füllstoffe mit Hilfe von Magnetfeldern zu geordneten Strukturen in weichen Matrizen ausrichteten. Die

Ausrichtung der MDS in den Hydrogelen wurde durch ein statisches und ein rotierendes Magnetfeld erreicht. Hydrogele mit hoch geordneten MDS besitzen einzigartige anisotrope optische und mechanische Eigenschaften und zeigen anisotrope Reaktionen auf Temperaturänderungen. Die Hydrogele sind nützlich für die Entwicklung funktioneller Materialien und weicher Aktuatoren mit vielseitigen Anwendungsmöglichkeiten und zeigen durch Licht und Magnetfelder gesteuerte Bewegungen. Die Kombination verschiedener Reiz-Reaktions-Eigenschaften der Hydrogele hat das Potenzial, den Entwurf und das Management von weichen Aktoren und Robotern für spezifische Anwendungen zu verbessern.

Der letzte Beitrag schließlich befasst sich mit der Entwicklung einer auf der Nasskolloidchemie basierenden Methode zur Herstellung dünner, transparenter Beschichtungen mit anisotroper Wärmeleitfähigkeit. Die Beschichtungen werden aus einer flüssigkristallinen, elektrostatisch stabilisierten Suspension von Doppelstapelstrukturen hergestellt, die aus kugelförmigen Goldnanopartikeln bestehen, die zwischen zwei dielektrischen 1 nm dicken Silikat-Nanoblättern liegen. Die DS-Strukturen sind auf einem ebenen Substrat in einer bestimmten Ausrichtung angeordnet, um eine anisotrope Wärmeleitfähigkeit zu erzielen, ohne dass eine strukturierte Oberfläche erforderlich ist. Die Absorption der Meta-Oberfläche ist durch Modulation der plasmonischen Kopplung über eine Variation der Nanopartikelladung einstellbar. Diese Beschichtungen ermöglichen eine schnelle Entnebelung und Entfrosten unter NIR-Bestrahlung.

INTRODUCTION

2D MATERIALS

Layered materials are defined by anisotropic chemical bonds in three dimensions. Usually, they have strong in-plane and weak out-of-plane chemical bonds.[1] Classical example of 2D material is graphene, where covalent bonding within the plane of the layer forming sp^2 hybridization network connects carbon atoms.[2] In the out-of-plane direction it is held together only by weak Van der Waals (VdW) attraction. This attraction can be easily overcome by the mild force application, which was shown in the pioneering work of Geim and Novoselov using simple Scotch tape.[3, 4]

The great interest in 2D materials lies in the properties' difference of the single layers from that of the bulk materials.[5, 6] For studying and applying these properties different exfoliation methods were developed, mainly focusing on shearing parallel or expanded normal to the in-plane direction.[7] These methods result in the production of nanometre-thin or even atomically thin sheets. The result of the breaking out-of-plane bonding can lead to two outcomes: complete delamination,[8-10] when the nanosheets have a single-layer structure, and exfoliation when the resulting nanosheets have varying thickness and consist of multilayers.[11]

Within most layered materials such as graphene, molybdenum disulfide (MoS_2), or hexagonal boron nitride (*h*BN), VdW bonds act to hold the layers together in the out-of-plane direction.[12, 13] The weak VdW forces between the layers make it simple to separate them applying mechanical,[7] chemical,[14] or electrochemical forces[15, 16]. This exfoliation process produces individual sheets with a thickness measured in nanometres, revealing a range of distinctive material properties that are not present in the bulk form.[17] However, exfoliation techniques heavily rely on the applied forces, leading to a wide range of defects,[18] low yields,[19] surface functionalization,[20] reduction of lateral sizes,[20] and wide distribution of thicknesses[21].

Unlike the VdW crystals, the layers in ionic-layered solids are held by electrostatic interaction between the charged layers and counterions in the interlayer space. The most widespread examples are layered silicates,[22, 23] layered double hydroxides,[24] titanates of lepidocrite type[25] or niobates of layered Ruddlesden-Popper type oxidic perovskites[26, 27]. Ionic bonds are generally stronger than VdW and different exfoliation methods are required to achieve similar results. Luckily, the electrostatic interaction

can be exploited by reversing the electrostatic attraction to repulsion between the similar charged nanosheets.[28-30]

Another importance difference to VdW crystals is the presence of relatively high mobility interlayer ion, which can be exchanged by simple ion-exchange reaction. This reaction changes the reactivity of the interlayer space.[22, 31]

LAYERED SILICATES

The most widespread examples of ionic-layered solids are layered silicates. Layered silicates of the 2:1 family with a permanent negative charge, such as smectites, are known for their unique 2D host material properties.[32] They are built in a sandwich-like manner where one octahedral layer is placed between two tetrahedral layers.[33]

Smectite layers have a permanent negative layer charge (0.2-0.6 per half unit cell), due to numerous isomorphic substitutions and vacancies, which are compensated by cations in the interlayer space.[33] The propensity of smectites for sorption of cationic species is given as cation-exchange capacity (CEC).[34] Smectites are well known for the special stepwise fashion of swelling with the formation of interlayer hydrates or solvates, depending on the solvation media.[35]

In this line, such natural abundant and affordable materials should be fruitfully exploited for 2D nanosheets production. Nevertheless, using them as a source for 2D nanosheets still is a non-trivial task. Natural smectites have numerous charge defects caused by non-systematic variation of isomorphous substitution and impurities introduced during the formation of natural clays.[36, 37] Such structural impurities lead to inconsistent intercrystalline reactivity,[38] which limits flawless delamination of smectites into individual nanosheets.

Therefore, controlled synthesis in laboratory conditions is required to produce smectites with a perfect uniform intercrystalline reactivity and homogeneous layer charge.

Synthetic sodium fluorohectorite was produced as a model system of idealized smectite crystal- (Na-hectorite, $[Na_{0.5}]^{inter}[Mg_{2.5}Li_{0.5}]^{oct}[Si_4]^{tet}O_{10}F_2$).

Na-hectorite is synthesized by exploring a combination of melt synthesis with subsequently long-term annealing.[39, 40] The resulting Na-hectorite has high single-phase purity, giant crystal size (20 µm, Fig.1 A to C), homogeneous charge density (0.5 per formula unit), and, as a result - uniform intercrystalline reactivity.

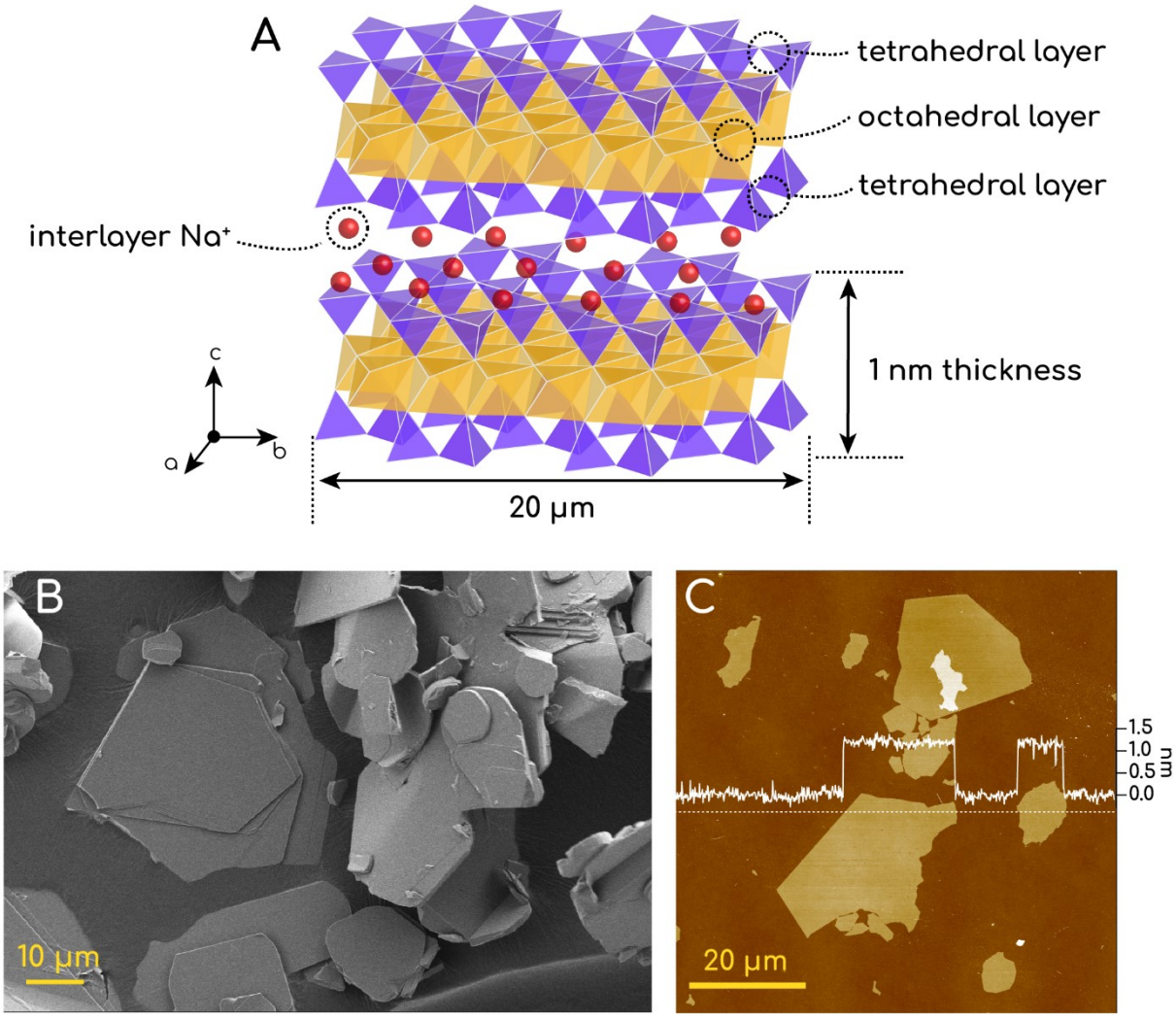

Figure 1 *Synthetic sodium fluorohectorite characterization.* ***(A)*** *Schematic crystallographic structure of sodium hectorite.* ***(B)*** *SEM image of Na-hectorite.* ***(C)*** *AFM of Na-hectorite, showing a thickness of 1 nm.*

Consequently swelling of Na-hectorite occurs in a strict, well-defined fashion with the uniform interlayer separation, which can be easily tracked by PXRD. Swelling of the Na-hectorite has two different regimes.[41] The first one crystalline swelling is characterized by the well-defined d-spacing which occurs in media with low solvent activity,[28, 40] for example in humid air or in solvents with low polarity. During that step, interlayer Na^+ acquires solvation or coordination shell -several water molecules surround every Na^+ in interlayer space. Being solvated, Na^+ increases the separation between basal surfaces (d-spacing changes from 9.6 to 12.4 Å for going from a completely non-hydrated structure to 1 water-layer hydrate). The second regime is called osmotic swelling or 1D dissolution,[8] which is characterized by a less defined separation between the nanosheets and the formation of a diffuse double layer it

happens in media with high solvent activity and high polarity.[42] For example, upon immersing into liquid water, solvent molecules are absorbed beyond the boundaries of crystalline swelling, surpassing a critical threshold of separation leading to the formation of diffused double layer, which overlaps and leads to the electrostatic repulsion. At this point, a repulsive force replaces the attractive interaction between neighboring nanosheets.

At this point, the nanosheets are caught in parallel orientation with respect to each other and are not able to rotate because of the much smaller separation between the nanosheets compare to the diameter of individual nanosheets.[28] Hectorite nanosheets form nematic liquid crystals and the separation between them can be controlled by dilution.[43]

ORDERED INTERSTRATIFICATION

Due to the mobile character of interlayer cations, most natural clays exist in the mixed interlayer state, meaning that within single silicate crystals, multiple different interlayer cations could coexist even within the single interlayer space.[33] Rarer is the case of the alternating interlayer spaces, where different interlayer spaces coexist each consisting of strictly single interlayer cation.[44] Such structures occur in natural clays from 2:1 family such as vermiculate, but they always have a random nature.[45-47]

In order to achieve strictly alternating nanolayers, more complicated approaches are required.[41, 48, 49] Ordered interstratifications (OI) have two explanations, one relies on thermodynamic and the second rely on kinetics (Fig. 2 A). The latter is argued by Lagaly, evoking the negative cooperativeness, meaning that swelling-induced deformation of the silicate lamellae will block the two adjacent interlayers.[47]

In high phase purity and superior charge homogeneity Na-hectorite, ordered interstratifications occur due to thermodynamics with parameters such as CEC% of exchange cation and solvent activity being most influential.[48, 49]

This mechanism describes, that upon formation of the regular interstratification, the charge density of the interlayers changes from homogeneous to alternating interlayer to interlayer in the stacking direction. This simple redistribution of exchangeable interlayer cations is facile and fast. The cation exchange capacity (CEC) of the collapsed interlayers is higher than the average CEC, while the CEC of the hydrated

interlayers will be correspondingly lower.[49] Resulting XRD pattern shows superstructure d-spacing of the two interlayers combined (Fig. 2 B).

After the parameters for OI are found, it can be produced in a facial manner, providing new functionalities to the material.[48, 50-52] One of which is the selective activation of 1D dissolution, assisted by the ion exchange of hydratable cation to nonhydratable.

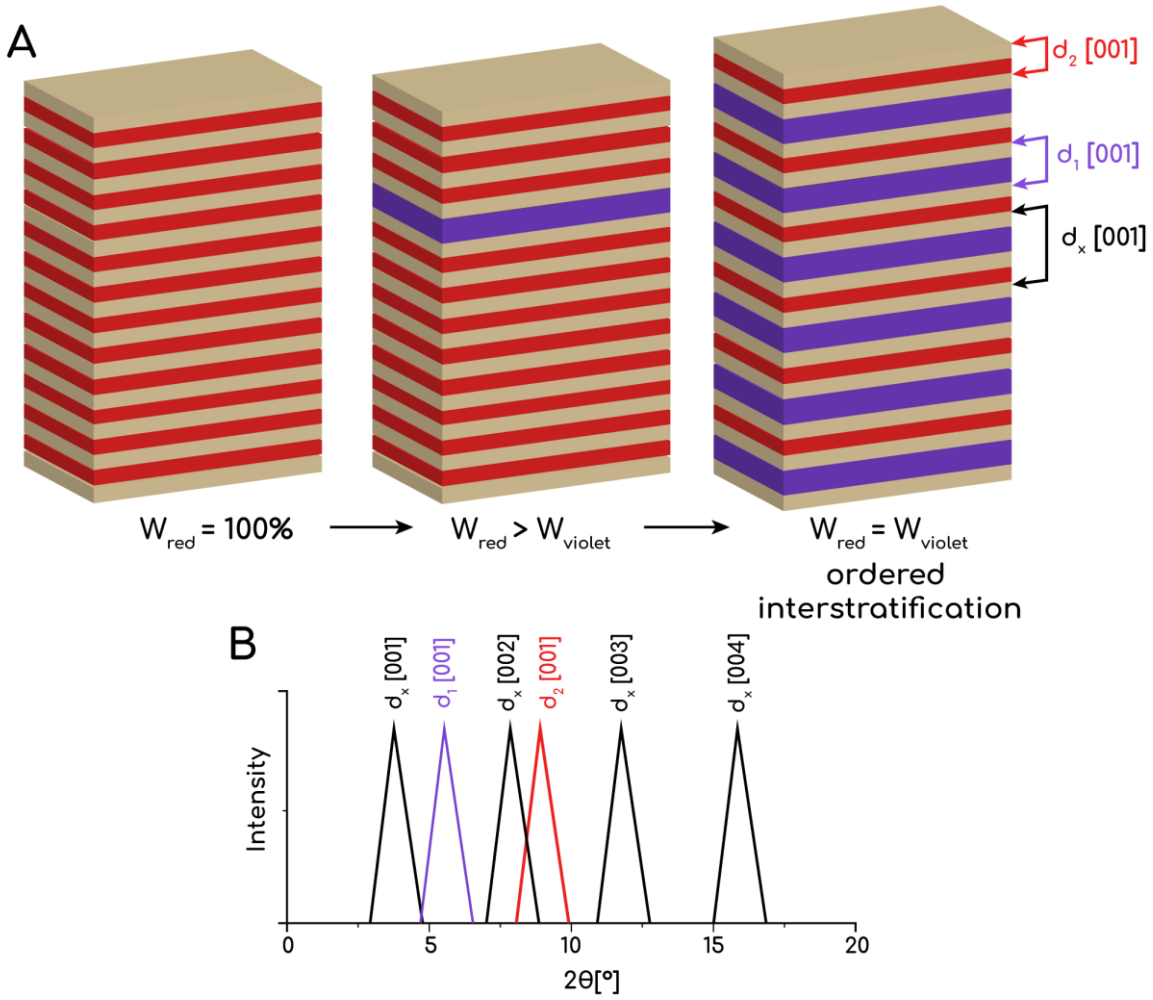

Figure 2 Schematic explaining of ordered interstratification (OI) formation. (A) *Scheme explaining the nucleation of an OI domain by intercalation of a single densely packed interlayer with lower interlayer cation densities into initially homogeneously distributed hydrated Na-interlayers.* ***(B)*** *Schematic XRD pattern of OI in A.*

As an example the Na^+/NH_4^+ OI, where the hydratable Na^+ is alternating with the nonhydratable NH_4^+ cation.[51] Upon immersion into water, such structures instead of delaminating to the single stacks delaminate to the double stacks (DS), where two silicate layers are glued together by NH_4^+ cation.

NH_4^+ has a pKa of 9.5[53] and can be readily deprotonated and subsequently removed from solution by the use of the base, such as LiOH, that offer the highly hydrophilic Li^+ cation.

Such DS can be used to make functional liquid crystals, by first flocculating the double stacks with the positively charged colloids or molecules and immersion of flocculate into LiOH to ensure the ion exchange of NH_4^+ for Li^+.[50, 52, 54, 55]

LIQUID CRYSTALS

Liquid crystals (LCs) have emerged as promising smart materials that are highly responsive to external stimuli, making them attractive for a variety of applications.[56, 57]

While the crystalline phase is characterized by a three-dimensional long-range orientational and positional order,[58] isotropic liquids only show short-range order (Fig.3). This order can greatly affect the directionality of properties, making crystalline phase anisotropic, while liquids are isotropic in most cases.

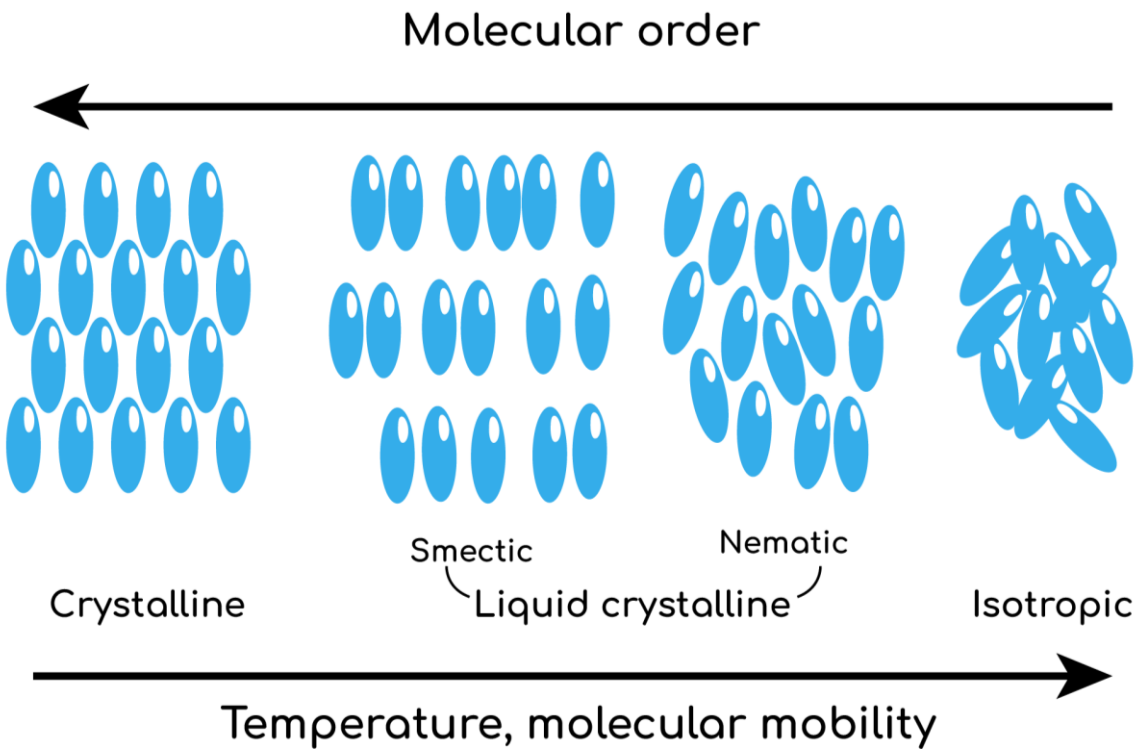

Figure 3. Schematic illustrations of order degree in different states of matter

Liquid crystals stand in between the liquids and crystalline materials. They consist of anisotropic mesogens and their degree of order takes an intermediate place between

the crystalline and the isotropic phases, allowing fluidity and dynamics like isotropic liquids, but still having directional-dependent properties.

LC phase is subdivided into smectic and nematic phases. The nematic phase is characterized by one-dimensional long-range orientational order. In smectic phases, the anisotropic mesogens are additionally oriented in layers and their order degree is higher than the nematic phase. Liquid crystals are often characterized by the nematic director as the vector, which is used for the relative determination of anisotropic properties.[57]

When people refer to the term “LC” in most cases they have in mind rigid organic molecules, which can exist in a liquid crystalline state in a specific temperature range. However, the world of LC is much wider than this.[59]

Another class of LC is based on inorganic materials – 2D nanosheets and 1D nanofibers.[42, 60-62] Particularly, Na-hectorite,[28] being immersed into water, delaminates into individual 2D nanosheets, forming a nematic liquid crystalline phase. This nematic phase saves the liquid crystal character in a wide range of temperatures. It is stabilized by electrostatic repulsion, and similarly to any other anisotropic mesogen, can be controlled by external stimuli.

In order to bring additional functionality, the LC phase is often loaded with NP. Incorporating NPs into liquid crystals LCs is a valuable approach to manipulating their characteristics. Resulting suspensions have notably distinct and potentially enhanced properties compared to the pure materials.[63-68]

Naturally, the alteration of liquid crystals' properties is reliant on the type and intrinsic characteristics of the doped nanoparticles used. For example, adding para- and ferromagnetic particles to nematics, brings specific features, making them a potential option for magnetically tuneable structures.[64, 67, 69-75] LC matrix, in its turn, translates anisotropy from mesogens on the whole LC-NPs system. Furthermore, such suspensions can maintain long-term stability, which is a crucial requirement for their utilization in industrial settings. Moreover, LC matrix allows distributing high loadings of NPs, reaching collective NPs response by controlling the separation between them, simultaneously avoiding Ostwald ripening.

NANOPARTICLES AND THEIR COLLECTIVE PROPERTIES

Nanoparticles (NPs) have unique properties compared to the same material in bulk form. For example, gold in the normal form represents the metallic-yellow material, while in the nano form, the color of gold nanoparticles varies from red to black, depending on the size and shape of the particles.[76-78] Such extreme properties of nanoparticles arise from the size effect, where the size of the particles start to be comparable with the length-scales of quantum effects and from the high surface-to-volume ratio.[79]

Another important feature of the NPs is a collective response. When they are brought close enough together, they can interact with each other, showing properties, different from the intrinsic properties of NPs in the isolated state.[80-82]

For example, when magnetic particles are sufficiently small, they show superparamagnetic collective behavior (SPM) (Fig. 4 A).[83, 84] It occurs in systems composed of a single magnetic domain NPs, without magnetic memory. The formation of domain walls in ferromagnetic materials is controlled by the competition between the energy cost for domain wall formation and the energy gain from the magnetostatic energy, which is known as demagnetizing energy density. The domain wall energy becomes more important compared with the demagnetization energy with decreasing grain size. Below a certain critical diameter (D_c), the ferromagnetic NPs become a single magnetic domain and behave as a permanent magnet.[85]

In some materials, it is easier to be magnetized in one direction than the others.[86] This preferred direction of spontaneous magnetization is known as easy axes determined by internal energy known as magnetic anisotropy. In the material, one can observe two different directions known as easy axes with the lowest energy cost and hard axes with the maximum energy cost.

The magnetization in a single magnetic domain nanoparticle is preferably oriented along an easy axis, and an energy barrier has to be overcome for the magnetization reversal. If the nanoparticles are separated enough to prevent any interparticle interactions, the directions of the superspins in the absence of a magnetic field are only a result of the competition between thermal fluctuation and anisotropy. For very small particles, where the energy barrier decreases below the thermal energy, the nanoparticle superspin can thermally fluctuate with time in analogy to the spins in a paramagnetic even below its critical temperature. The fluctuation stops when the

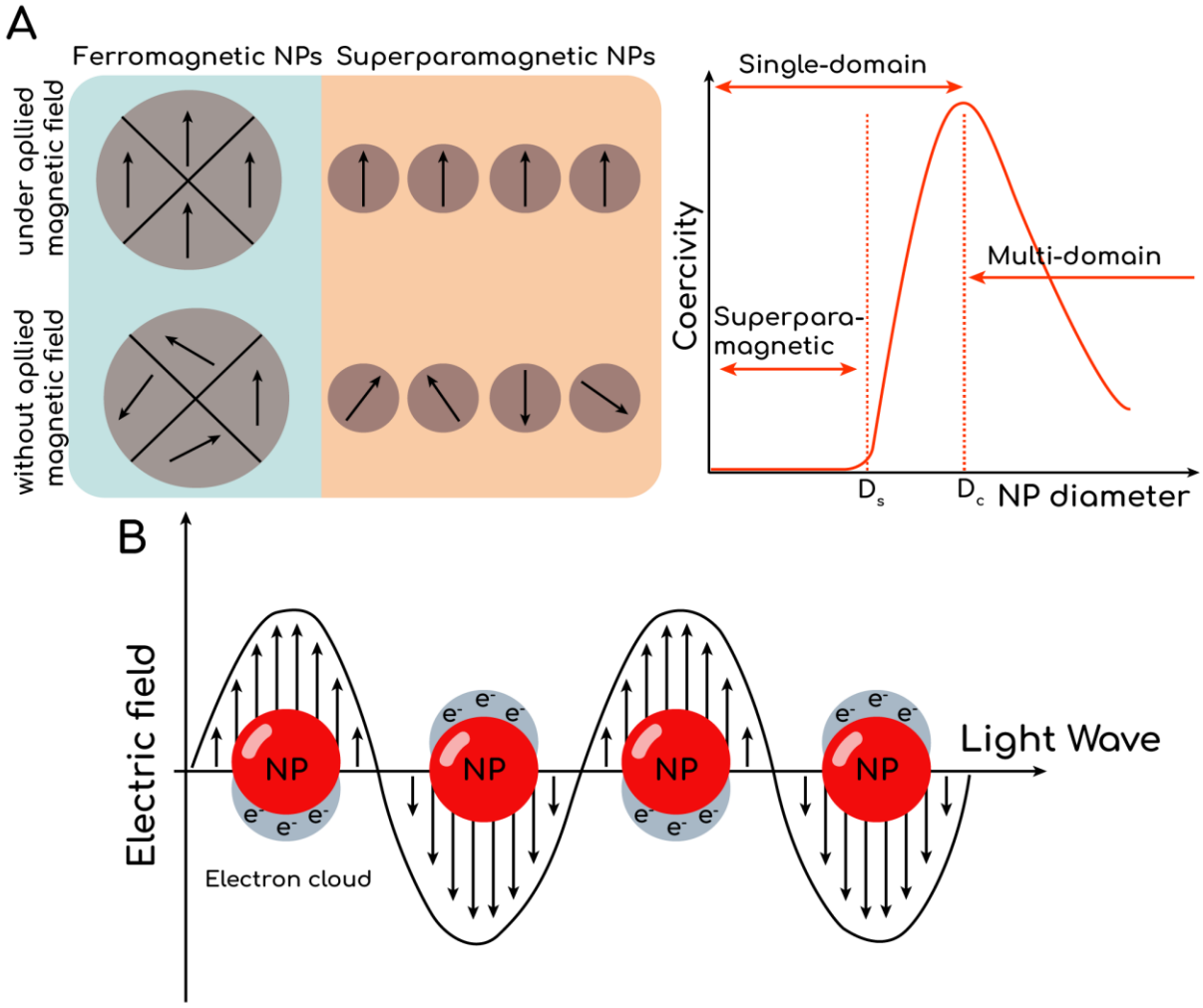

Figure 4 Nanoparticle's (NP) collective properties. (A) *Magnetic collective response. Under an external magnetic field, domains of a ferromagnetic NP align with the applied field. The magnetic moment of single domain superparamagnetic NPs aligns with the applied field. In the absence of an external field, ferromagnetic NPs will maintain a net magnetization, whereas superparamagnetic NPs will exhibit no net magnetization due to rapid reversal of the magnetic moment (left). Relationship between NP size and the magnetic domain structures. D_s and D_c are the "superparamagnetism" and 'critical' size thresholds (right).* ***(B)*** *Illustration of plasmonic coupling of metallic NPs caused by oscillating electromagnetic field.*

critical temperature known as blocking temperature (BT) reached.[87] BT is not an intrinsic value as Curie temperature and can be influenced by other sources. In particular, by the interparticle interactions, when the distances between SPM particles decrease, they start to influence the orientation of the spins of each other, creating an additional energy barrier for the spin flipping. Meaning that only by the spatial arrangement of NPs in the material, the magnetic properties can be changed without the need of changing the chemistry nor the crystal structure of NPs.[54]

Additionally, collective properties can be manifested in plasmon coupling(Fig. 4 B). This occurs when two or more plasmonic particles approach each other to a distance below roughly one diameter's length.[88] When plasmon coupling happens, the resonance of individual particles begins to hybridize, resulting in a shift in their resonance spectrum peak wavelength, either to a shorter (blueshift) or longer (redshift) wavelength. This shift depends on how the surface charge density is distributed over the coupled particles.[89] At a single particle's resonance wavelength, the surface charge densities of nearby particles can either be out of phase or in phase, which causes repulsion or attraction, leading to an increase or decrease in hybridized mode energy. The magnitude of the shift, which is a measure of plasmon coupling, depends on factors such as the interparticle gap, particle geometry, and the plasmonic resonances supported by individual particles.[90] Typically, a larger redshift is associated with a smaller interparticle gap and a larger cluster size.[91]

Collective interactions require the control of interparticle distance. This control can emerge from a delicate balance of attractive and repulsive interactions which are usually governed by VdW forces dictated by NP-ligand and ligand-solvent interaction.[92, 93] As was mentioned above, VdW forces are relatively weak, and to maximize the interaction energy, long chain-ligands are used. Long molecules as ligands create a “safety shell” around the NPs and separate them at a distance where the attraction between NPs is negligible.[94] However, creating a big interparticle spacing prevents short-range electromagnetic communication between neighboring particles. In this way, the trade-off between keeping particles safe from coalescence and achieving new and stronger collective properties.[95]

Loading nematic phase of single layer Na-hectorite was introduced to get materials with high loading and short distances between the NPs. In this way, nanoparticles of Pd or γ-Fe_2O_3 were intercalated between silicate nanosheets in a quazi-ion exchange manner. The loading of Pd NPs reached 72 wt%[96, 97], and for γ-Fe_2O_3 – 45 wt%[98] without any particles collapsing or growing. Unfortunately, such materials lack dynamic properties, characteristical for the LC. That’s why sandwiching of NPs into DS is an alternative approach to control the collective properties by controlling distances between NPs while the DS keeps the dynamics of LC.

LOCOMOTIONS IN HYDROGELS

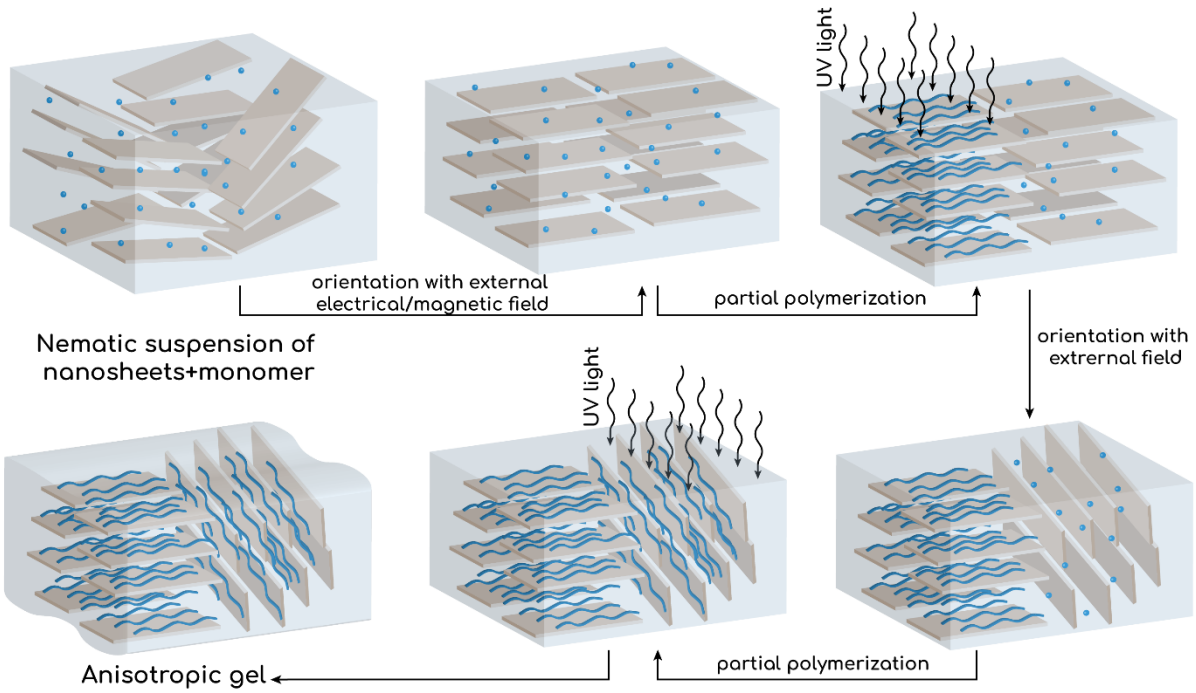

Figure 5 Schematic illustration of anisotropic hydrogels fabrication, based on Na-hectorite.

The complex morphing of natural systems serves as an inspiration for designing material for soft robotics and biomedical devices.[99] Living organisms possess remarkable abilities to adapt their shapes or positions in response to external stimuli.[100] For instance, pinecones, and Bauhinia seedpods can undergo bending and twisting deformations due to internal stresses caused by humidity changes.[101] By following and mimicking nature, we can create morphing materials and actuators that respond to specific stimuli, resulting in pre-programmed deformations and motions.

Hydrogels, in particular, gained significant interest due to their similarity to soft biotissues, ability to respond to various stimuli, ease of fabrication, and potential applications in the biomedical and engineering fields. However, compared to their biological counterparts, these morphing and actuating hydrogels have limited versatility. The controllable deformations of morphing materials are crucial for the functions of soft actuators and robots. The most crucial area of study is the exploration of new deformation modes and the underlying mechanisms. In the case of hydrogels, the asymmetric response to external stimuli plays a key role in the creation of controllable and predictable deformations. This can asymmetric response can be achieved through two main strategies. The first involves creating a gradient structure,

while the second involves applying heterogeneous stimuli. Fabricating the building blocks for the hydrogel matrix gives the possibility of combining both strategies.

To achieve programmed morphing in hydrogels, the homogeneous response of the material must be broken to avoid isotropic volume change. The best way to do that – creating a heterogeneous structure with a through-thickness gradient and an in-plane gradient in cross-linking density, component distribution, or filler orientation.[102-104]

In filler orientation, strategy fillers are oriented throughout the hydrogel, mimicking a common feature of living organisms. Site-specific orientations of fillers, such as nanosheets or cellulose fibrils, can be controlled by magnetic or electric fields or shear forces before the gelation process.[105] Synthetic hectorite offers a wide range of complex orientations, but unfortunately in the pristine form it has response only to an applied electrical field,[106-108] and adding the magnetic functionality would be of great benefit (Fig. 5).

Control of gradient structures allows for programmable deformations of hydrogels, as the separate regions respond differently to stimuli. However, hydrogels with uniform structures can also exhibit controllable deformations if stimulations are applied to spatially selected regions rather than globally.[109, 110] This deformation is driven by the swelling mismatch between actuated and un-actuated regions, similar to that seen in gradient structures. One advantage of heterogeneous stimulation is that it enables easy modulation, allowing for diverse configurations in a single hydrogel. Pristine hectorite hydrogels require addition of the photo-active particles like gold nanoparticles to enable heterogeneous-stimulation-induced deformations and in the paper “Magneto-Orientation of Magnetic Double Stacks for Patterned Anisotropic Hydrogels with Multiple Responses and Modulable Motions” we used nanosheets, contain such particles.[55]

SYNOPSIS

The present work contains two publications and one manuscript. For further publications I contributed to, please see the list of publications.

All the work is based on the expanding functionalizing of the hectorite liquid crystals and their practical application in different forms, from hydrogels to coatings. We have introduced the magnetic and the light-conversion properties to the hectorite liquid crystal. We utilized anisotropy of 2D nanosheets and translate it to OD isotropic nanoparticles. The whole liquid crystalline system acquires the functional properties of nanoparticles and preserves anisotropy from hectorite nanosheets (Fig. 6).

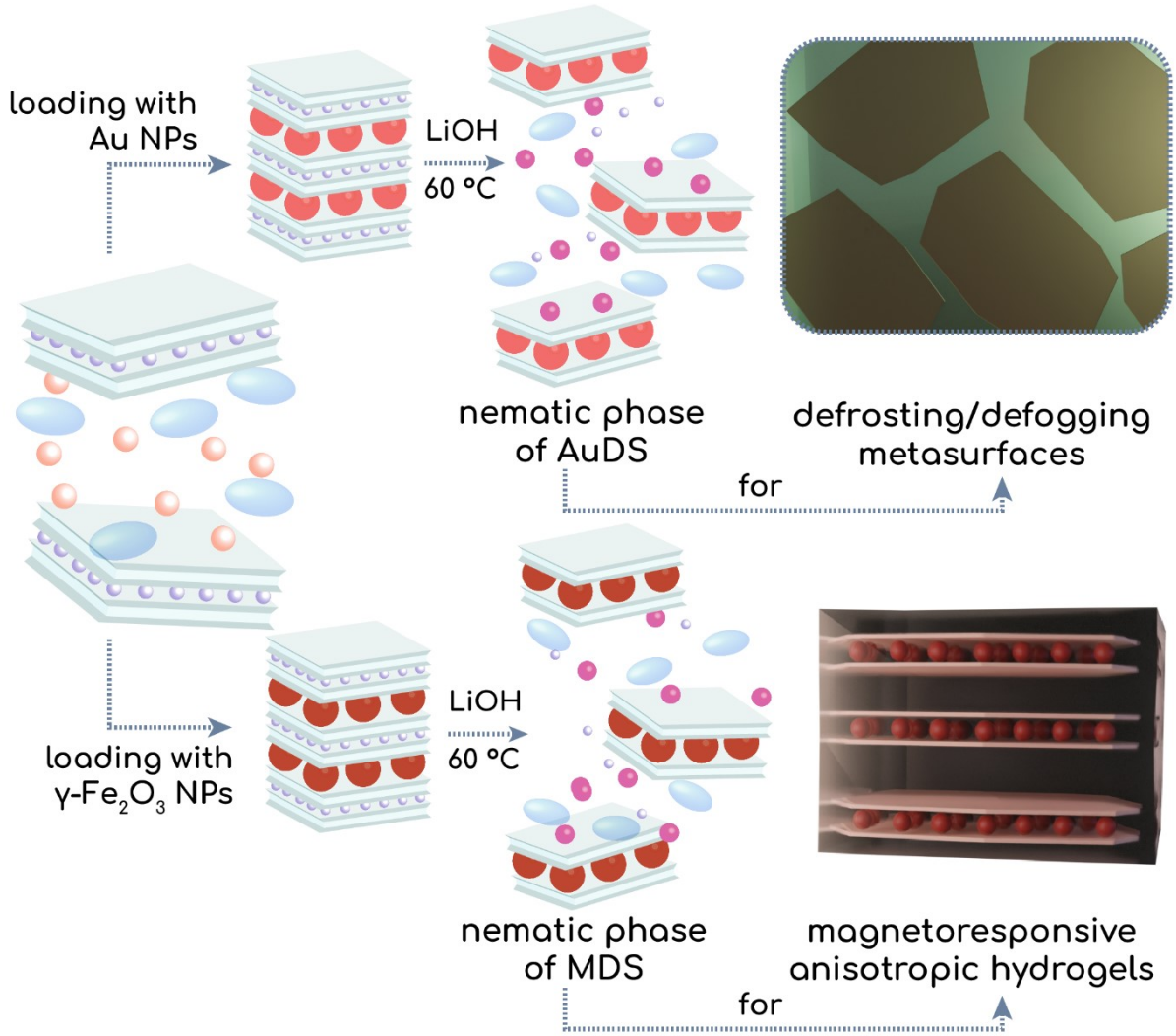

Figure 6 Graphical synopsis of the thesis showing the concept of functionalizing hectorite inorganic liquid crystals and their application.

The paper **"Colloidally stable, magnetoresponsive liquid crystals based on clay nanosheets"** describes the fabrication of anisotropic magnetic liquid crystals by combining hectorite nanosheets with maghemite nanoparticles. The Na-hectorite is a unique material due to its charge homogeneity and aspect ratio, allowing the creation of OI, which being immersed in water forms the LC phase of DS. Maghemite nanoparticles were intercalated between the hectorite nanosheets, creating sandwiched magnetic nanosheets (MDS). The MDS exhibit LC behavior and can be oriented perpendicular or parallel to an incoming magnetic field. The properties of the MDS depend on the NPs loading and their response to magnetic fields is direction-dependent. The resulting ferronematic suspension is stable in water and exhibits a highly anisotropic magnetic response that can be tuned by adjusting the starting ratio of components. Overall, this method provides a simple way to create anisotropic nanosheet-shaped colloids with adjustable interparticle interaction and magnetic properties.

The publication **"Magneto-Orientation of Magnetic Double Stacks for Patterned Anisotropic Hydrogels with Multiple Responses and Modulable Motions"** highlights the application of the MDS in the hydrogel, where they offer anisotropic mechanical properties and fast magnetic responsiveness. We developed anisotropic hydrogels using concepts inspired by biological tissues. We achieved this by aligning polymer chains or inorganic fillers into ordered structures within soft matrices using magnetic fields. The alignment of the MDS in the hydrogel was achieved using a static and rotating magnetic field. Hydrogels with highly ordered MDSs possess unique anisotropic optical and mechanical properties and exhibit anisotropic responses to changes in temperature. The hydrogels are useful in designing functional materials and soft actuators with versatile applications, and they exhibit multi-gait motions steered by light and magnetic fields. The combination of various stimulus-response properties of the hydrogels has the potential to enhance the design and management of soft actuators and robots for specific applications.

The article **"Fabricating defogging metasurfaces via a water-based colloidal route"** focuses on the development of a wet colloid chemistry-based method to fabricate thin, transparent coatings with anisotropic heat conductivity. The coatings are made using a liquid crystalline, electrostatically stabilized suspension of DS with intercalated spherical gold NPs between two dielectric 1 nm thick silicate nanosheets

(AuDS). The AuDS were assembled on a planar substrate, adopting the defined orientation, to yield anisotropic heat conductivity without the need for preparing a patterned surface. The absorbance of the metasurface is tunable by modulating plasmonic coupling via a variation of nanoparticle loading. These coatings allow for fast defogging and defrosting under solar irradiation.

COLLOIDALLY STABLE, MAGNETORESPONSIVE LIQUID CRYSTALS BASED ON CLAY NANOSHEETS

Materials with multiple stimuli-responsive pathways and which show direction-dependent properties can enable more elaborate functionalities in future technologies. LCs are intrinsically responsive to electrical fields but show only a weak response to magnetic fields. However, the combination of magnetic NPs with a nematic phase,

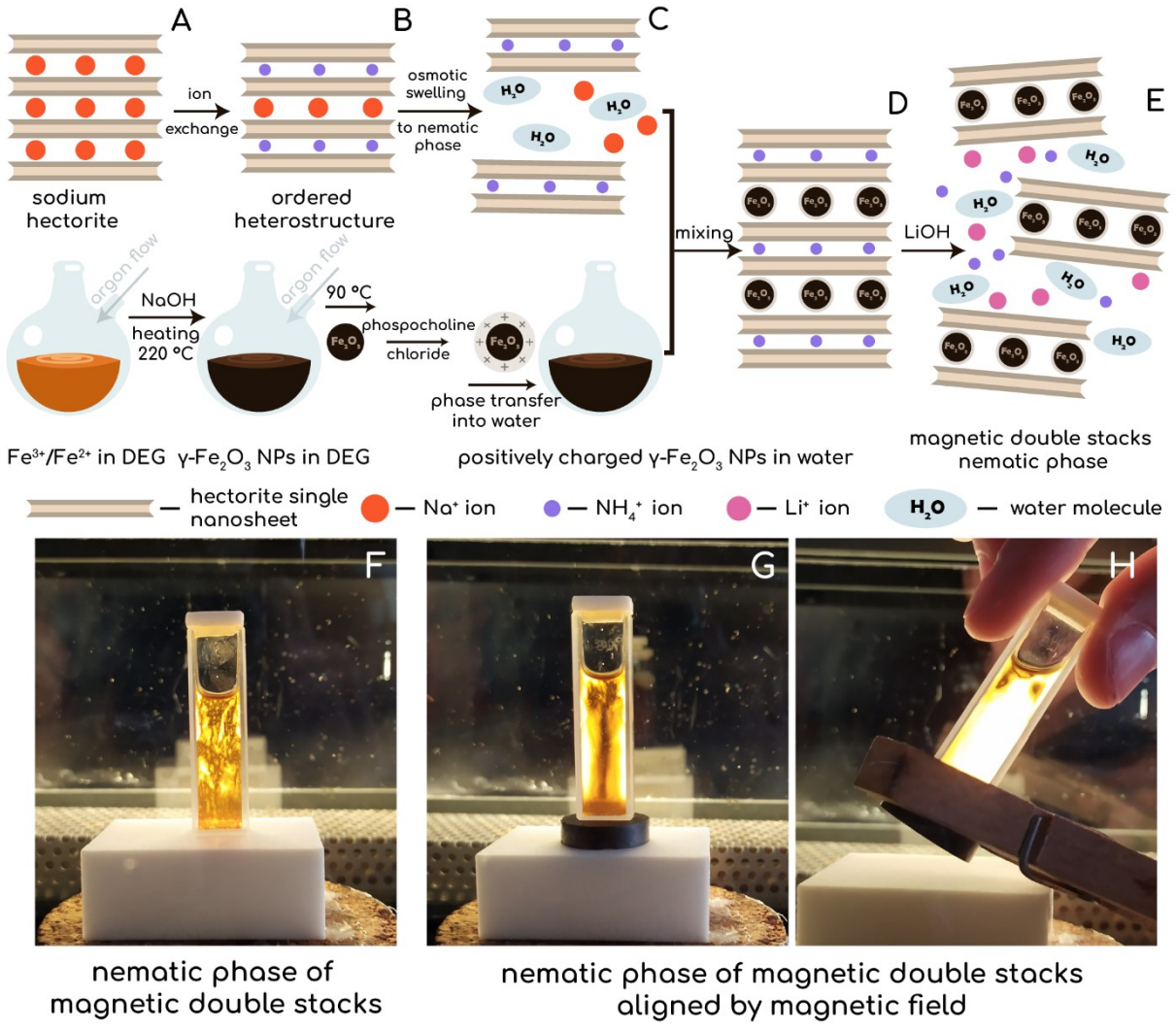

Figure 7 Schematic illustration of the MDS preparation procedure. ***(A)*** *Sodium hectorite structure.* ***(B)*** *Ordered heterostructures.* ***(C)*** *Osmotic swelling of ordered heterostructures yields a nematic phase of* NH_4^+ *-DS.* ***(D)*** *Heterostructures with strict alternation* NH_4^+ *and γ-*Fe_2O_3 *interlayers.* ***(E)*** *MDS nematic phase.* ***(F)*** *Photo of nematic LC phase of MDS with a concentration of 0.2 wt% under cross polarised light.* ***(G)*** *and* ***(H)*** *images of MDS aligned by a magnetic field with different orientations. Reprinted with permission 2021. Copyright Royal Society of Chemistry.*

could dramatically increase the effective director-magnetic field interaction and lead to unique physical properties.

The paper focuses on the fabrication of ordered heterostructures of Na-hectorite loaded with maghemite NPs and their 1D dissolution in an aqueous dispersion to a nematic phase comprised of MDS. This approach combines the best aspects of both known strategies to fabricate colloidally stable, anisotropic magnetoresponsive liquid crystals.

Magnetic liquid crystals were prepared from synthetic Na-hectorite, which is unique material due to high charge homogeneity and huge nanosheet aspect ratio. Those features allow us to produce ordered interstratifications where every other layer of interlayer Na^+ is exchanged for NH_4^+. Upon immersing into water such structure is 1D dissolved along Na^+ layers, but NH_4^+ layer stays intact, gluing two silicate nanosheets together. In this way, former Na^+ layers are activated for NPs intercalation and NH_4^+ layers are protected from any quasi-ion exchange (Fig. 7 A to C).

γ-Fe_2O_3 NPs were prepared via polyol method. For intercalation, NP's surface charge has to be positive for utilization of the negative hectorite nanosheets surface charge. For preparation of MDS, NH_4^+/Na^+-DS were immersed into water in order to create 1 wt% dispersion and was quickly injected into γ-Fe_2O_3 NPs dispersion. In this step, we partially exchanged Na^+ for NPs while NH_4^+ layers stayed intact. We used different volume of 0.1 wt% γ-Fe_2O_3 NPs dispersion to achieve different loading – 16.6, 30, and 45 wt% (MDS 16.6, MDS 30, and MDS 45, respectively). As a next step, NH_4^+ layers were activated for 1D dissolution by exchanging NH_4^+ for Li^+. In the end, we obtain magnetic γ-Fe_2O_3 NPs, sandwiched between two silicate layers while each "sandwich" is separated from another for a distance >50 nm due to electrostatic repulsion. Electrostatic repulsion between the MDS ensures the long-lasting colloidal stability of the ferronematic liquid crystal, avoiding the problem of coagulation due to magnetic dipole-dipole interaction (Fig. 7 D and E).

As prepared MDS show a quick response even to the moderate magnetic field, which highlights their difference compared to other magnetic 2D materials. MDS can be easily organized into the monodomain LC with different nematic director orientations by changing the angle of a magnetic field (Fig. 7 F to H).

We applied the AFM, PXRD, BET, and TEM measurements for further material characterization. The AFM suggests the height of the single MDS to be 8.5 nm, which

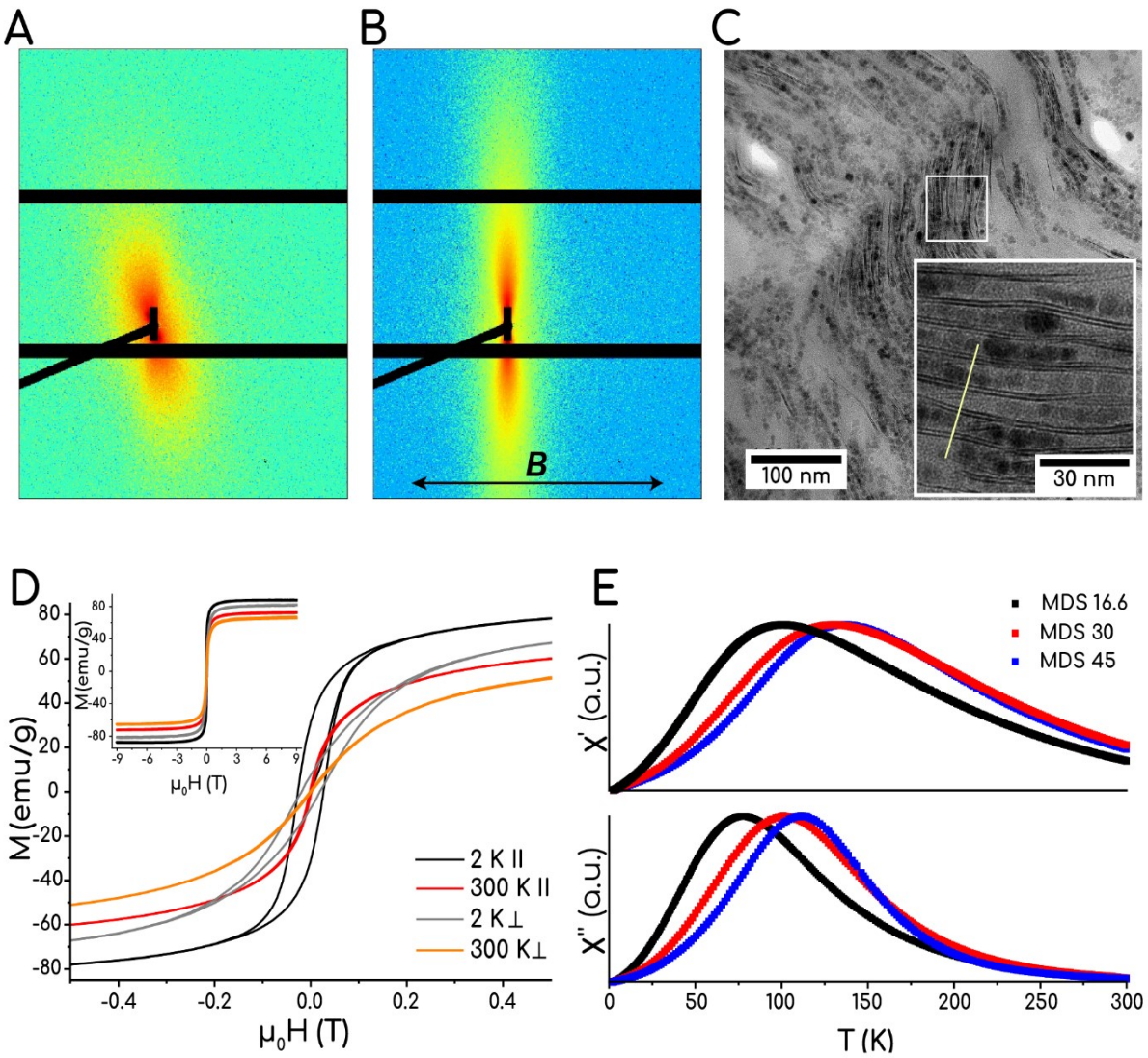

Figure 8 MDS characterization (A) *SAXS pattern of 4 wt% aqueous dispersion of MDS 16.6 recorded without magnetic field applied and with the detector set at low q-value.* ***(B)*** *2D SAXS pattern of 4 wt% aqueous dispersion of MDS 16.6 recorded with the magnetic field applied and with the detector set at low q-value. Vector B indicates the direction of applied magnetic field.* ***(C)*** *Cross-sectional TEM image of MDS. The inset shows the magnification of highly loaded nanosheets with the periodic nanoparticle-nanosheets arrangement.* ***(D)*** *M(H) curves for magnetic fields up to 0.5 T collected on the MDS 45 film at temperatures and magnetic field orientations as indicated. The inset shows the data for the full range of magnetic fields.* ***(E)*** *Real and imaginary parts (χ' and χ'') of the AC susceptibility as a function of temperature measured in zero DC field with f_{AC} as indicated for the sample with different loading and in-plane field orientation. The χ' signal measured for out-of-plane field orientation. Reprinted with permission 2021. Copyright Royal Society of Chemistry.*

is a sum of 2*1nm thickness of nanosheets + 6.5 nm sized γ-Fe_2O_3 NPs. TEM images suggest that nanoparticles are sandwiched between nanosheets while the other side

of the nanosheet is free of NPs (Fig.8 C). PXRD analysis shows no changes in the γ-Fe_2O_3 crystalline phase upon intercalation. BET measurements confirm mesoporous structure and show an increase in surface area with the increasing NPs content within the MDS.

Magnetic SAXS measurements demonstrate the change of the MDS orientation upon the application of a magnetic field with the simultaneous increase in the order parameter (Fig.8 A and B). Moreover, the different NPs content in MDS leads to different responses to the applied magnetic field.

The γ-Fe_2O_3 nanoparticle of 6.5 nm size is a single magnetic domain, but being intercalated into DS, γ-Fe_2O_3 NPs are trapped in the coupled state. This leads to MDS showing superparamagnetic behavior, opposite to single NP's ferromagnetic behavior. Increasing the content of NPs leads to increasing freezing temperature and magnetic susceptibility, further broadening the tunability of MDS (Fig.8 E). In addition, the anisotropic structure of the material leads to the difference in response to applied parallel and perpendicular magnetic field to MDS film (Fig.8 D).

In conclusion, we propose a simple method to create anisotropic nanosheet-shaped colloids with adjustable interparticle interaction and magnetic properties. The resulting ferronematic suspension is stable in water and exhibits LC behavior at low MDS concentrations. By adjusting the starting ratio of components, the interaction strength of magnetic nanoparticles can be tuned, resulting in a highly anisotropic magnetic response.

MAGNETO-ORIENTATION OF MAGNETIC DOUBLE STACKS FOR PATTERNED ANISOTROPIC HYDROGELS WITH MULTIPLE RESPONSES AND MODULABLE MOTIONS

Advancements in intelligent materials were made using concepts inspired by biological tissues. Hydrogels, which have water as their primary component and share similarities with living tissues, have been the subject of intense research interest. However, their isotropic network differs from the anisotropic structures found in biological tissues like muscles and ligaments. To expand their potential applications in biomedical and engineering domains, researchers have created anisotropic hydrogels by organizing polymer chains or inorganic fillers into ordered structures within soft matrices. Various methods have been used, including stretching the material to orient polymer chains, aligning rigid molecules or anisotropic fillers under external fields, and orienting mesogens and inorganic fillers using magnetic fields.

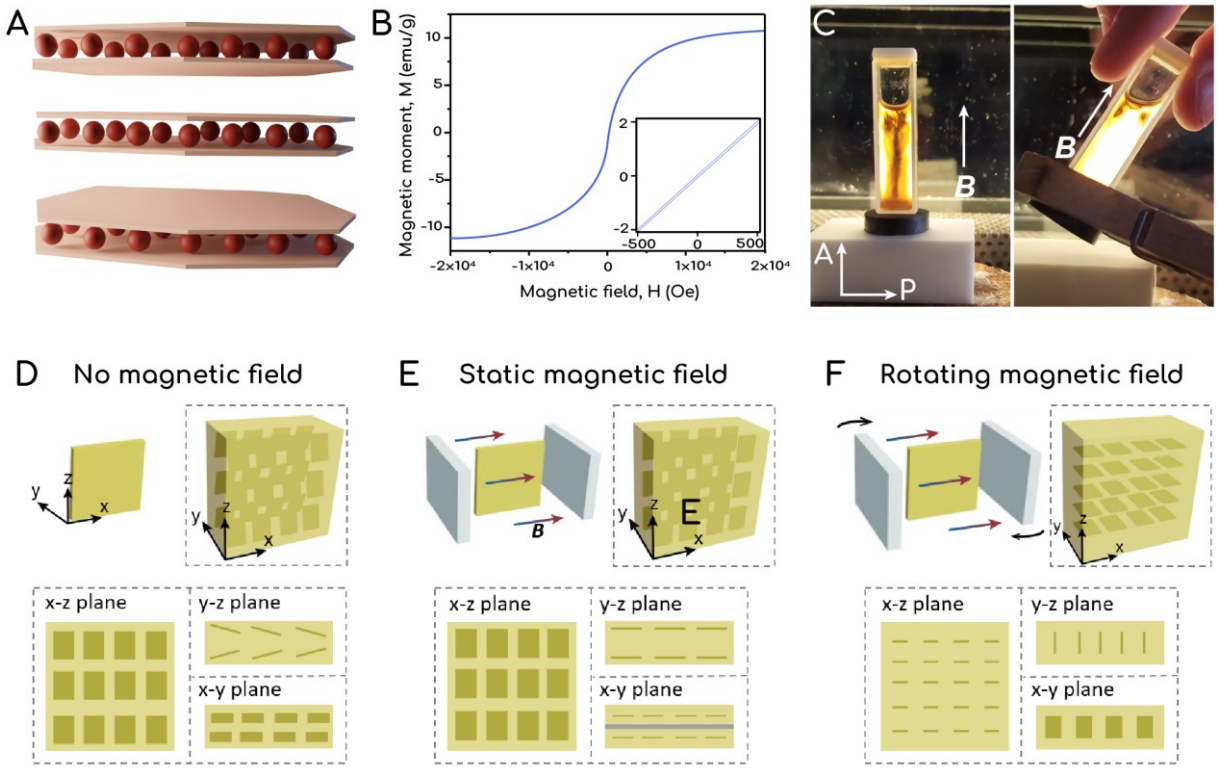

Figure 9 . MDS anisotropic hydrogel characterization (A) *Schematic illustration of the MDSs structure.* ***(B)*** *Magnetic hysteresis loop of MDS powder.* ***(C)*** *Photos of a ferronematic suspension of MDS (1 wt%) between a pair of crossed polarized films. A magnet is placed under the cuvette filled with the MDS suspension.* ***(D-F)*** *Schematic for the gel synthesis and the alignments of MDSs The hydrogels were prepared without magnetic field* ***(D)****, with static magnetic field* ***(E)****, or with rotating magnetic field* ***(F).*** *Reprinted with permission 2022. Copyright Wiley-VCH.*

Magnetic fields can be used to orient mesogens and inorganic fillers in a non-contact mode and develop anisotropic materials (Fig. 9 A). We have fabricated a series of anisotropic PNIPAm hydrogels using a weak rotating magnetic field to orient 2D MDS, which exhibited anisotropic optical and mechanical properties due to the highly ordered arrangement of the MDSs. These patterned hydrogels showed complex birefringent patterns and were deformed into three-dimensional configurations, enabling versatile locomotion through dynamic actuation under spatiotemporal light and magnetic fields (Fig. 9 B and C). This strategy can be useful in designing functional materials and soft actuators with versatile applications.

Alignment of the MDS within the hydrogel was achieved using static and rotating magnetic fields (Fig. 9 D to F). Without orientation, hydrogels have a polydomain nematic liquid crystalline structure with the low order parameter measured by SAXS. Static magnetic field allows to get higher orientation order compare to the non-oriented sample, but does not change the preferential alignment of the polydomain liquid crystalline hydrogel, but rather merges it into the monodomain structure. Opposite to the static magnetic field, the rotating magnetic field allows the making of hydrogels with the nematic director perpendicular to the preferential orientation, caused by the geometry of the hydrogel mold.

The MDS hydrogel’s degree of orientation highlights the high structuring effect of the rotating magnetic field that is preserved upon swelling of the hydrogel. The orientation degree in x-z plane slightly decreases from 0.88 to 0.86 and in the y-z direction from 0.86 to 0.83. The MDS leads to the anisotropic mechanical properties of the hydrogel, where Young's modulus in the parallel direction to the MDS alignment is 25 kPa, while the in the perpendicular – is only 8 kPa. The range of these values encompasses the modulus of the isotropic gel with Young’s modulus of 15 kPa, which is in agreement with classical theories of filler-reinforced materials.

The alignment of the MDS can be used to create the internal microstructure by ways of photolithographic polymerization, whereupon alignment of the MDS only part of the hydrogel is exposed to the UV light, causing the hydrogel polymerization. This allows encoding the complex pictures, visible only under the cross-polarised light with the parts, visible only under a certain rotation angle.

Fe_2O_3 nanoparticles have a wide absorption band and are capable of absorbing laser energy and converting it to heat. In combination with the PNIPAm, the LCST polymer

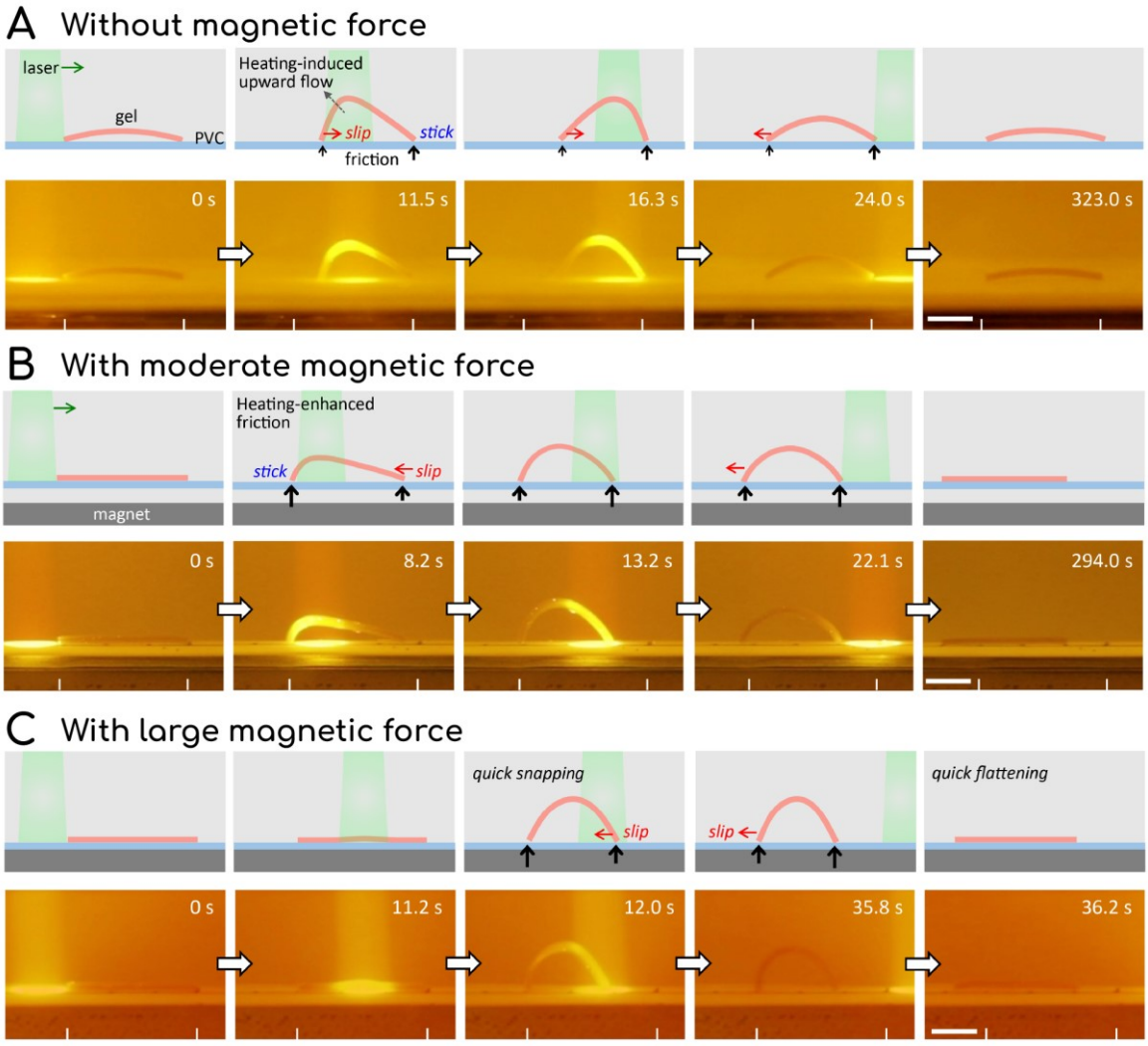

Figure 10 Snapshots showing the walking gait of the stripe-patterned anisotropic hydrogel. ***(A)*** *Without magnetic force.* ***(B)*** *With moderate magnetic force* ***(C)*** *With large magnetic force. Reprinted with permission 2022. Copyright Wiley-VCH.*

with the transition temperature of 32 °C, leads to the on-demand local deformations, caused by heating. For example, heating of the MDS hydrogel with the laser intensity of 2.8 W/cm^2 causes the local temperature to increase above the LCST point only in 2 seconds, making it the perfect material for the light-driven actuation.

Combining above mention properties, the sophisticated walking pattern was demonstrated under the exposure of the moving laser beam and the impact of magnetic fields with different magnetic strengths. If the sample is exposed to no magnetic field, the movement is slow (Fig. 10 A), due to the small deformations and low-density mismatch between hydrogel (1.02 g/cm^3) and water (0.997 g/cm^3), whereupon the weak magnetic field, the movement becomes faster, but still too slow to practical application (Fig. 10 B). Upon applying a strong magnetic field, the

movement and deformations are more abrupt (Fig. 10 C). The unique distortions and movements of the hydrogel that are manipulated by both magnetic fields and photo actuation are directly linked to the anisotropic structure and the multi-response capabilities of the MDSs. This combination of various stimulus-response properties of the hydrogels has the potential to enhance the design and management of soft actuators and robots for particular applications. It is important to note that the multi-gait movements demonstrated in this study differ from previously reported examples in terms of kinematics. Prior studies typically employ two strategies to convert cyclic bending/unbending or stretching/contraction deformations into directional walking motions, including the use of a ratchet plate or creating an asymmetric gel shape to generate asymmetric friction against the substrate.

To sum up, our study involved the creation of a variety of anisotropic hydrogels using a rotating magnetic field to align MDSs, followed by polymerization to solidify the ordered structures. These PNIPAm nanocomposite hydrogels, with their highly ordered MDSs, possess unique anisotropic optical and mechanical properties and exhibit anisotropic responses to changes in temperature or light. These properties are attributed to the distinct features of MDSs, such as their sandwich-like structure, high aspect ratio, high charge density, and sensitivity to magnetic and light fields. We also developed hydrogels with complex anisotropic MDS structures using multi-step magnetic orientation and photolithographic polymerization, resulting in gels with a variety of birefringent patterns and pre-programmed deformations upon heating or light irradiation. Furthermore, these patterned hydrogels can be manipulated to achieve distinct motions under spatiotemporal light irradiation with the aid of a static magnet, which controls the friction force between the gel and substrate. The fabrication of anisotropic hydrogels using magneto-orientation, as well as the cooperative manipulation strategy for controllable motions, provide valuable insights for the design of high-performance hydrogel devices. These hydrogels, with their controllable anisotropic structures, multiple stimuli-responsiveness, programmable deformations, and motions, have broad applications in biomedical and engineering fields, including biomedical devices, soft actuators/robots, and more.

FABRICATING DEFOGGING METASURFACES VIA A WATER-BASED COLLOIDAL ROUTE

The article discusses the development of "metamaterials 4.0" which incorporates chemical concepts into their design to achieve functions beyond what can be achieved through traditional nanofabrication and engineering methods. Metamaterials are structures created by intentionally applying nanoscopic building blocks at the mesoscale to achieve extraordinary properties not found in nature.

Similar to the magnetic functionalities, by changing the type of NPs, we can introduce other functional properties to LC. The alternation of dielectric and conductive layers

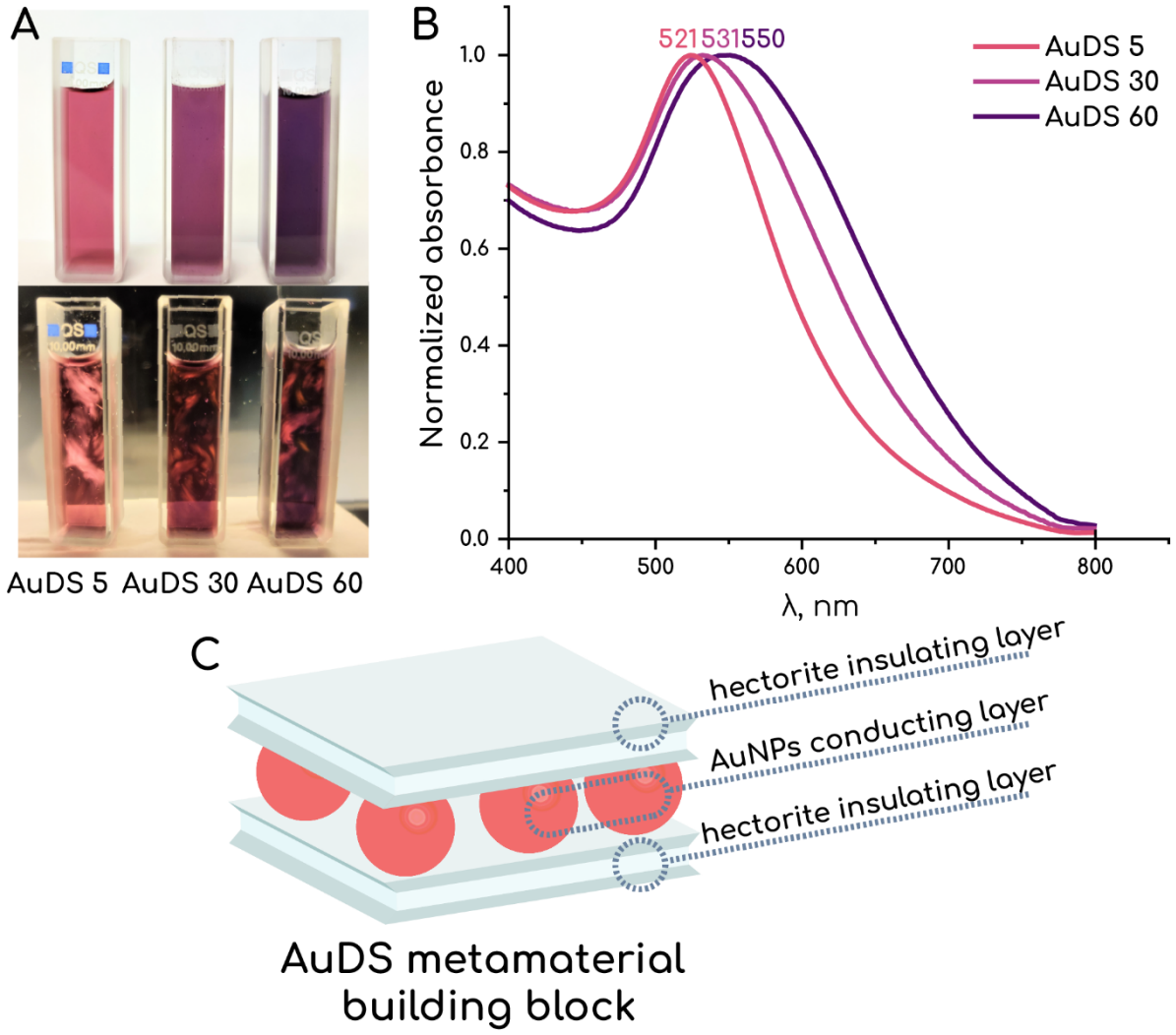

Figure 11 Characterization of AuDS ***(A)*** *Aqueous liquid crystalline AuDS suspensions in daylight (top) and cross-polarised light (bottom) showing the birefringent nature.* ***(B)*** *UV-vis spectra of AuDS with different Au loadings showing a gradual red shift.* ***(C)*** *Schematic representation of the metamaterial building block consisting of insulating hectorite monolayers sandwiching a light-absorbing layer of Au NPs.*

leads to the formation of new intricate properties (Fig. 11 C). As soon as hectorite nanosheets can be regarded as a dielectric layer, we have chosen the Au NPs to be intercalated and form conductive layers to fabricate a metamaterial building block-AuDS.

Unlike the maghemite NPs, the synthesis of Au NPs is trickier and requires additional synthetic steps to produce suitable for intercalation, positively charged NPs. We start with the synthesis of citrate capped, negatively charged Au NPs with a narrow size distribution and mean diameter of 6.5 nm. Direct charge reverse is not possible in the single phase for NPs dispersion of high concentration. For this reason, we utilize two steps phase transfer. In the first step, we use TOAB as a phase-transfer agent for transferring citrate capped Au NPs into toluene phase. In the second step, the NPs are transferred back into water with DMAP assistance, yielding positive charged NPs without altering size distribution. After that DMAP capped Au NPs are ready to be intercalated into DS in a similar procedure to the fabrication of MDS. We have prepared the samples with 5, 30, and 60 wt% of Au NPs, named as AuDS 5, AuDS 30, and AuDS 60, respectively.

As for MDS, variation of the NP's content in AuDS leads to the different collective NPs properties. In this case, we observe a change of the LSPR peak position for AuDS dispersions. LSPR peak redshifts and gets broader with increasing NPs content. The LSPR peak was further deconvolved into two components, corresponding to the contribution from isolated and coupled Au NPs (Fig. 11 A and B). We have correlated the LSPR peak position with the closest-neighbor distance within the AuDS, using a plasmonic ruler. The calculation of the gap distance was verified by the TEM observation of the top view of a single AuDS.

AuDS was further characterized with SAXS, TEM, and AFM. SAXS suggests the LC behavior of AuDS with the two scattering objects (spherical and 2D disk-shaped) contributing to the SAXS pattern. AFM shows the height of the single AuDS of 9 nm, which is in good agreement with the sum of Au NP diameters (7 nm) and the thickness of 2 silicate monolayers (2 x 1 nm). Surprisingly, if AuDS are prepared as multilayer films, TEM images revealed that the spherical nanoparticles were strongly deformed to an elliptical shape upon drying, which also changed the color of the sample from red to blue. The deformation was hypothesized to be triggered by the electrostatic attraction between negatively charged hectorite layers and positively charged Au NPs.

To show the realistic, spherical shape of Au NPs in AuDS, we have prepared hydrogels, where the drying effect is suppressed.

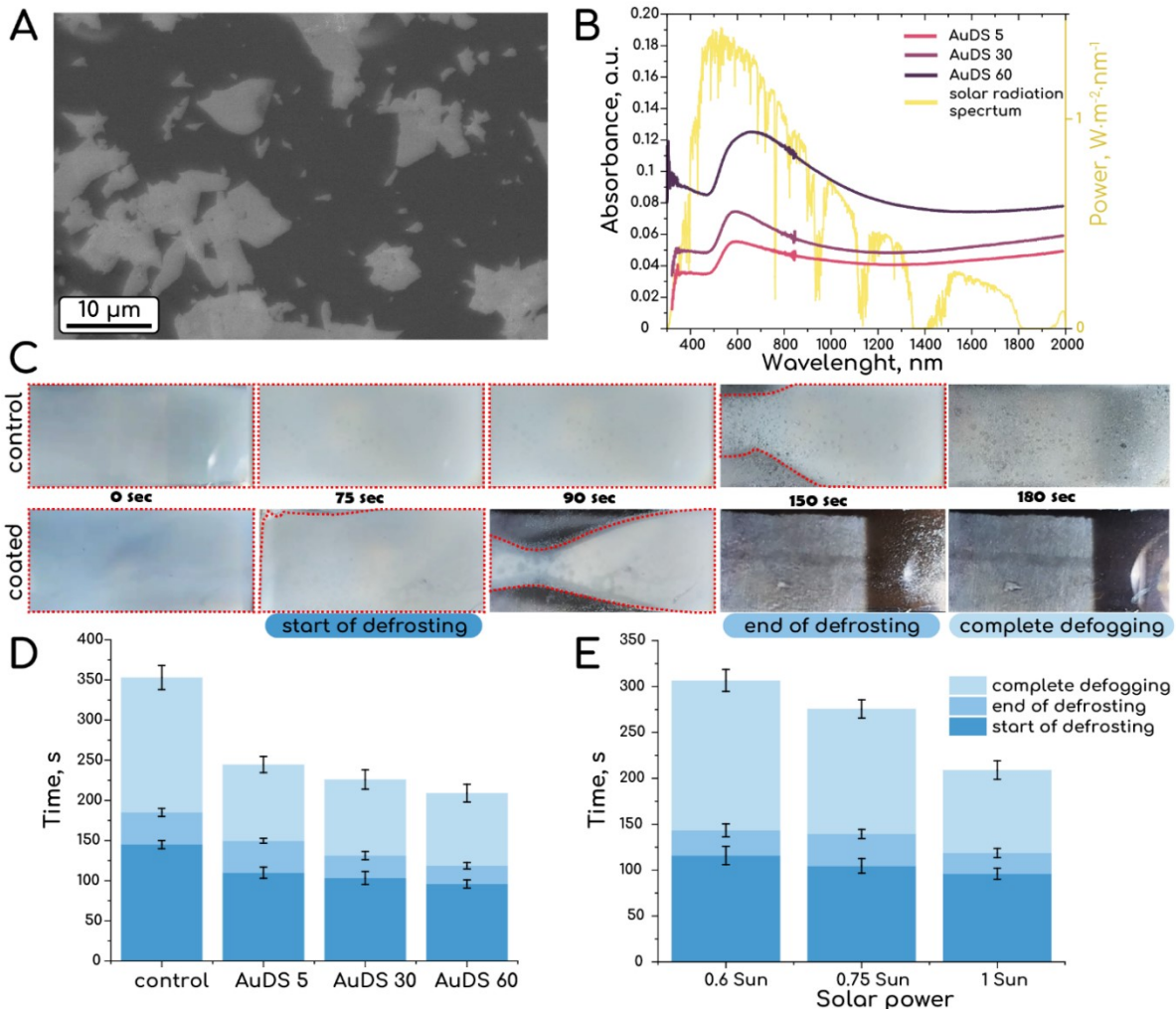

Figure 12 Defrosting and defogging performance of AuDS coated glass slides. (A) *SEM image of the AuDS coated surface. SEM imaging suggests incomplete mostly monolayer coverage.* ***(B)*** *Absorbance spectra of AuDS coated metasurfaces. The solar spectrum is included for reference in yellow (ASTM G173-03 Reference Spectra).* ***(C)*** *Sequence of images following the defrosting and defogging of an uncoated and a AuDS 60 coated glass slide over time under 1 sun solar irradiation.* ***(D)*** *Time dependency histogram of defrosting and defogging for different AuDS coatings measured under 1 sun irradiation.* ***(E)*** *Time dependency histogram of defrosting and defogging for a AuDS 60 coated glass slide measured under different irradiation power.*

AuDS were further used as a building block to fabricate the metasurface with defrosting and defogging properties under solar irradiation. Au NPs layer absorbs in the IR and NIR range of the solar spectrum converting it to heat and hectorite nanolayers act as heat conductors and distributors (Fig. 12 A to C).

AuDS metasurface was prepared on the glass substrate via dip coating method in order to create mostly monolayer coverage. Due to the high aspect ratio of hectorite nanosheets, AuDS have the preferred orientation on the substrate and do not require additional manipulation to build the self-assembly as a film. The resulting coating shows high transparency in the visible range and effectively reduces the defrosting and defogging time by 60% compared to uncoated glass Metasurface can also be prepared via facile methods such as spray coating without sacrificing defogging performance (Fig. 12 D and E).

To sum up, sandwiching Au NPs between nanosheets can create functional double stacks with energy conversion properties that can be varied by adjusting the NPs loading and average separation of NPs. This can lead to plasmonic coupling and a redshift of the absorbance spectra, which can be used for applications such as defrosting and defogging metasurfaces. The resulting DS are easy to orient on planar substrates and offer economic and technical advantages over traditional physical and chemical vapor deposition methods.

INDIVIDUAL CONTRIBUTION

Colloidally stable, magnetoresponsive liquid crystals based on clay nanosheets

J. B., S. F., S. M., W. B., I, and D. W. conceived the project and designed the experiments. I and D. W. performed the synthesis and sample characterization. S. M. performed the magnetic measurements. S. R. and M. D. performed SAXS measurements, V. D. and S. R. assisted with the SAXS part of the manuscript. K. O. and G. P. performed AFM measurements. All authors read and contributed to the manuscript preparations.

Magneto-Orientation of Magnetic Double Stacks for Patterned Anisotropic Hydrogels with Multiple Responses and Modulable Motions

I have performed the synthesis and characterization of the MDS and participated in the data analysis, discussion, and interpretation of the results and paper writing. C.F.D. and C.Z performed the experiments with hydrogels. P.Z. and M.D. and Q.L.Z., carried out theoretical and numerical analyses. Q.L.Z., D.J., J.B., Z.Q., and Z.L.W. contributed to the discussion and interpretation of the results.

Fabricating defogging metasurfaces via a water-based colloidal route

J. B and I conceived the project and designed the experiments. I performed the synthesis and sample characterization. V. D. and S. R. assisted with the SAXS part of the manuscript. All authors read and contributed to the manuscript preparations.

REFERENCES

1. A. Gupta, T. Sakthivel and S. Seal, Prog. Mater. Sci., 2015, 73, 44–126.
2. Z. Zhen and H. Zhu, in Graphene, Academic Press, Cambridge, MA, USA, 2018, DOI: 10.1016/b978-0-12-812651-6.00001-x, pp. 1–12.
3. K. S. Novoselov, A. K. Geim, S. V. Morozov, D. Jiang, Y. Zhang, S. V. Dubonos, I. V. Grigorieva and A. A. Firsov, Science, 2004, 306, 666–669.
4. A. K. Geim and K. S. Novoselov, Nat. Mater., 2007, 6, 183–191.
5. D. Akinwande, C. J. Brennan, J. S. Bunch, P. Egberts, J. R. Felts, H. Gao, R. Huang, J.-S. Kim, T. Li, Y. Li, K. M. Liechti, N. Lu, H. S. Park, E. J. Reed, P. Wang, B. I. Yakobson, T. Zhang, Y.-W. Zhang, Y. Zhou and Y. Zhu, Extreme Mech. Lett., 2017, 13, 42–77.
6. C. Wang, G. Zhang, S. Huang, Y. Xie and H. Yan, Adv. Opt. Mater., 2020, 8, 1900996.
7. C. Huo, Z. Yan, X. Song and H. Zeng, Science Bulletin, 2015, 60, 1994–2008.
8. V. Dudko, O. Khoruzhenko, S. Weiß, M. Daab, P. Loch, W. Schwieger and J. Breu, Adv. Mater. Technol., 2023, 8, 2200553.
9. T. Sasaki and M. Watanabe, J. Phys. Chem. B, 1997, 101, 10159–10161.
10. L. Wang and T. Sasaki, Chem. Rev., 2014, 114, 9455–9486.
11. Y. Hernandez, V. Nicolosi, M. Lotya, F. M. Blighe, Z. Sun, S. De, I. T. McGovern, B. Holland, M. Byrne, Y. K. Gun'Ko, J. J. Boland, P. Niraj, G. Duesberg, S. Krishnamurthy, R. Goodhue, J. Hutchison, V. Scardaci, A. C. Ferrari and J. N. Coleman, Nat. Nanotechnol., 2008, 3, 563–568.
12. A. K. Geim and I. V. Grigorieva, Nature, 2013, 499, 419–425.
13. K. S. Novoselov, A. Mishchenko, A. Carvalho and A. H. C. Neto, Science, 2016, 353, aac9439.
14. Y. Oaki, Chem. Lett., 2020.
15. S. Yang, P. Zhang, A. S. Nia and X. Feng, Adv. Mater., 2020, 32, 1907857.
16. Y. Yang, H. Hou, G. Zou, W. Shi, H. Shuai, J. Li and X. Ji, Nanoscale, 2019, 11, 16–33.

17. M. A. Islam, P. Serles, B. Kumral, P. G. Demingos, T. Qureshi, A. Meiyazhagan, A. B. Puthirath, M. S. B. Abdullah, S. R. Faysal, P. M. Ajayan, D. Panesar, C. V. Singh and T. Filleter, Appl. Phys. Rev., 2022, 9, 041301.

18. A. Ciesielski and P. Samorì, Chem. Soc. Rev., 2014, 43, 381–398.

19. A. Jawaid, D. Nepal, K. Park, M. Jespersen, A. Qualley, P. Mirau, L. F. Drummy and R. A. Vaia, Chem. Mater., 2016, 28, 337–348.

20. Z. Li, R. J. Young, C. Backes, W. Zhao, X. Zhang, A. A. Zhukov, E. Tillotson, A. P. Conlan, F. Ding, S. J. Haigh, K. S. Novoselov and J. N. Coleman, ACS Nano, 2020, 14, 10976–10985.

21. V. Nicolosi, M. Chhowalla, M. G. Kanatzidis, M. S. Strano and J. N. Coleman, Science, 2013, 340, 1226419.

22. N. Takahashi and K. Kuroda, J. Mater. Chem., 2011, 21, 14336–14353.

23. J. McCarney and M. V. Smalley, Clay Miner., 1995, 30, 187–194.

24. R. Ma, Z. Liu, L. Li, N. Iyi and T. Sasaki, J. Mater. Chem., 2006, 16, 3809–3813.

25. T. Maluangnont, K. Matsuba, F. Geng, R. Ma, Y. Yamauchi and T. Sasaki, Chem. Mater., 2013, 25, 3137–3146.

26. D. Yamaguchi, N. Miyamoto, S. Koizumi, T. Nakato and T. Hashimoto, J. Appl. Crystallogr., 2007, 40, s101–s105.

27. Y. Song, N. Iyi, T. Hoshide, T. C. Ozawa, Y. Ebina, R. Ma, S. Yamamoto, N. Miyamoto and T. Sasaki, Dalton Trans., 2018, 47, 3022–3028.

28. S. Rosenfeldt, M. Stöter, M. Schlenk, T. Martin, R. Q. Albuquerque, S. Förster and J. Breu, Langmuir, 2016, 32, 10582–10588.

29. M. Daab, N. J. Eichstaedt, A. Edenharter, S. Rosenfeldt and J. Breu, RSC Adv., 2018, 8, 28797–28803.

30. M. Daab, N. J. Eichstaedt, C. Habel, S. Rosenfeldt, H. Kalo, H. Schießling, S. Förster and J. Breu, Langmuir, 2018, 34, 8215–8222.

31. D. R. Lewis, Clays Clay Miner., 1952, 1, 54–69.

32. T. Selvam, A. Inayat and W. Schwieger, Dalton Trans., 2014, 43, 10365–10387.

33. Elsevier, Handbook of Clay Science, Elsevier Science, Walthm, MA, USA, 2006.

34. R. R. Weil and N. C. Brady, The Nature and Properties of Soils, Pearson, London, England, UK, 2016.

35. E. L. Hansen, H. Hemmen, D. M. Fonseca, C. Coutant, K. D. Knudsen, T. S. Plivelic, D. Bonn and J. O. Fossum, Sci. Rep., 2012, 2, 1–4.

36. F. Bergaya and G. Lagaly, in Developments in Clay Science, Elsevier, Walthm, MA, USA, 2013, vol. 5, pp. 1–19.

37. E. Galán and R. E. Ferrell, in Developments in Clay Science, Elsevier, Walthm, MA, USA, 2013, vol. 5, pp. 83–126.

38. M. F. Brigatti, E. Galán and B. K. G. Theng, in Developments in Clay Science, Elsevier, Walthm, MA, USA, 2013, vol. 5, pp. 21–81.

39. J. Breu, W. Seidl, A. J. Stoll, K. G. Lange and T. U. Probst, Chem. Mater., 2001, 13, 4213–4220.

40. M. Stöter, D. A. Kunz, M. Schmidt, D. Hirsemann, H. Kalo, B. Putz, J. Senker and J. Breu, Langmuir, 2013, 29, 1280–1285.

41. M. Stöter, S. Rosenfeldt and J. Breu, Annu. Rev. Mater. Res., 2015, 45, 129–151.

42. L. J. Michot, I. Bihannic, S. Maddi, S. S. Funari, C. Baravian, P. Levitz and P. Davidson, Proc. Natl. Acad. Sci. U.S.A., 2006, 103, 16101.

43. P. H. Michels-Brito, V. Dudko, D. Wagner, P. Markus, G. Papastavrou, L. Michels, J. Breu and J. O. Fossum, Sci. Adv., 2022, 8, eabl8147.

44. G. F. Walker, Clay Minerals Bulletin, 1957, 3, 154–163.

45. J. Środoń, Annu. Rev. Earth Planet. Sci., 1999, 27, 19–53.

46. D. M. Moore and J. Hower, Clays Clay Miner., 1986, 34, 379–384.

47. G. Lagaly, Clays Clay Miner., 1982, 30, 215–222.

48. M. Stöter, B. Biersack, N. Reimer, M. Herling, N. Stock, R. Schobert and J. Breu, Chem. Mater., 2014, 26, 5412–5419.

49. M. W. Möller, D. Hirsemann, F. Haarmann, J. Senker and J. Breu, Chem. Mater., 2010, 22, 186–196.

50. M. Stöter, B. Biersack, S. Rosenfeldt, M. J. Leitl, H. Kalo, R. Schobert, H. Yersin, G. A. Ozin, S. Förster and J. Breu, Angew. Chem. Int. Ed., 2015, 54, 4963–4967.

51. M. Stöter, S. Gödrich, P. Feicht, S. Rosenfeldt, H. Thurn, J. W. Neubauer, M. Seuss, P. Lindner, H. Kalo, M. Möller, A. Fery, S. Förster, G. Papastavrou and J. Breu, Angew. Chem., 2016, 128, 7524–7528.

52. M. Matejdes, M. Stöter, R. Czerwieniec, M. Leitl, S. Rosenfeldt, T. Schumacher, J. Albert, M. Lippitz, H. Yersin and J. Breu, Adv. Opt. Mater., 2021, 9, 2100516.

53. D. R. Lide, CRC Handbook of Chemistry and Physics, CRC Press Inc, Boca Raton, FL, USA, 2003.

54. O. Khoruzhenko, D. R. Wagner, S. Mangelsen, M. Dulle, S. Förster, S. Rosenfeldt, V. Dudko, K. Ottermann, G. Papastavrou, W. Bensch and J. Breu, J. Mater. Chem. C, 2021, 9, 12732–12740.

55. C. F. Dai, O. Khoruzhenko, C. Zhang, Q. L. Zhu, D. Jiao, M. Du, J. Breu, P. Zhao, Q. Zheng and Z. L. Wu, Angew. Chem. Int. Ed., 2022, 61, e202207272.

56. A. A. Sonin, Liq. Cryst. Rev., 2018, 6, 109–128.

57. S. Singh, Liquid Crystals: Fundamentals, World Scientific Publishing Company, Singapore, 2002.

58. G. Meier, E. Sackmann and J. G. Grabmaier, Applications of Liquid Crystals, Springer, Berlin, Germany, 2012.

59. T. Kato, J. Uchida, T. Ichikawa and T. Sakamoto, Angew. Chem. Int. Ed., 2018, 57, 4355–4371.

60. J.-C. P. Gabriel, F. Camerel, B. J. Lemaire, H. Desvaux, P. Davidson and P. Batail, Nature, 2001, 413, 504–508.

61. P. Davidson and J.-C. P. Gabriel, Curr. Opin. Colloid Interface Sci., 2005, 9, 377–383.

62. P. Davidson, C. Penisson, D. Constantin and J.-C. P. Gabriel, Proc. Natl. Acad. Sci. U.S.A., 2018, 115, 6662–6667.

63. F. Brochard and P. G. de Gennes, J. Phys., 1970, 31, 691–708.

64. K. Binnemans, Y. G. Galyametdinov, R. Van Deun, D. W. Bruce, S. R. Collinson, A. P. Polishchuk, I. Bikchantaev, W. Haase, A. V. Prosvirin, L. Tinchurina, I. Litvinov, A. Gubajdullin, A. Rakhmatullin, K. Uytterhoeven and L. Van Meervelt, J. Am. Chem. Soc., 2000, 122, 4335–4344.

65. Y. J. Liu, G. Y. Si, E. S. P. Leong, N. Xiang, A. J. Danner and J. H. Teng, Adv. Mater., 2012, 24, OP131–OP135.

66. R. Bitar, G. Agez and M. Mitov, in Proceedings Volume 8475, Liquid Crystals XVI, SPIE, 2012, vol. 8475, p. 847503.

67. M. Wang, L. He, S. Zorba and Y. Yin, Nano Lett., 2014, 14, 3966–3971.

68. A. Choudhary, G. Singh and A. M. Biradar, Nanoscale, 2014, 6, 7743–7756.

69. Y. Galyametdinov, M. A. Athanassopoulou, K. Griesar, O. Kharitonova, E. A. Soto Bustamante, L. Tinchurina, I. Ovchinnikov and W. Haase, Chem. Mater., 1996, 8, 922–926.

70. A. Mertelj, D. Lisjak, M. Drofenik and M. Čopič, Nature, 2013, 504, 237–241.

71. R. Sahoo, M. V. Rasna, D. Lisjak, A. Mertelj and S. Dhara, Appl. Phys. Lett., 2015, 106, 161905.

72. C. Cîrtoaje, E. Petrescu, C. Stan and D. Creangă, Physica E, 2016, 79, 38–43.

73. A. Mertelj and D. Lisjak, Liq. Cryst. Rev., 2017, 5, 1–33.

74. M. Mur, J. A. Sofi, I. Kvasić, A. Mertelj, D. Lisjak, V. Niranjan, I. Muševič and S. Dhara, Opt. Express, 2017, 25, 1073–1083.

75. M. Hähsler, I. Appel and S. Behrens, Physical Sciences Reviews, 2020, DOI: 10.1515/psr-2019-0090.

76. C. L. Nehl and J. H. Hafner, J. Mater. Chem., 2008, 18, 2415–2419.

77. S. Khatua, P. Manna, W.-S. Chang, A. Tcherniak, E. Friedlander, E. R. Zubarev and S. Link, J. Phys. Chem. C, 2010, 114, 7251–7257.

78. X. Huang and M. A. El-Sayed, J. Adv. Res., 2010, 1, 13–28.

79. J. Jeevanandam, A. Barhoum, Y. S. Chan, A. Dufresne and M. K. Danquah, Beilstein J. Nanotechnol., 2018, 9, 1050.

80. B. Auguié and W. L. Barnes, Phys. Rev. Lett., 2008, 101, 143902.

81. M. Coey, K. Ackland, M. Venkatesan and S. Sen, Nat. Phys., 2016, 12, 694–699.

82. Y.-R. Zhen, K. H. Fung and C. T. Chan, Phys. Rev. B, 2008, 78, 035419.

83. M. Knobel, W. C. Nunes, L. M. Socolovsky, E. De Biasi, J. M. Vargas and J. C. Denardin, J. Nanosci. Nanotechnol., 2008, 8, 2836–2857.

84. C. P. Bean and J. D. Livingston, J. Appl. Phys., 1959, 30, S120–S129.

85. J. L. Dormann, L. Bessais and D. Fiorani, J. Phys. C: Solid State Phys., 1988, 21, 2015.

86. W. H. Meiklejohn and C. P. Bean, Physical Review, 1957, 105, 904–913.

87. M. Mikhaylova, D. K. Kim, N. Bobrysheva, M. Osmolowsky, V. Semenov, T. Tsakalakos and M. Muhammed, Langmuir, 2004, 20, 2472–2477.

88. A. M. Funston, C. Novo, T. J. Davis and P. Mulvaney, Nano Lett., 2009, 9, 1651–1658.

89. T. Chen, M. Pourmand, A. Feizpour, B. Cushman and B. M. Reinhard, J. Phys. Chem. Lett., 2023, 4, 2147.

90. R. T. Hill, J. J. Mock, A. Hucknall, S. D. Wolter, N. M. Jokerst, D. R. Smith and A. Chilkoti, ACS Nano, 2012, 6, 9237–9246.

91. P. K. Jain, W. Huang and M. A. El-Sayed, Nano Lett., 2007, 7, 2080–2088.

92. E. Rabani, D. R. Reichman, P. L. Geissler and L. E. Brus, Nature, 2003, 426, 271–274.

93. M. Grzelczak, J. Vermant, E. M. Furst and L. M. Liz-Marzán, ACS Nano, 2010, 4, 3591–3605.

94. A. Böker, J. He, T. Emrick and T. P. Russell, Soft Matter, 2007, 3, 1231–1248.

95. A. K. Boal, F. Ilhan, J. E. DeRouchey, T. Thurn-Albrecht, T. P. Russell and V. M. Rotello, Nature, 2000, 404, 746–748.

96. K. Ament, D. R. Wagner, T. Götsch, T. Kikuchi, J. Kröhnert, A. Trunschke, T. Lunkenbein, T. Sasaki and J. Breu, ACS Catal., 2021, 11, 2754–2762.

97. K. Ament, N. Köwitsch, D. Hou, T. Götsch, J. Kröhnert, C. J. Heard, A. Trunschke, T. Lunkenbein, M. Armbrüster and J. Breu, Angew. Chem. Int. Ed., 2021, 60, 5890–5897.

98. K. Ament, D. R. Wagner, F. E. Meij, F. E. Wagner and J. Breu, Z. Anorg. Allg. Chem., 2020, 646, 1110–1115.

99. D. Rus and M. T. Tolley, Nature, 2015, 521, 467–475.

100. L. Montero de Espinosa, W. Meesorn, D. Moatsou and C. Weder, Chem. Rev., 2017, 117, 12851–12892.

101. S. Armon, E. Efrati, R. Kupferman and E. Sharon, Science, 2011, 333, 1726–1730.

102. E. Palleau, D. Morales, M. D. Dickey and O. D. Velev, Nat. Commun., 2013, 4, 1–7.

103. X. Peng, T. Liu, Q. Zhang, C. Shang, Q.-W. Bai and H. Wang, Adv. Funct. Mater., 2017, 27, 1701962.

104. I. Burgert and P. Fratzl, Philos. Trans. Royal Soc. A, 2009, 367, 1541–1557.

105. A. Sydney Gladman, E. A. Matsumoto, R. G. Nuzzo, L. Mahadevan and J. A. Lewis, Nat. Mater., 2016, 15, 413–418.
106. Q. L. Zhu, C. F. Dai, D. Wagner, O. Khoruzhenko, W. Hong, J. Breu, Q. Zheng and Z. L. Wu, Adv. Sci., 2021, 8, 2102353.
107. Q. L. Zhu, C. Du, Y. Dai, M. Daab, M. Matejdes, J. Breu, W. Hong, Q. Zheng and Z. L. Wu, Nat. Commun., 2020, 11, 1–11.
108. Q. L. Zhu, C. F. Dai, D. Wagner, M. Daab, W. Hong, J. Breu, Q. Zheng and Z. L. Wu, Adv. Mater., 2020, 32, 2005567.
109. A. W. Hauser, A. A. Evans, J.-H. Na and R. C. Hayward, Angew. Chem. Int. Ed., 2015, 54, 5434–5437.
110. Y. Ueoka, J. Gong and Y. Osada, J. Intell. Mater. Syst. Struct., 1997, 8, 465–471.

RESULTS

COLLOIDALLY STABLE, MAGNETORESPONSIVE LIQUID CRYSTALS BASED ON CLAY NANOSHEETS

Olena Khoruzhenko,[a] Daniel R. Wagner,[a] Sebastian Mangelsen,[b] Martin Dulle,[c] Stephan Förster,[c] Sabine Rosenfeldt,[a] Volodymyr Dudko, Katharina Ottermann,[d] Georg Papastavrou ,[d] Wolfgang Bensch [b]* and Josef Breu [a]*

* Corresponding authors

[a] Department of Chemistry and Bavarian Polymer Institute, University of Bayreuth, Universitätsstr. 30, 95440 Bayreuth, Germany

[b] Institute of Inorganic Chemistry, Christian-Albrechts University Kiel, 24118 Kiel, Germany

[c] JCNS-1/IBI-8: Neutron Scattering and Biological Matter, Forschungszentrum Jülich Gmbh, Wilhelm-Johnen-Straße, 52428 Jülich, Germany

[d] Department of Physical Chemistry II and Bavarian Polymer Institute, University of Bayreuth, Universitätsstr. 30, Bayreuth, Germany

Published in J. Mater. Chem. C 9, 12732 (2021).

Journal of Materials Chemistry C

ROYAL SOCIETY OF CHEMISTRY

PAPER

View Article Online
View Journal | View Issue

Cite this: J. Mater. Chem. C, 2021, 9, 12732

Colloidally stable, magnetoresponsive liquid crystals based on clay nanosheets†

Olena Khoruzhenko,[a] Daniel R. Wagner,[a] Sebastian Mangelsen,[b]* Martin Dulle,[c] Stephan Förster,[c] Sabine Rosenfeldt,[a] Volodymyr Dudko,[a] Katharina Ottermann,[d] Georg Papastavrou,[d] Wolfgang Bensch[b]* and Josef Breu[a]*

Received 23rd June 2021,
Accepted 18th August 2021

DOI: 10.1039/d1tc02927d

rsc.li/materials-c

Liquid crystalline materials found numerous applications in modern technologies due to their ability to respond to external fields. In this context, ferronematic liquid crystals are fascinating because they offer a response to weak magnetic fields in addition to electrical fields. Nevertheless, the synthesis of stable ferronematic liquid crystals represents a challenge for colloidal and synthetic chemists. In this work, we present a straight-forward strategy for directly incorporating presynthesized magnetic nanoparticles into every other interlayer of synthetic 2 : 1 layered silicates, which subsequently can be swollen to nematic phases simply by immersion into water, offering almost infinite stability. The resulting ferronematic suspension shows a sensitive response to magnetic fields. Moreover, the synthetic strategy is highly modular, enabling for variations of the magnetic nanosheets that allow for tuning the interaction between nanosheets and blocking temperature.

Introduction

Materials capable of responding to various external stimuli are at the heart of most technologies we are using daily. Nevertheless, for the next evolutionary step enabling future technologies, we are looking for materials with multiple stimuli-responsive pathways.[1,2] These materials would potentially show direction-dependent properties that allow for more elaborate functionalities.

Liquid crystals (LC), due to their large dielectric anisotropy, are intrinsically responsive to electrical fields but show only a very weak response to magnetic fields. As the LC state can flow as an ordinary liquid while preserving a long-range order, the constituents can be manipulated at field strengths in the range of k_BT.[3] Magnetic LC (MLC) thus already respond to rather weak applied fields. MLC show orientational order and fluidity, and high magnetic susceptibility.[4] This paves the way to unique physical properties like magneto-optic and magneto-mechanical effects, which one eventually might find in applications within the field of optics, display devices, telecommunications, micro-, smart fluids, photonics, and for many biomedical applications.[5–12]

Ferronematic behavior was predicted in the 1970s in Brochard's and de Gennes's pioneering work.[13] They concluded that a combination of magnetic nanoparticles (MNPs) with a nematic phase such as maghemite (γ-Fe_2O_3), magnetite (Fe_3O_4), or metallic cobalt could be a source of spontaneous magnetization and would dramatically increase the effective director-magnetic field interaction.[13] The first stable ferronematic suspension could, however, not be realized until 2013.[14]

For the preparation of MLC, two strategies are usually exploited. Molecular LC have been converted to MLC by either enhancing the intrinsic magnetic properties of a LC or by incorporating MNPs into the LC.[13,15–18] In the first strategy, LC phase molecules are doped with heavy paramagnetic atoms, rendering them more sensitive to the magnetic field. This method, however, requires not only sophisticated synthetic procedures but it delivers paramagnetic materials that require extremely strong magnetic fields for alignment, limiting its usefulness.[19]

The second strategy applying MNPs yields more field-sensitive MLC, but magnetic dipole–dipole interaction leads to fast aggregation and poor system stability.[19,20] To enhance stability and to avoid segregation of the MLC phase, MNPs were surface modified to enhance compatibility with the molecular LC. Usually, this involves capping of MNPs with a surfactant layer made of ligands with similar mesogenic units as the LC host. In some cases, MNPs were passivated by coating them

[a] Department of Chemistry and Bavarian Polymer Institute, University of Bayreuth, Universitätsstr. 30, 95440 Bayreuth, Germany
[b] Institute of Inorganic Chemistry, Christian-Albrechts University Kiel, 24118 Kiel, Germany
[c] JCNS-1/IBI-8: Neutron Scattering and Biological Matter, Forschungszentrum Jülich Gmbh, Wilhelm-Johnen-Straße, 52428 Jülich, Germany
[d] Department of Physical Chemistry II and Bavarian Polymer Institute, University of Bayreuth, Universitätsstr. 30, 95440, Bayreuth, Germany

† Electronic supplementary information (ESI) available. See DOI: 10.1039/d1tc02927d

View Article Online
Paper Journal of Materials Chemistry C

with an inert inorganic material.[21] For instance, silica coatings have been shown to be capable of stabilizing MNP suspensions.[19] The coating acts as a physical barrier between magnetic nanorods, preventing strong magnetic dipole–dipole interactions. Acidic groups on the silica surface, moreover, exert long-range electrostatic repulsion that contributes to the good dispersibility and stability in different polar solvents.

In summary, the preparation of homogeneous MLC with anisotropic properties and high dispersion stability still represents a significant challenge to both synthetic and colloidal chemists.[22]

A handful of layered compounds like lepidocrocite-type titanates,[23] layered antimony phosphates,[24,25] perovskite-type niobate,[26] or graphene oxide[27] have been shown to osmotically swell. Being a thermodynamically allowed process and repulsive in nature,[28,29] it allows for utter and most gentle delamination into nanosheets of uniform thickness. With diameters in the μm range, the obtained nanosheets possess large aspect ratios, and rotation of the nanosheets in suspension is hindered. Even very dilute dispersions of the charged nanosheets adopt a cofacial arrangement due to strong electrostatic repulsion. In this nematic state, adjacent nanosheets are held in a coherent cofacial geometry but are separated by long distances determined by the clay content, typically exceeding 50 nm (see Fig. 2d in ref. 30), enabling incorporation of nanoparticles. Amongst the known nanosheet-LCs, synthetic fluorohectorite is unique for allowing production of heterostructures where such nanoparticles can exclusively be incorporated into every second interlayer, which results in delamination into nematic phases of double stacks (Fig. 1).[31] Within these double stacks (DS), nanoparticles are sandwiched between two 1 nm thick silicate layers and thus resemble to some extent the above-cited coating approach. The difference being that the large aspect ratio of the coating also gives rise to the LC state.

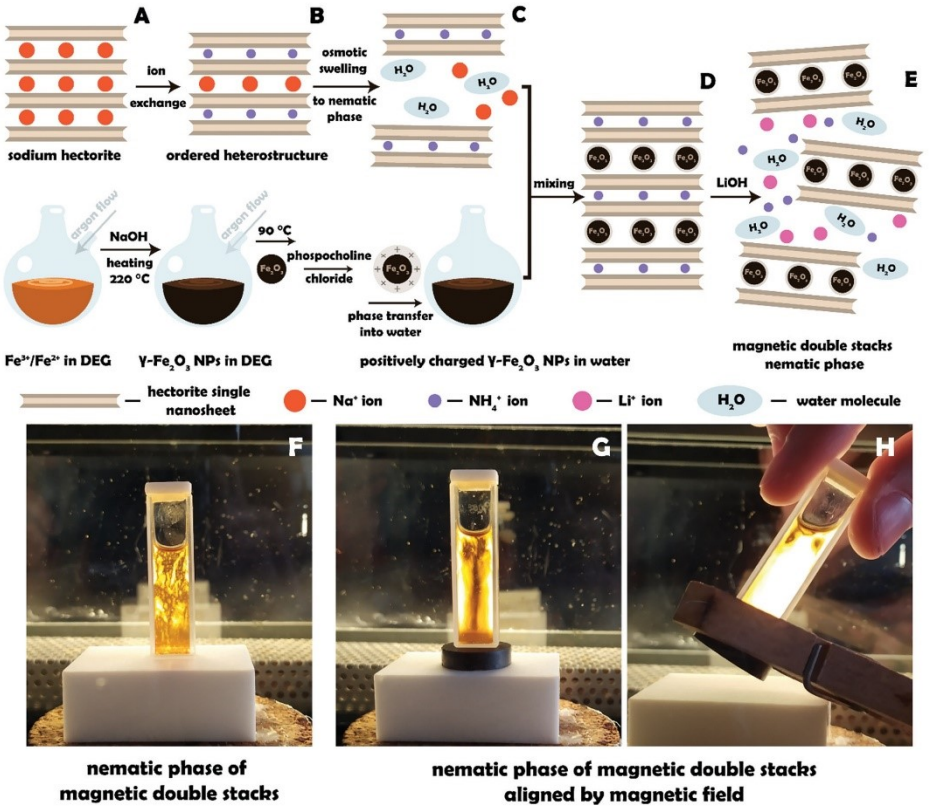

Fig. 1 Schematic illustration of the MDS preparation procedure. (A) Sodium hectorite structure. (B) Ordered heterostructures. (C) Osmotic swelling of ordered heterostructures yields a nematic phase of NH_4^+-DS. (D) Heterostructures with strict alternation NH_4^+ and γ-Fe_2O_3 interlayers. (E) MDS nematic phase (F) photo of nematic LC phase of MDS with a concentration of 0.2 wt% under cross polarised light. (G) and (H) Images of MDS aligned by a magnetic field with different orientations.

View Article Online
Journal of Materials Chemistry C Paper

In this paper, we describe the fabrication of ordered heterostructures of fluorohectorite with nanoparticulate maghemite and its osmotic swelling in an aqueous dispersion to a nematic phase comprised of magnetic nanosheets. In a sense, this approach combines the best aspects of both known strategies to fabricate colloidally stable, anisotropic magnetoresponsive liquid crystals.

Results and discussion

Synthetic strategy

Synthetic sodium fluorohectorite (Na-hectorite, $[Na_{0.5}]^{inter}[Mg_{2.5}Li_{0.5}]^{oct}[Si_4]^{tet}O_{10}F_2$) belongs to a handful of layered compounds that show the long-known,[32] but rare phenomenon of osmotic swelling[23–25,33,34] producing a liquid crystalline phase. The highly-charged nanosheets with a huge aspect ratio (20 000 nm diameter, 1 nm thickness)[35] are separated to a uniform distance when immersed into deionized water.[28,29] Even very dilute suspensions ($\approx$0.3 wt%) of such high aspect ratio nanosheets are not isotropic but represent nematic phases as evidenced by a rational 00*l* series (Fig. S1, ESI†) being observed in small-angle X-ray scattering (SAXS) curves.[30,35]

The randomly oriented domains of the nematic suspension can easily be orientated into a monodomain or any sophisticated pattern by applying appropriate external electric fields.[36,37]

The nematic phases of Na-hectorite can be loaded with nanoparticles like maghemite (γ-Fe_2O_3)[38] or palladium,[39] whereupon the structure's collapse leads to encapsulation of the nanoparticles.

Na-hectorite, moreover, can be converted to ordered heterostructures by simple partial ion exchange following a published procedure.[31] Briefly, a NH_4Cl solution was added in an appropriate quantity (69% of the cation exchange capacity (CEC)) to Na-hectorite in a 3 to 1 ethanol–water mixture. Upon equilibration in an overhead shaker overnight, Na^+ is replaced in every other interlayer by NH_4^+ in a strictly alternating fashion (Fig. 1B and Fig. S5, ESI†). Due to its lower hydration enthalpy, NH_4^+ blocks osmotic swelling in every other interlayer while the Na^+ interlayers will still swell infinitely. Thus upon immersion into water, a nematic phase of DS forms with NH_4^+ acting as glue for two silicate layers (Fig. 1C) yielding a total height of 2.4 nm (Fig. S6, ESI†). At 1 wt%, the DS are separated to 100 nm in the nematic suspension allowing for incorporation of nanoparticles with positive surface potential *via* a quasi-ion exchange.

Next magnetic nanoparticles (γ-Fe_2O_3) were synthesized by applying the polyol method and were characterized as previously published in detail.[38] Since a positive ζ-potential is required for quasi-ion-exchange[40] into the galleries between the negatively charged hectorite nanosheets, phosphocholine was added as capping ligand (ζ = +42 mV at pH 7; Fig. S2B, ESI†). This capping ligand also allows for transfer of the maghemite nanoparticles into water.

According to the transmission electron microscope (TEM) graphs, the maghemite nanoparticles have a spherical shape and a diameter of 5.5 $\pm$ 1.1 nm with a low polydispersity (Fig. S2A, C and D, ESI†). Dynamic light scattering measurement (DLS) indicates a hydrodynamic radius of 6.9 $\pm$ 1.3 nm (Fig. S2A, ESI†). Powder X-ray diffraction (XRD) (Fig. S3, ESI†) confirms the spinel-type maghemite (γ-Fe_2O_3) phase. No reflections of hematite or any other crystalline iron oxide phase were observed and the phase purity is confirmed by Mößbauer spectra (Fig. S4, ESI†).

Next, the nematic DS suspension and the aqueous maghemite suspension were combined. Typically, a 1 wt% aqueous dispersion of DS was added to 0.1 wt% of maghemite dispersion under vigorous stirring. The volume of maghemite dispersion was varied to get the desired weight compositions. The huge gallery separation allows for fast diffusion and incorporation of the positively charged nanoparticles while triggering heterocoagulation into dense heterostructures where NH_4^+ and γ-Fe_2O_3 interlayers strictly alternate (Fig. 1D). While at stage D a highly ordered, crystalline heterostructure is obtained, this does not yet swell to a liquid crystalline phase because the hydration enthylpy of the NH_4^+ cation in the interlayer space is too low. In order to form the liquid crystalline phase, NH_4^+ ion needs first to be replaced with Li^+ showing a high hydration enthalpy.

In the following step, the NH_4^+ interlayers in the ordered heterostructure are activated again for osmotic swelling. This is achieved by ion exchange with LiOH. At the high pH provided by LiOH (pH > 10), the NH_4^+ gets deprotonated and evaporates from the solution at 60 °C. At this point, Li^+ is exchanged into the former NH_4^+ interlayers, but the Li^+ interlayers do not swell osmotically, given the high ionic strength.

After repeated centrifugation and redispersion reducing the ionic strength, the ordered Li^+/γ-Fe_2O_3 heterostructure, however, eventually delaminates into a nematic suspension of magnetic DS (MDS) where γ-Fe_2O_3 nanoparticles are sandwiched between two silicate layers (Fig. 1E)

The individual MDS nanosheets are separated by water layers acting as a dielectric medium that modulates the long-range electrostatic repulsion between MDS. Nematic suspension of MDS shows a fast response to an external magnetic field (Fig. 1G, H and Movie S1, Fig. S15, ESI†). Without magnetic field nematic phase's color of MDS suspension stays unchanged (Fig. S16, ESI†).

Obviously, individual delaminated MDS only persist while being dispersed. In the following, some analytical techniques involve dried powders of the nematic suspensions. Upon drying, the MDS are, however, forced to restack into heterostructures of Li^+ and γ-Fe_2O_3 interlayers.

The resulting height of MDS is expected to be around 7–9 nm ($\approx$5.5 nm nanoparticle height + 2 $\times$ 1 nm silicate nanosheet), which was confirmed by atomic force microscopy (AFM) (Fig. 2A), showing a thickness of 8.5 nm. TEM images of cross sections of restacked MDS, which were prepared by microtoming, confirm the strict alteration of γ-Fe_2O_3 monolayers separated by two silicates layers with Li^+ in the interlayer space (Fig. 2B and grayscale analysis Fig. S10, ESI†). Please note that the microtome cutting alters the structures in a way that causes the structures to appear curved and results in a large portion of nanoparticles at the edge to be pulled out by the

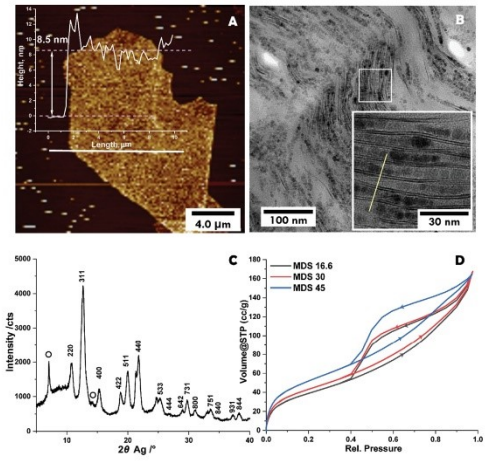

Fig. 2 MDS structural characterization (A) the topographic AFM image of the single MDS nanosheets with the insert of the height profile (B) cross-sectional TEM image of MDS. The inset shows the magnification of highly loaded nanosheets with the periodic nanoparticle-nanosheets arrangement. The yellow line was used for greyscale analysis (Fig. S10, ESI†). (C) Wide-angle PXRD pattern of MDS. Characteristics hectorite peaks marked with circles. (D) Nitrogen adsorption/desorption isotherms of MDS with different loading of nanoparticles.

blade.[41] The thickness of the MDS, and hence the periodicity, varies slightly along the stacking direction as the nanoparticles are not strictly monomodal. Averaging over at least three MDS (line in the inset of Fig. 2C), an average periodicity of 7.8 nm was calculated, which is in decent agreement with the sum of the average nanoparticle diameter and 2 times the thickness of the silicate nanosheet. The packing density of y-Fe_2O_3 nanoparticles can be better spotted with TEM images taken from the top (Fig. S7, ESI†).

PXRD of MDS feature maghemite peaks (indexed in Fig. 2C) in addition to the hectorite reflections. Hectorite peaks (marked by a circle in Fig. 2C) may be indexed as 02/11 and 06 bands deriving from the 2D crystal structure of the nanosheets in the *ab*-plane while the relative position along the *c*-direction is disordered due to the variation of interlayer height defined by the nanoparticle diameter.

By varying the ratio of magnetic nanoparticles to hectorite, it is possible to obtain different MNP loadings of MDS. By inductively coupled plasma atomic absorption spectroscopy (ICP-OES), the resulting nominal formula for the sample with an expected loading of 16.6 wt%, 30 wt%, and 45 wt% of y-Fe_2O_3 nanoparticles (referred to as MDS 16.6, MDS 30 and MDS 45) are $(Fe_2O_3)_{0.46}Li_{0.31}(Mg_{2.5}Li_{0.5}Si_4O_{10}F_2)$, $(Fe_2O_3)_{1.05}Li_{0.31}(Mg_{2.5}Li_{0.5}Si_4O_{10}F_2)$ and $(Fe_2O_3)_{1.95}Li_{0.31}(Mg_{2.5}Li_{0.5}Si_4O_{10}F_2)$, respectively. Experimentally determined compositions are in close agreement with the expected loading of y-Fe_2O_3 (Table S1, ESI†).

The Na^+/NH_4^+ heterostructures showed no mesoporosity (type 2 adsorption isotherm according to IUPAC classification, Fig. S8, ESI†).[42] The small micropore volume at low partial pressure most likely is related to fringed edges of the stacks. Upon incorporation of y-Fe_2O_3 nanoparticles, the N_2 adsorption/desorption isotherms changed to H3 type with a hysteresis loop, indicating a mesoporous structure (Fig. 2D). The nanoparticles are apparently not densely packed and act as a pillar between the silicate nanosheets, creating slit-shaped mesopores between them. The height of the slit should correspond to the nanoparticle size, while the width is expected to vary with loading if the nanoparticles are uniformly distributed. Since no kernel is available for slit pores,[43] we applied the DFT kernel for spherical pores, which gave a rather broad pore size distribution with a maximum at 5.5 nm (Fig. S9, ESI†), in agreement with the pristine nanoparticles diameter. The curve is, however too noisy to estimate an accurate slit width. Since the nanoparticle surface contributes to the total surface area as long as they are accessible, the BET surface area is expected to increase with loading, which was confirmed experimentally with 141.6 $m^2 g^{-1}$, 156.0 $m^2 g^{-1}$, and 188.3 $m^2 g^{-1}$ for MDS 16.6, MDS 30, and MDS 45, respectively.

Small-angle X-ray scattering in the magnetic field

Orientation under magnetic field was monitored by SAXS. The 2D pattern of nematic suspensions of MDS was strongly anisotropic (Fig. 3A and B), which indicated preferred orientation of the nematic domains. Since at concentrations applied for SAXS (4 wt%) the suspensions are already quite viscous, the shear forces inherent during capillary loading therefore already induced some degree of orientation (Fig. 3A and B). In the magnetic field the majority of the MDS is oriented with the nematic director perpendicular to the magnetic field yielding an order parameter $S = 0.7$ (Fig. 3C and D). Adjacent MDS are shifted relative to each other in the plane of orientation/field,

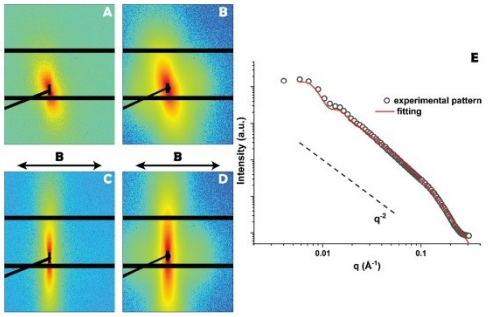

Fig. 3 2D SAXS pattern of 4 wt% aqueous dispersion of MDS 16.6 recorded without magnetic field applied and with the detector set at low (A) and high (B) *q*-value: 2D SAXS pattern of 4 wt% aqueous dispersion of MDS 16.6 recorded with the magnetic field applied and with the detector set at low (C) and high (D) *q*-value. Vector *B* indicates the direction of applied magnetic field. (E) Angle averaged 1D SAXS pattern derived from (C) and (D) in the direction perpendicular to the applied magnetic field together with the fitting.

View Article Online
Journal of Materials Chemistry C Paper

resulting in band-like structures, which in the literature is referred to as quasi chainlike.[44]

When transforming the 2D data to 1D with the radial distributions in conjunction the scattering of the nematic liquid crystal director, no rational 00*l* series originating from the quasi-crystalline lamellar form factor became apparent (Fig. 3E). This indicates that unlike in the ordered NH_4^+ DS (Fig. S1, ESI†), the separation of adjacent MDS varies considerably in the MDS suspensions. The very weak 00*1* peak observed at the $q = 0.0072$ Å^{-1} corresponds to 87 nm separation between adjacent nanosheets.

As expected for nanosheets, at intermediate q values the intensity $I(q)$ is proportional to q^{-2}, where q is the magnitude of the scattering vector and 2 is the fractal exponent of the scattering object. In case of the well oriented MDS we also were able to separate the scattering of the embedded particles from the sheets. This enabled us to determine their packing fraction within the layer to be 0.4. The calculation for the order parameter, the fit as well data reduction procedures can be found in the ESI.†

Magnetic properties of restacked MDS films

Nanoparticles of y-Fe_2O_3 are well known to show superparamagnetic behavior.[45–48] Their spatial separation can tune the interaction of superparamagnetic nanoparticles. In the MDS case presented here, the particles are arranged in a highly anisotropic fashion with different in-plane and out-of-plane distances. As shown above, the MDS in the nematic LC phase respond to an applied magnetic field. This phenomenon calls for a more detailed study of the MDS magnetic properties. For this, MDS suspensions were drop casted on Kapton foil, whereupon solvent evaporation, highly oriented films with MDS nanosheets parallel to the support were obtained. The magnetic properties of these oriented films were studied by both DC and AC field magnetization measurements. First, we examine the isothermal, field-dependent magnetic properties. The magnetization (M) was measured as a function of the applied magnetic field (H) at a temperature (T) of 2 and 300 K with the films oriented parallel and perpendicular to H, respectively. The data of the MDS 45 film are presented in Fig. 4A.

At $T = 300$ K, no remanent magnetization is discernible for both field orientations, indicating superparamagnetic behavior. The hysteresis loops show the typical s-shape with a rapid increase of M in low magnetic fields where 90% of the saturation magnetization (M_S) is reached at $\mu_0 H = 1$ T. At 2 K, a clear magnetic hysteresis can be observed. Most strikingly, the magnetization process is highly dependent on the field orientation, albeit the particles themselves are spherical. The anisotropy indicates that the MDS were deposited in a highly oriented fashion and that the individual MDS are magnetically anisotropic. An easy plane of magnetization is evident from the data, which can be deduced from M being higher at a given applied magnetic field for in-plane field orientation as compared to the out-of-plane orientation. When comparing the behavior of samples with different loadings of y-Fe_2O_3 (see Fig. 4B), it becomes obvious

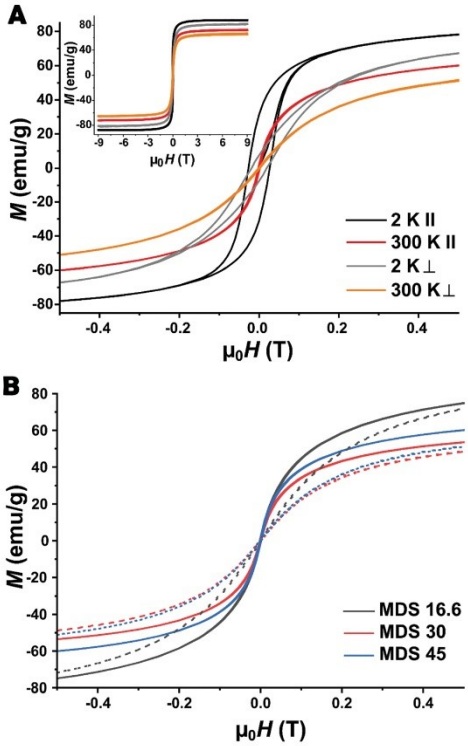

Fig. 4 (A) $M(H)$ curves for magnetic fields up to 0.5 T collected on the MDS 45 film at temperatures and magnetic field orientations as indicated. The inset shows the data for the full range of magnetic fields. (B) Comparison of the data collected at $T = 300$ K for samples with different loadings of y-Fe_2O_3. Solid lines correspond to H being parallel to the film plane; dotted lines correspond to perpendicular orientation.

that all samples show this kind of magnetic anisotropy. The value of M_S (in-plane orientation) differs among the samples with 72, 64, and 92 emu g^{-1} for the films of MDS 45, MDS 30, and MDS 16.6, respectively. For comparison, bulk y-Fe_2O_3 has an M_S of 76 emu g^{-1}.[49] Other samples of y-Fe_2O_3 with similar size show significantly smaller values for M_S (47–62 emu g^{-1}).[45,46] The variations among the samples appear non-systematic and can be ascribed to the significant errors in calculating the mass of y-Fe_2O_3 given the low overall sample mass of a few mg.

We now turn to the temperature-dependent magnetic properties. Magnetic nanoparticles show superparamagnetic relaxation, *i.e.*, the magnetic moment of the single domain particles fluctuates at elevated temperatures, but upon cooling, the thermally activated process is frozen. Besides the nature of the NPs themselves, their interaction plays a crucial role in the blocking temperature, where freezing occurs.[50] This can be studied using AC-susceptibility; corresponding data for the real and imaginary part (χ' and χ'') are shown in Fig. 5. The sample

View Article Online
Paper Journal of Materials Chemistry C

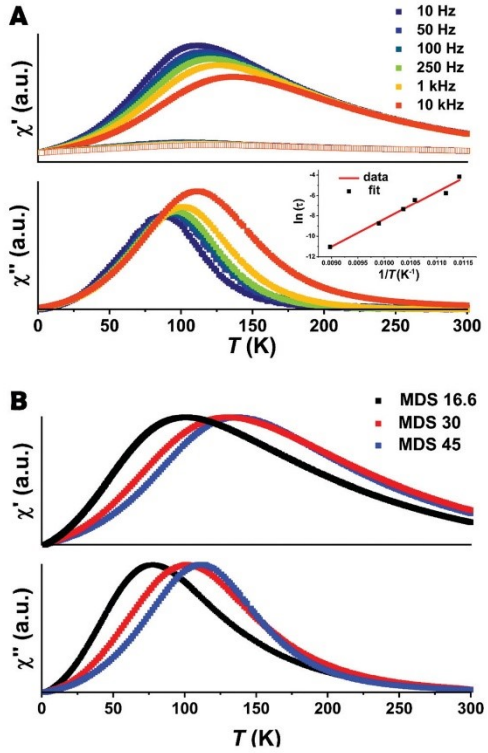

Fig. 5 (A) Real and imaginary parts (χ' and χ'') of the AC susceptibility as a function of temperature measured in zero DC field with f_{AC} as indicated for the MDS 45 sample and in-plane field orientation. The χ' signal measured for out-of-plane field orientation is shown for comparison. The inset shows a fit of the Arrhenius law to the observed maxima in χ''. (B) Comparison of the data collected for the samples with different loading with f_{AC} = 10 kHz and in-plane field orientation.

is excited with a low magnitude (10 Oe) oscillating magnetic field of a given frequency f_{AC} in zero DC field for the experiment. At room temperature in the superparamagnetic state, the magnetic moment can easily follow the AC field. However, due to the finite activation energy of the magnetization switching, blocking of this process will occur when the sample is cooled down.[51] The frequency dependence of χ' and χ'' shown in Fig. 5A (MDS 45 with parallel field orientation) is typical for SPM behaviour:[51] the blocking temperature decreases with f_{AC} since the magnetic moment has more time to follow the excitation. Also, in this experiment, a strong anisotropy of the samples in respect to the magnetic field is evident. In Fig. 5A, χ' measured with out-of-plane orientation was found to be a factor of $\sim$6 lower than for the in-plane orientation. Anisotropy can be observed systematically for all three samples. From the maxima in χ'', activation energy for the spin switching can be determined according to the Arrhenius law $\tau = \tau_0 \exp(\Delta E/kT)$ with the relaxation time τ, the characteristic time τ_0, activation energy ΔE and Boltzmann's constant k.[51] A fit of the data to this law is shown in the inset of Fig. 5A. The loading of y-Fe_2O_3 particles in the films significantly influences the activation energy, as outlined in Fig. 5B. Here the data for χ' and χ'' are displayed for the three samples at fixed f_{AC} = 10 kHz. A significant shift of the maxima towards higher temperatures (99 to 137 K at f_{AC} in χ') with increasing nanoparticle loading is evident. The activation energies determined as $\Delta E/k$ for MDS 16.6, MDS 30, and MDS 45 are 1162 ($\pm$ 170), 1564 ($\pm$ 90), and 2685 ($\pm$ 190) K, respectively. Examples of neat maghemite NPs of similar size are 737 K and 3800 K.[47,48] However, the energy barriers are highly dependent on the actual system and particle arrangement. The characteristic time τ_0 determined for the three samples ranges from 1.1 $\times$ 10^{-11} s (MDS 16.6) to 5.3 $\times$ 10^{-16} s (MDS 45). The latter value is much higher than those commonly observed for SPM systems (10^{-9}–10^{-11} s), indicating the onset of spin glass-like behavior, which is in line with the increased inter-particle interaction.[51]

The systematic increase of ΔE with particle concentration demonstrates that the particles' interaction strength is effectively tuned by varying their intralayer (in-plane) distance. This conclusion can be drawn due to the well-defined and loading-independent interlayer spacing given by the hectorite layers. The pronounced magnetic anisotropy of the MDS nicely explains the observed spontaneous alignment of nematic domains in a magnetic field as evidenced by the SAXS data. Since the y-Fe_2O_3 nanoparticles are spherical, a preferred alignment and a specific crystallographic orientation (and thus easy magnetic axis) between the layers due to their shape do not appear reasonable. Instead, we speculate that the observed easy plane of magnetization is due to a preferred in-plane coupling of the particle's magnetic moments. According to TEM images, the distance in the cross-plane direction between nanoparticles is >2 nm, while the in-plane distance is considerably smaller (Fig. S7, ESI†), leading to the stronger in-plane coupling as a direct consequence of the MDS architecture. This magnetic anisotropy should become even more pronounced in the LC state when the cross-plane distance between adjacent MDS becomes tens or hundreds of nanometers, making the cross-plane coupling negligible.

Conclusions

In conclusion, we propose a straight forward method for fabricating stimulus-responsive colloids with pronounced anisotropic nanosheet shape and tuneable interparticle interaction. This allows for varying the magnetic properties without alternating the morphology nor sacrificing colloidal stability of the LC and without altering the chemistry of magnetic nanosheets.

The resulting ferronematic suspension is not only infinitely stable in water but also requires a very low concentration of the magnetic nanosheets to show LC behavior. Simply by tuning the starting ratio of the components (hectorite and nanoparticles), the interaction strength of the y-Fe_2O_3 NPs in the restacked MDS films can be tuned. This is evident from the

View Article Online
Journal of Materials Chemistry C Paper

activation energy for switching the magnetic moment increasing from 1162 K to 2685 K from low to high NPs loading. The restacked MDS films show a highly anisotropic magnetic response, which points to an artificial easy plane being introduced by the composite's architecture. This serves as a tentative explanation for the ferronematic suspension's response to a magnetic field.

This approach is not limited to synthetic hectorite and maghemite nanoparticles. The synthetic strategy can be adopted to other nanosheets capable of showing repulsive osmotic swelling. Additionally, there is no limit on the type of nanoparticles, which could be used to create ferronematics.

Experimental section

Synthesis of sodium hectorite

Sodium hectorite ($[Na_{0.5}]^{inter}[Mg_{2.5}Li_{0.5}]^{oct}[Si_4]^{tet}O_{10}F_2$, Na-hectorite) was obtained by melt synthesis followed by long-term annealing according to a published procedure.[35] The material featured a cation exchange capacity (CEC) of 1.27 mmol g^{-1} and a density of 2.73 g cm^{-3}.

Synthesis of ordered heterostructures

Ordered heterostructures were synthesized according to a published procedure.[31] First, 1.5 g Na-hectorite was immersed in 250 ml of a water-ethanol mixture (75 vol% ethanol) for 12 h at room temperature in an overhead shaker. Then, 70.3 mg of NH_4Cl, corresponding to 69% of the CEC of Na-hectorite, was dissolved in 100 ml of a water–ethanol mixture (75 vol% ethanol) and added to Na-hectorite under vigorous stirring followed by equilibration in the overhead shaker overnight at room temperature. The resulting solid was washed five times with the same ethanol–water mixture and collected *via* centrifugation at 8000 rpm for 10 min. During washing and centrifugation, an iridescent gel formed. After centrifugation at 6000 rpm for 1 min, the iridescent gel was decanted, 250 ml of MQ water was added, and the sample was equilibrated for two days. The resulting gel was washed three times with deionized water by centrifugation at 10 000 rpm for 15 min and dried in the oven at 60 °C.

Synthesis of y-Fe_2O_3 nanoparticles

Nanoparticles were synthesized according to a published procedure.[38] $FeCl_3 \times 6H_2O$ (1,05 g, 2.00 mmol) and $FeCl_2 \times 4H_2O$ (398 mg, 1.00 mmol) were dissolved in 40.0 g diethylene glycol (DEG). NaOH (640 mg, 16.0 mmol) in 80.0 g DEG was added, and the solution was degassed under a flow of argon for 3 h. The solution was heated to 220 °C with a ramp of 2 K min^{-1} and kept at this temperature for 2 h. The dispersion was allowed to cool to 90 °C, and phosphocholine chloride calcium salt tetrahydrate (330 mg, 1.00 mmol) in 20.0 g DEG was rapidly added under vigorous stirring. The temperature was kept for 1 h and then cooled to room temperature. The particles were precipitated in 600 mL of acetone, washed twice with 400 mL of acetone, and then redispersed in water. The dispersion was dialyzed in 4 L of water for 48 h, with water being exchanged after 6 and 24 h. $FeCl_2 \times 4H_2O$ (98%), $FeCl_3 \times 6H_2O$ (≥99%), NaOH (pellets, ≥98%), and diethylene glycol (99%) were purchased from Sigma Aldrich. Phosphocholine chloride calcium salt tetrahydrate (98%) was purchased from abcr GmbH. The water used was of MilliQ quality (18.2 MΩ).

Synthesis of magnetic double stacks

DS were delaminated as 1 wt% dispersion in water. For the intercalation, the pH of both DS and nanoparticle dispersions was adjusted to pH 7. The nematic suspension of DS was rapidly added to nanoparticle dispersion volume (0.1 wt%) under stirring. The volume of nanoparticle dispersions was varied according to the desired composition of MDS. The flocculate was collected by a magnet and washed 3 times with water. Freshly prepared LiOH solution with pH 10 was added to the flocculated gel, and the dispersion was stirred for 15 minutes. This procedure was repeated twice with fresh LiOH solution. After centrifugation, the precipitate was transferred into an Erlenmeyer flask with 600 ml LiOH (pH 10) and heated to 60 °C over night under argon flow. The cleaved double stacks were collected *via* centrifugation, washed several times with water, and freeze-dried.

Powder X-ray diffraction measurements (PXRD) were done with an STOE Stadi P diffractometer in Debye–Scherrer geometry applying monochromatic Ag $K_{\alpha 1}$ radiation and a MYTHEN2 4K detector (4 MYTHEN2 R 1K Si-strip detector modules) in stationary mode. Samples were charged into 0.5 mm glass capillaries (Hilgenberg, code 4007605).

Transmission electron microscopy (TEM) measurements were performed with a JEOL JEM-2200FS field emission energy filtering transmission electron microscope (FE-EFTEM) at an acceleration voltage of 200 kV. A bottom-mounted CMOS camera system (OneView; Gatan) was used for recording zero-loss filtered micrographs ($\Delta E \sim 0$ eV). Micrographs were processed with DM 3.3 image processing software (Gatan). Nanoparticle only samples were prepared by simple drop-casting a dilute dispersion onto carbon-coated copper grids. MDS powders were embedded in a polymer matrix and cut with a Leica Ultramicrotome UC7 + FC7.

Dynamic light scattering (DLS) and determination of ζ-potential were recorded on a Litesizer 500 (Anton-Paar).

Atomic force microscopy (AFM)

The surface topography was determined by atomic force microscopic measurements. The images were acquired with a Dimension Icon (Bruker Nano Inc.) in PeakForce tapping mode in air. A ScanAsyst Air cantilever (Bruker Nano Inc.) with a typical spring constant of 0.4 N m^{-1} and a resonant frequency of 70 kHz was used. The PeakForce amplitude was 60 nm, and the PeakForce frequency was 2 kHz. The AFM images were processed with NanoScope Analysis 1.80 (Bruker Nano Inc.). The topography was flattened by subtracting the first-order polynomial background using a threshold to exclude platelets from flattening. Platelet heights were determined using the "step tool" in NanoScope Analysis software. The samples were

prepared by slow evaporation of a few drops of a diluted suspension (0.02 g L^{-1}) on a Si wafer under ambient conditions.

ICP-AAS

To determine the elemental composition, to about 20 mg of the sample was added a mixture of 1.5 mL 30 wt% HCl (Merck), 0.5 mL of 85 wt% H_3PO_4 (Merck), 0.5 mL 65 wt% HNO_3 (Merck), and 1 mL of 48 wt% HBF_4 (Merck). The sample was digested in an MLS 1200 Mega microwave digestion apparatus for 6.5 min and heated at 600 W (MLS GmbH). The sample was allowed to cool to room temperature, and the clear solution was diluted to 100 mL and analyzed with a Varian Vista-Pro radial ICP-OES.

BET

Physisorption data was collected with a Quantachrome Autosorb-1 using N_2 at 77 K as the adsorbate. Prior, samples were degassed at 383 K for 24 h.

Small angle X-ray scattering (SAXS)

SAXS data were collected with a "Double Ganesha AIR" (SAXSLAB, Denmark). In this laboratory-based system, a micro-focused X-ray beam is provided by a rotating copper anode (MicoMax 007HF, Rigaku Corporation, Japan). A position-sensitive detector (PILATUS 300 K, Dectris) was used in different positions to cover the range of the scattering vector q = 0.004–0.6 $Å^{-1}$. Before the measurement, the clay suspensions were filled in 1 mm glass capillaries (Hilgenberg, code 4007610). The circularly averaged data were normalized to the incident beam, sample thickness, and measurement time.

Small angle X-ray scattering (SAXS) in magnetic field

A specially designed and in house built sample holder for 1 mm glass capillaries (Hilgenberg, code 4007610) was used for the measurements in magnetic field conditions. The capillary is placed between to strong permanent magnets in vertical direction having a fixed field strength of about 0.9 T. SAXS patterns were recorded with the SAXS system "Ganesha-Air" from (SAXSLAB, Xenocs). The X-ray source of this laboratory-based system was a D2-MetalJet (Excillum) with a liquid-metal anode operating at 70 kV and 3.57 mA with Ga-Kα radiation (λ = 0.1341 nm) providing a very brilliant and a very small beam (<100 μm). The beam was focused with a focal length of 55 cm using a specially made X-ray optic (Xenocs) to provide a very small and intense beam at the sample position. The transmitted intensity data were recorded by a position-sensitive detector (PILATUS 300 K, Dectris). To cover the range of scattering vectors between 0.026 and 3 nm^{-1}, different detector positions were used. The circularly averaged data were normalized to incident beam, sample thickness, and measurement time. Further details concerning the data reduction can be found in the supporting information.

Magnetization measurements

The samples were prepared by placing a Kapton foil on the Petri dish's bottom, casting dispersions of MDS on top and letting it dry. High aspect-ratio nanosheets self-assemble parallel to the Kapton surface during the water evaporation, yielding highly oriented films. Several discs of 4 mm diameter of each sample were punched out, stacked, and held together with Kapton tape. This stack with a sample mass of 3–10 mg was mounted on a quartz stick, allowing for alignment of the magnetic field within or perpendicular to the composite layers. The magnetization was measured as a function of the applied magnetic field at 300 K and 2 K on a PPMS9 (Quantum Design) using the VSM option. The AC magnetization was measured in temperature sweep mode with zero DC-field applied, an AC magnetic field of 10 Oe, and variable excitation frequencies ranging from 10 Hz to 10 kHz.

Author contributions

J. B., S. F., S. M., W. B., O. Kh, and D. W. conceived the project and designed the experiments. O. Kh and D. W. performed the synthesis and sample characterization. S. M. performed the magnetic measurements. S. R. and M. D. performed SAXS measurements, V. D. and S. R. assisted with the SAXS part of the manuscript. K. O. and G. P. performed AFM measurements. All authors read and contributed to the manuscript preparations.

Conflicts of interest

There are no conflicts to declare.

Acknowledgements

The authors thank F. Puchtler for producing the synthetic hectorite, M. Schwarzmann for the TEM images and ICP-OES analysis. We appreciate the support of the Keylab for Optical and Electron Microscopy of the Bavarian Polymer Institute (BPI). We thank R. Timmins for English proofreading. This work was supported by the Deutsche Forschungsgemeinschaft (SFB 840, projects A2, A6, B9 and C4).

Notes and references

1 M. A. C. Stuart, W. T. S. Huck, J. Genzer, M. Müller, C. Ober, M. Stamm, G. B. Sukhorukov, I. Szleifer, V. V. Tsukruk, M. Urban, F. Winnik, S. Zauscher, I. Luzinov and S. Minko, *Nat. Mater.*, 2010, **9**, 101–113.
2 H. Li, C. Li, W. Sun, Y. Wang, W. Hua, J. Liu, S. Zhang, Z. Chen, S. Wang, Z. Wu, Q. Zhu, R. Tang, J. Yu, L. He, G. A. Ozin and X. Zhang, *Adv. Mater.*, 2019, **31**, 1900388.
3 A. A. Sonin, *Liq. Cryst. Rev.*, 2018, **6**, 109–128.
4 S. Burylov, D. Petrov, V. Lacková, K. Zakutanská, N. Burylova, A. Voroshilov, V. Skosar, F. Agresti, P. Kopčanský and N. Tomašovičová, *J. Mol. Liq.*, 2021, **321**, 114467.
5 A. J. Hess, Q. Liu and I. I. Smalyukh, *Appl. Phys. Lett.*, 2015, **107**, 071906.

6 C. Cîrtoaje, E. Petrescu, C. Stan and D. Creangă, *Phys. E*, 2016, **79**, 38–43.
7 A. Mertelj and D. Lisjak, *Liq. Cryst. Rev.*, 2017, **5**, 1–33.
8 R. Sahoo, M. V. Rasna, D. Lisjak, A. Mertelj and S. Dhara, *Appl. Phys. Lett.*, 2015, **106**, 161905.
9 P. J. Ackerman and I. I. Smalyukh, *Nat. Mater.*, 2017, **16**, 426–432.
10 M. Mur, J. A. Sofi, I. Kvasić, A. Mertelj, D. Lisjak, V. Niranjan, I. Muševič and S. Dhara, *Opt. Express*, 2017, **25**, 1073–1083.
11 C. Scherer and A. M. Figueiredo Neto, *Braz. J. Phys.*, 2005, **35**, 718–727.
12 R. Ganguly, A. P. Gaind, S. Sen and I. K. Puri, *J. Magn. Magn. Mater.*, 2005, **289**, 331–334.
13 F. Brochard and P. G. de Gennes, *J. Phys.*, 1970, **31**, 691–708.
14 A. Mertelj, D. Lisjak, M. Drofenik and M. Čopič, *Nature*, 2013, **504**, 237–241.
15 P. Fabre, C. Casagrande, M. Veyssie, V. Cabuil and R. Massart, *Phys. Rev. Lett.*, 1990, **64**, 539–542.
16 N. Podoliak, O. Buchnev, O. Buluy, G. D'Alessandro, M. Kaczmarek, Y. Reznikov and T. J. Sluckin, *Soft Matter*, 2011, **7**, 4742–4749.
17 K. Binnemans, Y. G. Galyametdinov, R. Van Deun, D. W. Bruce, S. R. Collinson, A. P. Polishchuk, I. Bikchantaev, W. Haase, A. V. Prosvirin, L. Tinchurina, I. Litvinov, A. Gubajdullin, A. Rakhmatullin, K. Uytterhoeven and L. Van Meervelt, *J. Am. Chem. Soc.*, 2000, **122**, 4335–4344.
18 Y. Galyametdinov, M. A. Athanassopoulou, K. Griesar, O. Kharitonova, E. A. Soto Bustamante, L. Tinchurina, I. Ovchinnikov and W. Haase, *Chem. Mater.*, 1996, **8**, 922–926.
19 M. Wang, L. He, S. Zorba and Y. Yin, *Nano Lett.*, 2014, **14**, 3966–3971.
20 M. Hähsler, I. Appel and S. Behrens, *Phys. Sci. Rev.*, 2020, DOI: 10.1515/psr-2019-0090.
21 K. Koch, M. Kundt, A. Eremin, H. Nadasi and A. M. Schmidt, *Phys. Chem. Chem. Phys.*, 2020, **22**, 2087–2097.
22 Z. Li and Y. Yin, *Adv. Mater.*, 2019, **31**, 1807061.
23 L. Wang and T. Sasaki, *Chem. Rev.*, 2014, **114**, 9455–9486.
24 P. Davidson, C. Penisson, D. Constantin and J.-C. P. Gabriel, *Proc. Natl. Acad. Sci. U. S. A.*, 2018, **115**, 6662–6667.
25 J.-C. P. Gabriel, F. Camerel, B. J. Lemaire, H. Desvaux, P. Davidson and P. Batail, *Nature*, 2001, **413**, 504–508.
26 N. Miyamoto, H. Yamamoto, R. Kaito and K. Kuroda, *Chem. Commun.*, 2002, 2378–2379, DOI: 10.1039/b206998a.
27 R. Liu, T. Gong, K. Zhang and C. Lee, *Sci. Rep.*, 2017, **7**, 1–9.
28 M. Daab, N. J. Eichstaedt, A. Edenharter, S. Rosenfeldt and J. Breu, *RSC Adv.*, 2018, **8**, 28797–28803.
29 M. Daab, N. J. Eichstaedt, C. Habel, S. Rosenfeldt, H. Kalo, H. Schießling, S. Förster and J. Breu, *Langmuir*, 2018, **34**, 8215–8222.
30 S. Rosenfeldt, M. Stöter, M. Schlenk, T. Martin, R. Q. Albuquerque, S. Förster and J. Breu, *Langmuir*, 2016, **32**, 10582–10588.
31 M. Stöter, S. Gödrich, P. Feicht, S. Rosenfeldt, H. Thurn, J. W. Neubauer, M. Seuss, P. Lindner, H. Kalo, M. Möller, A. Fery, S. Förster, G. Papastavrou and J. Breu, *Angew. Chem.*, 2016, **128**, 7524–7528.
32 A. Lerf, *Dalton Trans.*, 2014, **43**, 10276–10291.
33 L. J. Michot, I. Bihannic, S. Maddi, S. S. Funari, C. Baravian, P. Levitz and P. Davidson, *Proc. Natl. Acad. Sci. U. S. A.*, 2006, **103**, 16101.
34 Y. Liu, Z. Xu, W. Gao, Z. Cheng and C. Gao, *Adv. Mater.*, 2017, **29**, 1606794.
35 M. Stöter, D. A. Kunz, M. Schmidt, D. Hirsemann, H. Kalo, B. Putz, J. Senker and J. Breu, *Langmuir*, 2013, **29**, 1280–1285.
36 Q. L. Zhu, C. F. Dai, D. Wagner, M. Daab, W. Hong, J. Breu, Q. Zheng and Z. L. Wu, *Adv. Mater.*, 2020, **32**, 2005567.
37 Z. L. Wu, M. Moshe, J. Greener, H. Therien-Aubin, Z. Nie, E. Sharon and E. Kumacheva, *Nat. Commun.*, 2013, **4**, 1–7.
38 K. Ament, D. R. Wagner, F. E. Meij, F. E. Wagner and J. Breu, *Z. Anorg. Allg. Chem.*, 2020, **646**, 1110–1115.
39 K. Ament, N. Köwitsch, D. Hou, T. Götsch, J. Kröhnert, C. J. Heard, A. Trunschke, T. Lunkenbein, M. Armbrüster and J. Breu, *Angew. Chem., Int. Ed.*, 2021, **60**, 5890–5897.
40 K. Ament, N. Köwitsch, D. Hou, T. Götsch, J. Kröhnert, C. J. Heard, A. Trunschke, T. Lunkenbein, M. Armbrüster and J. Breu, *Angew. Chem., Int. Ed.*, 2020, **60**, 5890–5897.
41 H. Zhang, C. Wang and G. Zhou, *Microsc. Microanal.*, 2020, **26**, 867–877.
42 M. Thommes, K. Kaneko, A. V. Neimark, J. P. Olivier, F. Rodriguez-Reinoso, J. Rouquerol and K. S. W. Sing, *Pure Appl. Chem.*, 2015, **87**, 1051–1069.
43 M. Thommes, *Chem. Ing. Tech.*, 2010, **82**, 1059–1073.
44 S. Singamaneni, V. N. Bliznyuk, C. Binek and E. Y. Tsymbal, *J. Mater. Chem.*, 2011, **21**, 16819–16845.
45 A. G. Roca, J. F. Marco, M. del Puerto Morales and C. J. Serna, *J. Phys. Chem. C*, 2007, **111**, 18577–18584.
46 M. P. Morales, S. Veintemillas-Verdaguer, M. I. Montero, C. J. Serna, A. Roig, L. Casas, B. Martínez and F. Sandiumenge, *Chem. Mater.*, 1999, **11**, 3058–3064.
47 M. B. Fernández van Raap, F. H. Sanchez, A. G. Leyva, M. L. Japas, E. Cabanillas and H. Troiani, *Phys. B*, 2007, **398**, 229–234.
48 L. A. Mercante, W. W. M. Melo, M. Granada, H. E. Troiani, W. A. A. Macedo, J. D. Ardison, M. G. F. Vaz and M. A. Novak, *J. Magn. Magn. Mater.*, 2012, **324**, 3029–3033.
49 B. D. Cullity and C. D. Graham, *Introduction to Magnetic Materials*, Wiley, Hoboken, NJ, USA, 2nd edn, 2008.
50 S. Mørup and E. Tronc, *Phys. Rev. Lett.*, 1994, **72**, 3278–3281.
51 M. Bałanda, *Acta Phys. Pol., A*, 2013, **124**, 964–976.

Electronic Supplementary Material (ESI) for Journal of Materials Chemistry C.

SUPPORTING INFORMATION

Title: Colloidally stable, magnetoresponsive liquid crystals based on clay nanosheets

Author(s): Olena Khoruzhenko, Daniel R. Wagner, Sebastian Mangelsen,* Martin Dulle, Sabine Rosenfeldt, Volodymyr Dudko, Katharina Ottermann, Georg Papastavrou, Stephan Förster, Wolfgang Bensch* and Josef Breu *

SAXS data for double stacks

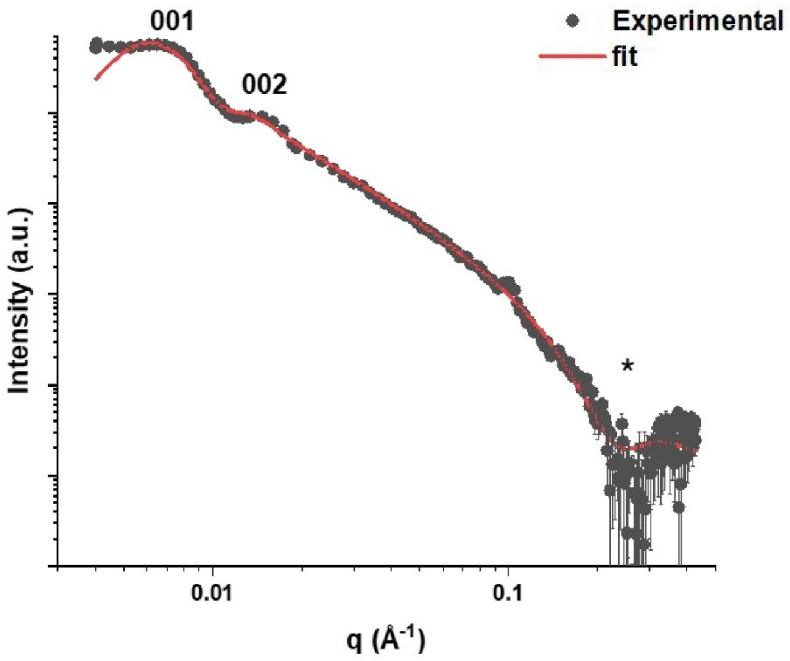

Figure S1. SAXS pattern of the nematic liquid crystal of double stacks at a concentration of 4wt%. The rational *00l* series indicates the spacing between the nanosheets to be 85 nm. * labels the structure factor minimum, indicating the characteristic thickness of the platelets to be 2.5 nm.

Maghemite nanoparticle characterization

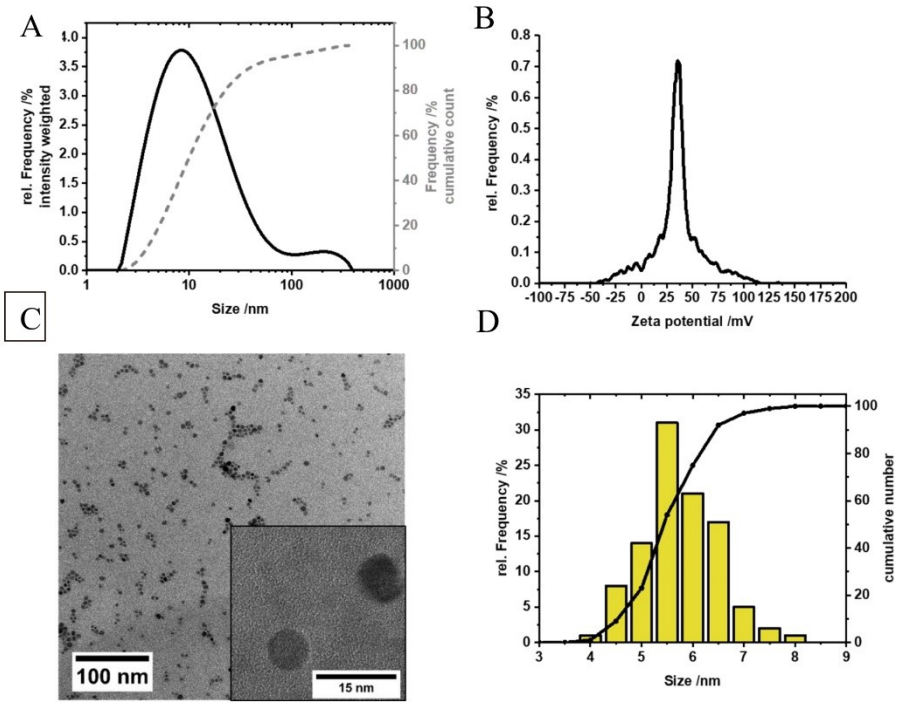

Figure S2. Characterization of nanoparticles. (A) hydrodynamic diameter according to DLS measurement. (B) zeta potential at pH 7 of y-Fe_2O_3 nanoparticles. (C) TEM image of y-Fe_2O_3 nanoparticles. (D) histogram of the core sizes of 100 particles.

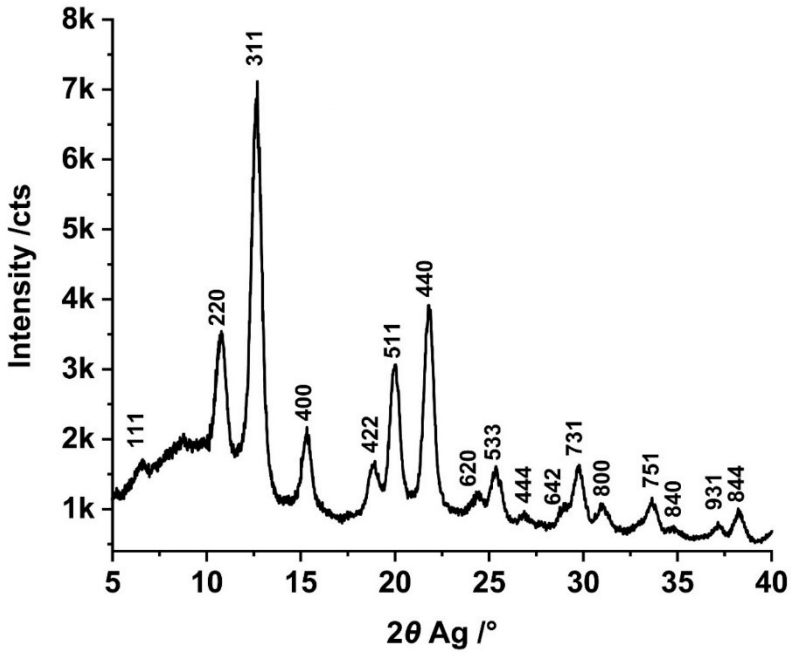

XRD pattern of γ-Fe_2O_3

Figure S3. Wide angle PXRD using Ag-K_α (λ = 0.5594075 Å) radiation of γ-Fe_2O_3 nanoparticles

Mößbauer spectroscopy of γ-Fe_2O_3

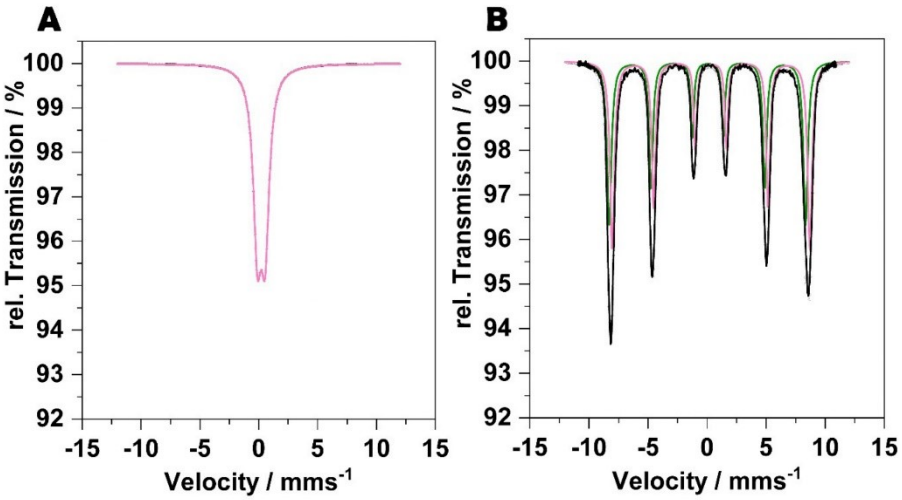

Figure S4. (A) Room temperature Mößbauer spectrum showing only one quadrupole doublet. (B) 4.2 K Mößbauer spectrum with two sextets for Fe^{3+} in tetrahedral sites (green) and octahedral sites (pink).

To additionally confirm the formation of the γ-Fe_2O_3 we performed the Mößbauer spectroscopy, because the standard XRD peaks of γ-Fe_2O_3 and Fe_3O_4 are almost identical. The RT spectrum showed only one quadrupole doublet due to fast superparamagnetic relaxation processes that is characteristic for small sized iron oxide nanoparticles (Figure S4 A). The spectrum recorded at 4.2 K showed two sextets with nearly identical hyperfine fields and nearly no quadrupole interaction (Figure S4 B). The isomeric shifts of 0.05 mm·s^{-1} and 0.33 mm·s^{-1} corresponded to the tetrahedral and octahedral sites of Fe^{3+}, respectively. Fe^{2+} that would indicate a magnetite phase could not be observed.[1, 2]

5

XRD pattern of NH_4^+/Na^+ ordered heterostructures also named ordered interstratification (OI)

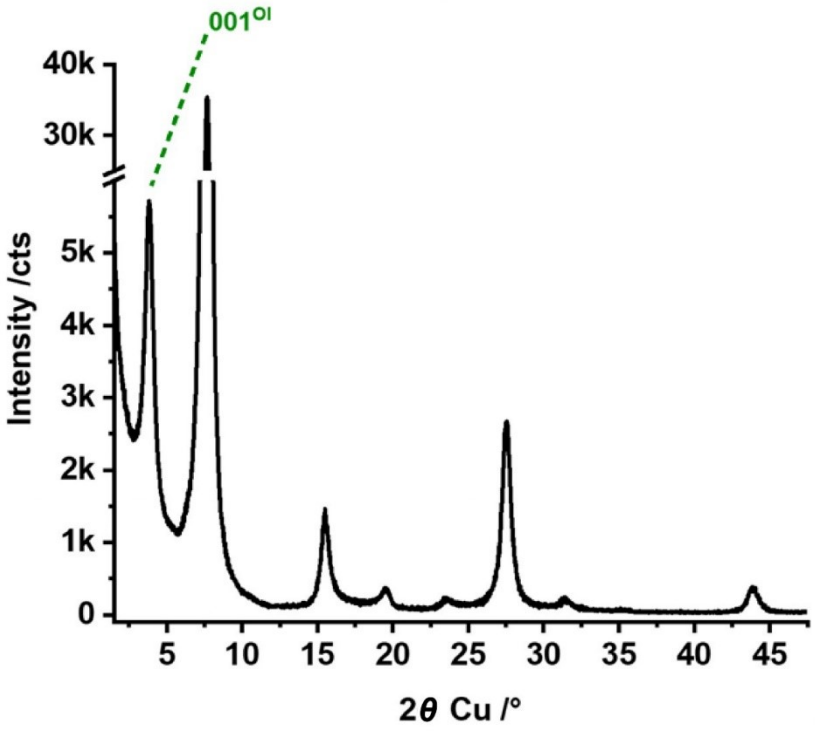

Figure S5. Wide angle PXRD of the ordered interstratification (OI) of strictly alternating Na^+ and NH_4^+ layers in synthetic hectorite. The sample was equilibrated in an atmosphere with 43% relative humidity.

AFM of double stacks

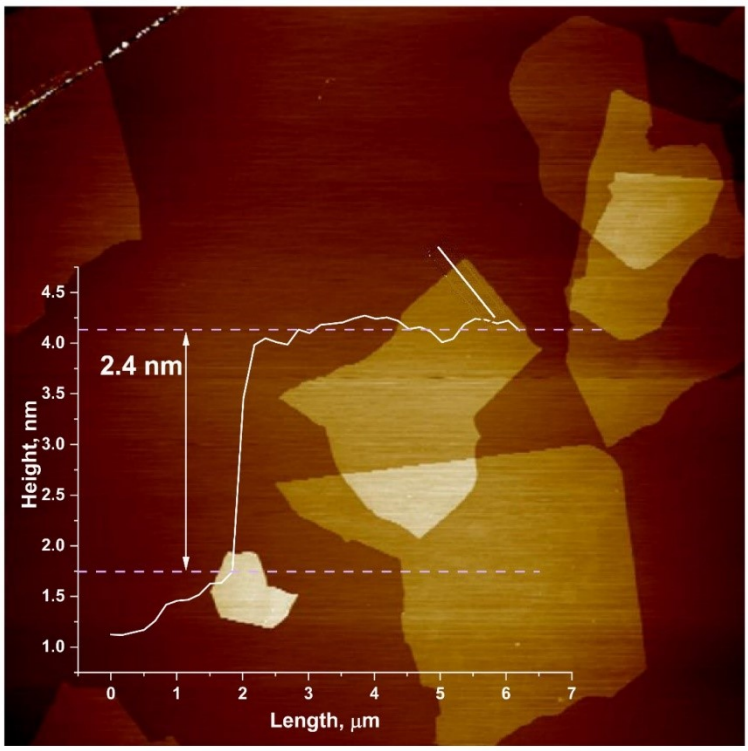

Figure S6. Representative, topographical AFM image of double stacks. A height profile shows a platelet thickness of 2.4 nm.

ICP-OES

Table S1. Elemental composition according to ICP-OES.

Element	**Weight fraction of the element [%]**		
Nominal Fe_2O_3	*16 wt%*	*30 wt%*	*45 wt%*
Fe	11.9	21.5	31.8
Mg	13.4	11.2	8.8
Fe_2O_3 wt%[a]	17	31	46
Nominal Formula[b]	$(Fe_2O_3)_{0.46}Li_{0.31}$ $(Mg_{2.5}Li_{0.5}Si_4O_{10}F_2)$	$(Fe_2O_3)_{1.05}Li_{0.31}$ $(Mg_{2.5}Li_{0.5}Si_4O_{10}F_2)$	$(Fe_2O_3)_{1.95}Li_{0.31}$ $(Mg_{2.5}Li_{0.5}Si_4O_{10}F_2)$

[a] Assuming an stoichiometric composition of Fe_2O_3 the weight fraction of maghemite nanoparticles is calculated from the Fe wt%.

[b] Then the nominal formula was calculated to be $(Fe_2O_3)xLi_{0.31}(Mg_{2.5}Li_{0.5}Si_4O_{10}F_2)$. Si was not detected directly via ICP-OES. The amount of Si was rather calculated assuming the atomic ratio of Mg to Si of 2.5:4 as required by the hectorite-composition.

Top-view TEM MDS 16.6

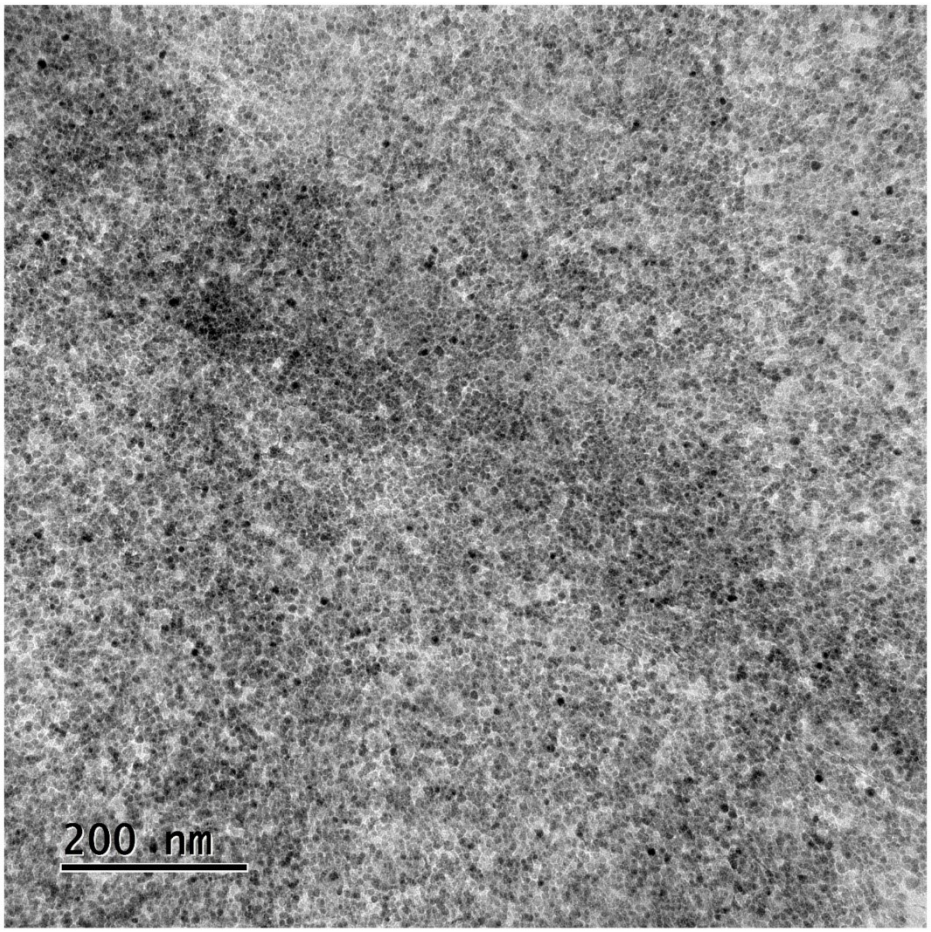

Figure S7. TEM image of top view of the MDS 16.6.

BET

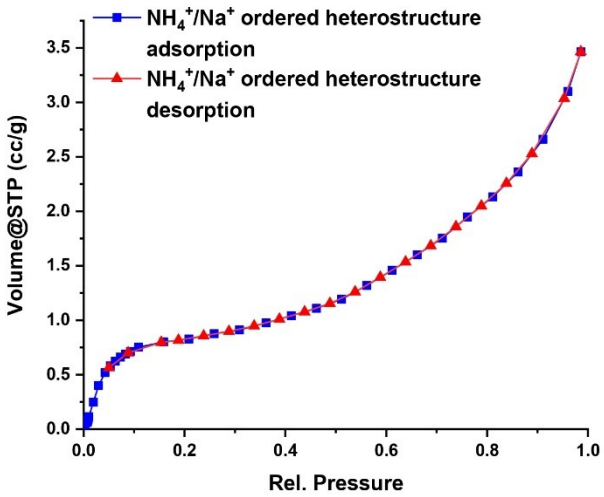

Figure S8. Nitrogen adsorption-desorption isotherms of the NH_4^+/Na^+ ordered heterostructures.

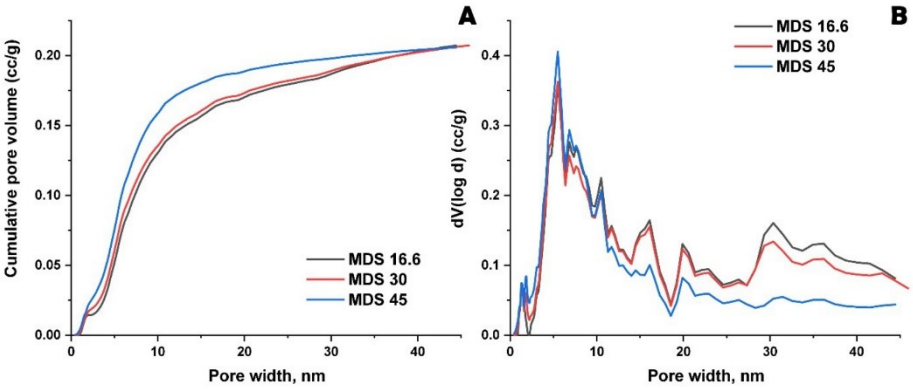

Figure S9. Pore width analysis of nitrogen physisorption isotherms taken at 77 K derived by applying the DFT kernel for MDS 16.6, MDS 30, MDS 45. (A) Cumulative pore volumes (B) Pore size distributions.

Grayscale analysis of a TEM micrograph taken for a cross section of restacked

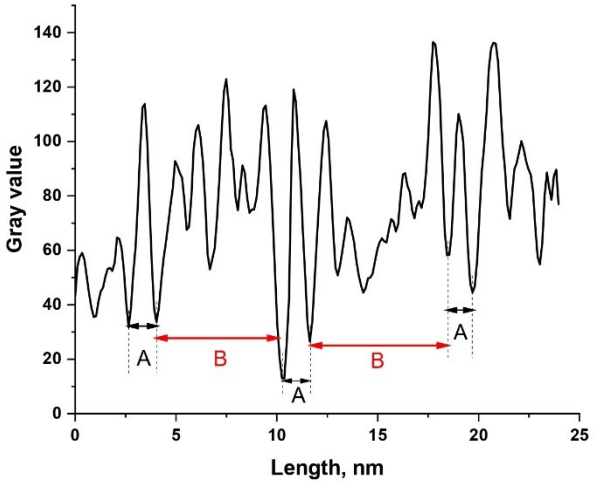

MDS

Figure S10. Grayscale analysis of a TEM micrograph taken for a cross section of restacked MDS showing the periodic arrangement of the material with characteristic lengths A = 1.3 nm corresponding to the distance between the centres of two silicate nanosheets and B = 6.54 nm corresponding to the diameter of nanoparticles sandwiched between two nanosheets.

Orientation order analysis

The orientation order parameter was calculated using the following formula based on the description from Lovell and Mitchel by averaging over the second Legendre polynomial.[3]

$$S = -2 \cdot \frac{\int_0^{\frac{\pi}{2}} I(\phi) \cdot 1/2 \cdot (3\cos^2\phi - 1) \cdot \sin\phi d\phi}{\int_0^{\frac{\pi}{2}} I(\phi) \cdot \sin\phi d\phi}$$

S is the order parameter, ϕ is the azimuthal angle (*y* axis corresponds to $\phi = 0$) $I(\phi)$ is the intensity at ϕ. In order to minimize smearing effects from the collimation of the SAXS instrument the $I(\phi)$ was averaged in the range of 0.03nm^{-1}< q <0.14nm^{-1}. The order parameter has a value of S=0.7 which is very well ordered with respect to the director given by the magnetic field.

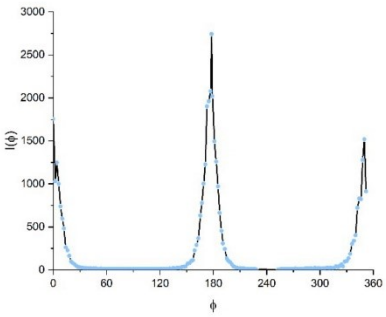

Figure S11. The $I(\phi)$ plot of the magnetically oriented sample used to calculate the order parameter.

Data reduction for SAXS of the oriented sample and fit with 2D structure factor

The sample was filled in a 1 mm Hilgenberg glass capillary and inserted in a homemade sample holder consisting of two fixed permanent magnets, left and right of the vertically orientated capillary. The field strength on the sample position is ~0.9 T. For the measurements without field another sample holder was used. For both a separate water background was measured as well.

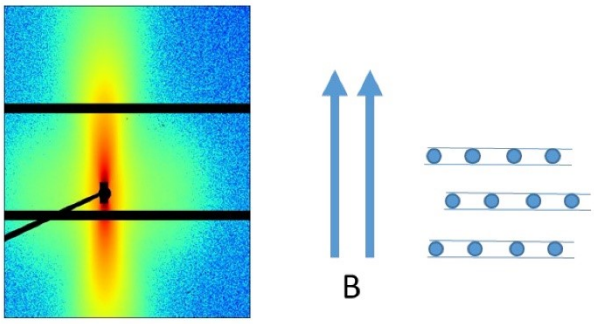

Figure S12. Left: 2D SAXS pattern in magnetic field, middle: direction of the magnetic field, right: direction of the stacks.

Data reduction for SAXS of the oriented sample and fit with 2D structure factor

In order to be able to properly account for the anisotropy in the samples scattering the back ground was subtracted in 2D and subsequently the radial average was either along the nematic director or perpendicular to it. To do that we chose the width of the peaks in the $I(\phi)$ plots to define the regions of interest. The radial averaged data from the three detector distances was scaled to measurement time, transmission as well sample thickness and put on absolute scale. For the highly oriented sample we got two scattering curves.

This enables us to separate the scattering of the sheets from the particle scattering. As the particles are isotropic they scatter to all angles even when the much stronger scattering sheets

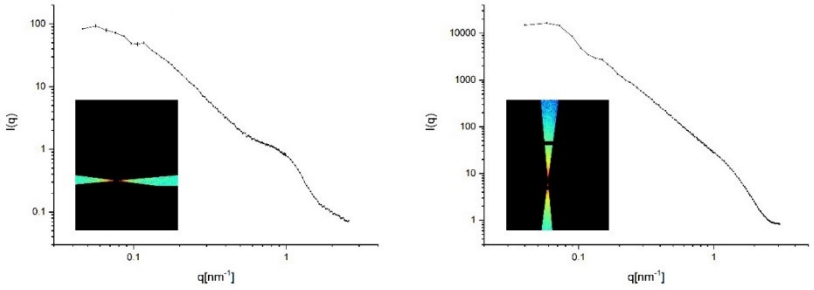

are oriented due to the magnetic field.

Figure S13. Left: radial averaged scattering along the nematic director with particle scattering visible next to a contribution at low q from sheets which are not perfectly oriented. Right: radial averaged scattering perpendicular the nematic director where the contribution from the sheets is a hundred times higher than on the left side.

Data reduction for SAXS of the oriented sample and fit with 2D structure factor

In order to separate the excess particle scattering from the sheets we used the I(q) scaling at medium 0.3>q<0.4 to shift both curves on top of each other.

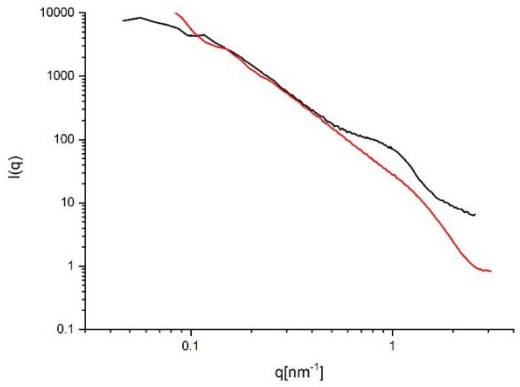

Figure S14. Shifted radial average along the nematic director so that the intermediate q values overlap.

By subtracting the red from the black curve the excess particle scattering within the sheets is extracted. This is possible because at high q the red curve is dominated by the sheet form factor and the nice $I(q)\sim q^{-2}$ scaling at intermediate q values for both curves. The resulting scattering curve represents the scattering from the particles within the double stacks only.

We also were able to fit this data with a model for polydisperse spheres also taking into account the 2D Percus Yevick structure factor for hard spheres.[4] The fit results in a particle radius of 2.5nm±0.5nm and a 2D packing fraction of 0.4. The particle radius fits very good with the TEM and DLS results as far as the packing fraction within the layer goes it is an average value over the whole sample and seems reasonably high.

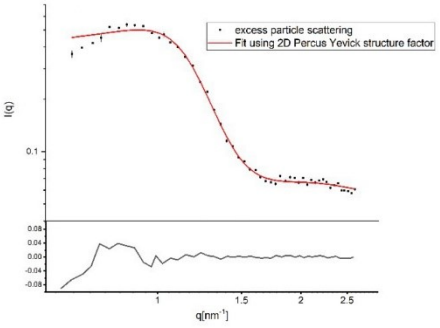

Figure S15. Excess particle scattering with the fit using a polydisperse sphere model with 2D PY structure factor.

Photographs of nematic texturing

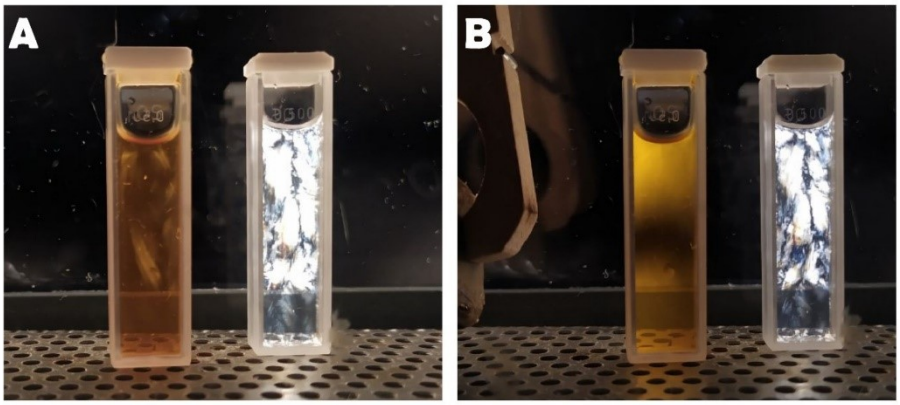

Figure S15. Photographs of nematic phases of DS (right cuvette) and MDS (left cuvette) without (A) and with (B) applied magnetic field in cross-polarized light.

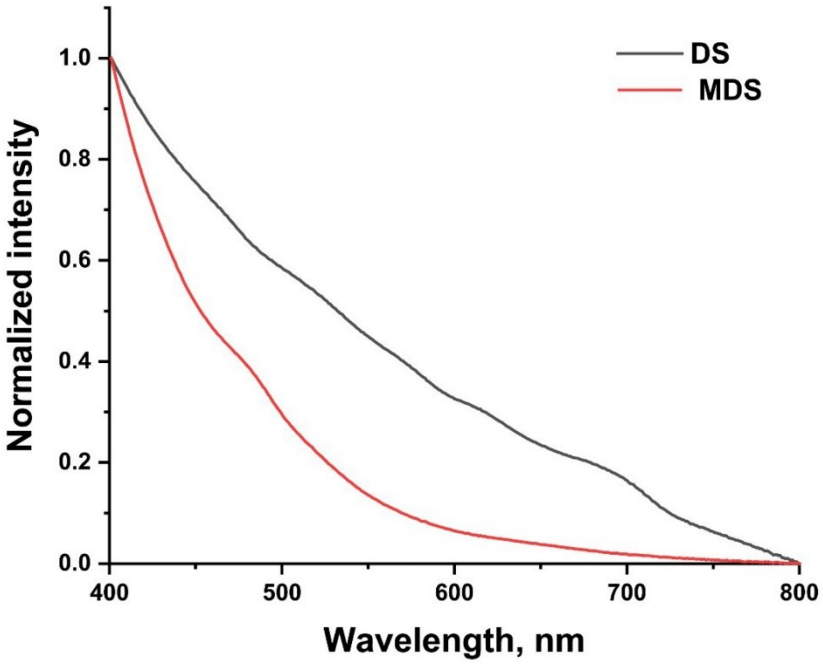

Figure S16. UV-vis spectra of nematic phases DS (black, 0.3 wt%) and MDS (red, 0.15 wt%).

References

1. K. Ament, D. R. Wagner, F. E. Meij, F. E. Wagner and J. Breu, *Z. Anorg. Allg. Chem.*, 2020, **646**, 1110–1115.
2. F. J. Berry, S. Skinner and M. F. Thomas, *J. Phys.: Condens. Matter*, 1998, **10**, 215–220.
3. R. Lovell and G. R. Mitchell, *Acta Cryst. A*, 1981, **37**, 135–137.
4. Y. Rosenfeld, *Phys. Rev. A*, 1990, **42**, 5978–5989.

MAGNETO-ORIENTATION OF MAGNETIC DOUBLE STACKS FOR PATTERNED ANISOTROPIC HYDROGELS WITH MULTIPLE RESPONSES AND MODULABLE MOTIONS

Chen Fei Dai,[a] Olena Khoruzhenko,[b] Chengqian Zhang,[d] Qing Li Zhu,[a] Dejin Jiao,[a] Prof. Miao Du,[a] Prof. Josef Breu,[b]* Prof. Peng Zhao,[c]* Prof. Qiang Zheng,[a]* Prof. Zi Liang Wu[a]*

* Corresponding authors

[a] Ministry of Education Key Laboratory of Macromolecular Synthesis and Functionalization Department of Polymer Science and Engineering, Zhejiang University, Hangzhou, 310027 China

[b] Department of Chemistry and Bavarian Polymer Institute, University of Bayreuth, Universitätsstr. 30, 95440 Bayreuth, Germany

[c] The State Key Laboratory of Fluid Power Transmission and Control Systems, Key Laboratory of 3D Printing Process and Equipment of Zhejiang Province, School of Mechanical Engineering, Zhejiang University, Hangzhou, 310028 China

[d] The State Key Laboratory of Fluid Power Transmission and Control Systems, Key Laboratory of 3D Printing Process and Equipment of Zhejiang Province, School of Mechanical Engineering, Zhejiang University, Hangzhou, 310028 China

Published in Angew. Chem. Int. Ed. 61, 35 (2022).

GDCh Research Articles Angewandte International Edition Chemie www.angewandte.org

Two-Dimensional Materials | Very Important Paper

How to cite: *Angew. Chem. Int. Ed.* **2022**, *61*, e202207272
International Edition: doi.org/10.1002/anie.202207272
German Edition: doi.org/10.1002/ange.202207272

Magneto-Orientation of Magnetic Double Stacks for Patterned Anisotropic Hydrogels with Multiple Responses and Modulable Motions

Chen Fei Dai, Olena Khoruzhenko, Chengqian Zhang, Qing Li Zhu, Dejin Jiao, Miao Du, Josef Breu, Peng Zhao,* Qiang Zheng,* and Zi Liang Wu**

Abstract: Reported here is a multi-response anisotropic poly(*N*-isopropylacrylamide) hydrogel developed by using a rotating magnetic field to align magnetic double stacks (MDSs) that are fixed by polymerization. The magneto-orientation of MDSs originates from the unique structure with γ-Fe_2O_3 nanoparticles sandwiched by two silicate nanosheets. The resultant gels not only exhibit anisotropic optical and mechanical properties but also show anisotropic responses to temperature and light. Gels with complex ordered structures of MDSs are further devised by multi-step magnetic orientation and photolithographic polymerization. These gels show varied birefringence patterns with potentials as information materials, and can deform into specific configurations upon stimulations. Multi-gait motions are further realized in the patterned gel through dynamic deformation under spatiotemporal light and friction regulation by imposed magnetic force. The magneto-orientation assisted fabrication of hydrogels with anisotropic structures and additional functions should bring opportunities for gel materials in biomedical devices, soft actuators/robots, etc.

Introduction

Concepts that draw inspirations from biological tissues have enabled substantial progress in creating artificial intelligent materials.[1] Hydrogels, a class of soft materials with water as the major component, have close similarity to living tissues and therefore receive particular research interest.[2] Although great efforts have been made to improve the mechanical properties to match specific soft tissues,[3] synthetic hydrogels usually have an isotropic network, different from the anisotropic structures of biological tissues such as muscles and ligaments.[4,5] Creating ordered structures in hydrogel materials should afford them with anisotropic optical, mechanical, and response properties, thereby promoting their applications in biomedical and engineering fields.

In recent years, various anisotropic materials have been developed by forming ordered structures of polymer chains or inorganic fillers in the soft matrices.[5,6] One straightforward strategy is to orient polymer chains by stretching the materials and then fixing this anisotropic structure;[7] but this method requires the material capable of withstanding considerable deformation and force, and can only produce materials with monodomain anisotropic structures. Another strategy is to align rigid molecules or anisotropic fillers under external fields and then freeze the ordered structures by curing of the precursors.[8–14] For example, Tovar and co-workers used shear forces to align π-conjugated peptide nanostructures in hydrogels that showed directionally dependent optical signal and electrical response.[8a] Anisotropic hydrogels can also be obtained by electric field-induced orientation of anisotropic particles with the permanent or induced dipole moment.[9] However, the direct contact with precursor solutions may result in unexpected electrochemical reactions and/or electrophoresis during gel synthesis. Different from the aforementioned strategies, magnetic fields can be applied in non-contact mode to orient various mesogens and inorganic fillers in order to fabricate anisotropic materials.[10–14] For instance, Stupp et al. developed anisotropic hydrogels with the assistance of a static magnetic field to orient nickel nanowires that were embedded in a photoresponsive polymer matrix; the resultant hydrogels

[*] C. F. Dai, Q. L. Zhu, D. Jiao, Prof. M. Du, Prof. Q. Zheng, Prof. Z. L. Wu
Ministry of Education Key Laboratory of Macromolecular Synthesis and Functionalization Department of Polymer Science and Engineering, Zhejiang University
Hangzhou 310027 (China)
E-mail: zhengqiang@zju.edu.cn
wuziliang@zju.edu.cn

Prof. J. Breu
Bavarian Polymer Institute and Department of Chemistry, University of Bayreuth
Universitätsstrasse 30, 95440 Bayreuth (Germany)
E-mail: Josef.Breu@uni-bayreuth.de

O. Khoruzhenko, C. Zhang, Prof. P. Zhao
The State Key Laboratory of Fluid Power Transmission and Control Systems, Key Laboratory of 3D Printing Process and Equipment of Zhejiang Province, School of Mechanical Engineering, Zhejiang University
Hangzhou 310028 (China)
E-mail: pengzhao@zju.edu.cn

were used as continuum soft robots and showed multi-gait motions steered by light and magnetic field.[11] However, it is still a grand challenge to develop patterned hydrogels with sophisticated anisotropic structures.

Besides nanoparticles and nanowires, two-dimensional (2D) nanosheets can also be oriented by magnetic fields to form lamella-like ordered structures that will further enhance the anisotropic properties and responses of the resultant hydrogels.[12–14] For example, Studart et al. decorated Al_2O_3 platelets with Fe_3O_4 nanoparticles and then aligned them by a rotating magnetic field to develop anisotropic poly(*N*-isopropylacrylamide) (PNIPAm) hydrogels. Bilayer hydrogel was further prepared by multi-step magnetic orientation and polymerization to form sophisticated anisotropic structures of the platelets, which showed programmed deformations under external stimuli.[13a] Another seminal work by Aida et al. reported on the development of muscle-like anisotropic hydrogels applied an ultrastrong ($\approx$10 T) superconducting magnetic field to perfectly align titanate nanosheets.[14] The obtained nanocomposite PNIPAm hydrogel exhibited fast and isochoric deformations upon heating due to the reversibly changes of electrostatic permittivity and the resulting anisotropic electrostatic repulsion. They further used this hydrogel to realize earthworm-like peristaltic crawling in a confined glass tube upon periodic light irradiation after incorporating gold nanoparticles.[14b] However, it is still challenging to develop complex ordered structures in the hydrogel by using such a superconducting magnetic field. In addition, the nanosheets and photothermal nanoparticles are separately introduced into the hydrogel to afford photo-induced anisotropic response. The possible diffusion of the nanoparticles out of the matrix may lead to reduced performances of the gel. On the other hand, the locomotion of anisotropic gels usually relies on specific strategies to convert cyclic bending/unbending or stretching/contraction deformations into directional motions by using a rachet plate or creating asymmetric shape of the material.[14d,15] Programmable locomotion with switchable direction and gait mode has been rarely realized in anisotropic gels, which require sophisticated controls of the distributed structures and cooperative actuations for dynamic morphing.[1c] Clearly, it is highly desirable to develop hydrogels with sophisticated anisotropic structures and multiple responses by applying a weak magnetic field to align the functional nanosheets, which can be coupled with other advanced fabrication technologies.

Here we report a series of anisotropic PNIPAm hydrogels fabricated by applying a weak rotating magnetic field ($\approx$260 mT) to orient 2D magnetic double stacks (MDSs) followed by polymerization to fix the ordered structures. The MDSs have a unique structure with γ-Fe_2O_3 nanoparticles being sandwiched by two silicate layers, which can be dispersed in water with high stability.[15a] The aqueous suspensions show ferronematic phases at a very low content, which are responsive to magnetic field and light. The obtained monodomain PNIPAm hydrogels have anisotropic optical and mechanical properties due to the highly-ordered arrangement of the MDSs. The hydrogels also exhibit anisotropic response upon heating or light irradiation. Hydrogels with sophisticated ordered structures of MDSs are further developed by multi-step magnetic orientation and photolithographic polymerization, which show complex birefringent patterns and deform into three-dimensional (3D) configurations. Versatile locomotion is realized in the patterned hydrogel by dynamic actuations under spatiotemporal light and magnetic field. The strategy of preparing anisotropic hydrogels and the light- and magnet-steered locomotion should be informative for the design of functional materials and soft actuators with versatile applications.

Results and Discussion

The magnetic double stacks (MDSs) were synthesized according to a previously published procedure.[16] The generic structure of MDSs is shown in Figure 1a. MDSs have a sandwich-like structure with two nanosheets of $[Li_{0.25}][Mg_{2.5}Li_{0.5}][Si_4]O_{10}F_2$ encompassing γ-Fe_2O_3 nanoparticles confined in the resulting interlayer space. The singular silicate nanosheet (thickness 1 nm) has a high aspect ratio ($\approx$20000) and high density of negative charges (1.1 nm^{-2}), while the surface of magnetic nanoparticles bears positive charges.[17] As shown in Figure S1 by atomic force microscopy (AFM), the typical diameter of MDS is $\approx$15 μm. As γ-Fe_2O_3 nanoparticles are 5.5 ± 1.1 nm with a low polydispersity and the two individual hectorite sheets are 2×1 nm,[16] the height observed by AFM of $\approx$8.5 nm is in good agreement with expectations, in particular as in addition the countercations attached to the upper surface need to be taken into accounts. These structural attributes afford MDSs with structural stability and good dispersibility in water. The aqueous suspension of MDSs forms a ferronematic phase even at a very low content ($\approx$0.3 wt%) as rotation is hampered even at separations >50 nm of individual MDSs.[16a] The suspension with 1 wt% of MDS exhibits strong birefringence when placed between a pair of crossed polarizing films (Figure S2). This ferronematic phase can be further oriented by mechanical shearing (Figure S3). The relationship between the orientation direction and the birefringence color provides a straightforward way to characterize the alignment of MDSs.[18] The multi-domain nematic suspension can also be transformed into a monodomain under a magnetic field, due to the presence of magnetic γ-Fe_2O_3 nanoparticles (Figure S4). The sandwiching of nanoparticles affords collective magnetic response and provides MDSs with obvious superparamagnetism at ambient temperature and thus a suspension with ultrafast response to magnetic field (Figure 1b,c and Figure S5).

Anisotropic hydrogels are prepared by using a weak magnetic field (260 mT) to orient MDSs and then fixing the ordered structure by photopolymerization to form a gel matrix. The introduction of neutral monomer, chemical crosslinker, and photo-initiator does not influence the ferronematic phase of the suspension and the magnetic orientation of MDSs. Static or rotating magnetic fields are then applied to prepare anisotropic hydrogels, which are compared with that synthesized in the absence of magnetic

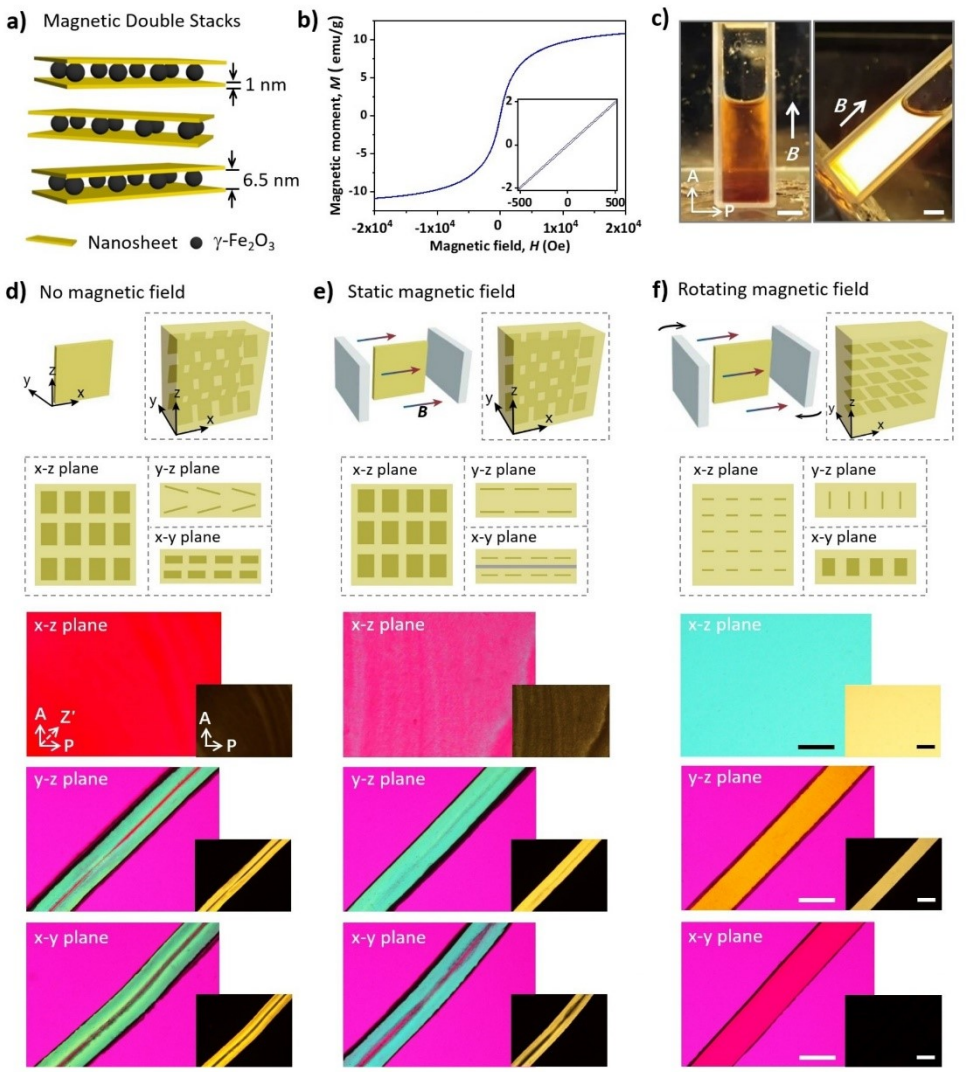

Figure 1. a) Schematic of the sandwich-like structure of MDSs. b) Magnetic hysteresis loop of MDS powder. c) Photos of a ferronematic suspension of MDS (1 wt%) between a pair of crossed polarized films. A magnet is placed under the cuvette filled with the MDS suspension. Scale bar: 5 mm. d–f) Schematic for the gel synthesis and the alignments of MDSs (top) and POM images of the hydrogel sheets observed from different directions (bottom). The hydrogels were prepared without magnetic field (d), with static magnetic field (e), or with rotating magnetic field (f). A: analyzer, P: polarizer, Z': slow axis of 530 nm tint plate. Scale bar: 1 mm.

field (Figure 1d–f). When prepared without magnetic field, the nanocomposite hydrogel sheet (corresponding to *x*–*z* plane) shows no birefringence when viewed from the top (*y* direction, as noted in the schematic figure) under a polarizing optical microscope (POM). However, the cross-sections of the hydrogel show strong birefringence except the middle region, indicating the formation of anisotropic structure during the gel synthesis (Figure 1d). This unexpected structure arises from the shear-induced orientation of MDSs when the precursor solution is injected into the reaction cell; the gradual rising of the fluid results in shear-orientation of MDSs that are fixed by subsequent polymerization (Fig-

ure S6). Due to this reason, the cross-sections (x–y plane and y–z plane) of the hydrogel exhibit similar birefringent pattern. A careful analysis indicates that the MDSs in the cross-section (y–z plane) are aligned at the regions close to the glass substrate, as expected for shear orientation with an oblique angle of $\pm 15°$ to the surface.

When a static magnetic field is applied, the anisotropic structure of the hydrogel is only slightly improved, as revealed by POM observations. Under static magnetic field, the MDSs previously tilted to the glass substrate are oriented along the magnetic field. No birefringence is found in the x–z plane of the hydrogel film, yet uniform birefringence is observed in the y–z and x–y planes (Figure 1e and Figure S7). This is because a static magnetic field only results in uniaxial orientation of MDSs along the magnetic field and lacks control over other directions. When a rotating magnetic field is applied, the hydrogel has, however, a much better anisotropic structure of MDSs (Figure 1f and Figure S8). The MDSs tend to follow the direction of magnetic field to minimize their magnetic energy and rotate synchronously with the rotating magnetic field. Therefore, the nanosheets align in the rotating plane of the magnetic field, i.e. parallel to the x–y plane of the sample.[13b,19] In other words, biaxial orientation of MDSs in the suspension is achieved under the rotating magnetic field, which can be immobilized further by photopolymerization. This strategy results in a monodomain hydrogel with MDSs perfectly aligned along the planar rotating magnetic field. The anisotropic structure of hydrogel is confirmed by POM observations.

We further examine the influences of rotating frequency, action time, and strength of the rotating magnetic field on the degree of anisotropy of resultant hydrogels. As shown in Figure S9a, the hydrogels show almost identical birefringence, indicating that the rotating frequency ranging from 10 to 60 Hz has little influence on the alignment of MDSs.[13b,19] The action time of the rotating magnetic field also shows little influence on the alignment of MDSs (Figure S9b). When the action time increases from 20 s to 10 min, the hydrogels show the same birefringence, indicating a high efficiency of rotating magnetic field to align the MDSs. As the magnetic field strength determines the magnetic torque, it is expected to be important for the magnetic orientation. As the magnetic field strength increases from 40 to 260 mT, the intensity of birefringence indeed increases, indicating an improved orientation degree of MDSs (Figure S9c). Therefore, the rotating frequency, action time, and strength of the rotating magnetic field are set as 30 Hz, 20 s and 260 mT respectively, for the synthesis of anisotropic gels.

The alignment of MDSs endows the hydrogel with anisotropic optical and mechanical properties.[12a,19] Strong anisotropic SAXS patterns are observed in the x–z and y–z planes of the as-prepared gel, whereas an isotropic pattern is found in the x–y plane (Figure 2a–c), which further confirms the alignments of MDSs in the gel. The calculated orientation degree of MDSs in the as-prepared gel is 0.88, which slightly decreases to 0.86 after being equilibrated in water due to the weak volume expansion of the gel (Figure S10). The swelling ratio in length of the hydrogel is also anisotropic, i.e. 1.2 and 1.3 in the direction parallel (//) and perpendicular ($\perp$) to the alignment of MDSs (Figure 2d and Figure S11). This hydrogel also shows anisotropic mechanical properties. As shown in Figure 2e and 2f, the Young's modulus of the gel stretched along the // direction is ≈ 3 times that along the $\perp$ direction, while the breaking strain along the // direction is $\approx 40\,\%$ lower than that along the $\perp$ direction. This anisotropic mechanical property arises from the highly-ordered reinforcing MDSs. Rigid MDSs as the stiff crosslinking junctions restrict the in-plane deformation of the gel matrix, thereby resulting in larger modulus and strength of the hydrogel along the // direction.[9b,20] An isotropic hydrogel containing randomly dispersed MDSs is prepared (Figure S12, see experiment details in Supporting Information) for comparison of the mechanical properties with those of the anisotropic gel. It is rational that the modulus of the MDS-containing isotropic gel is between the moduli of the anisotropic gel in the // direction and $\perp$ direction (Figure 2e).[14a]

The nanocomposite PNIPAm hydrogel also exhibits anisotropic response to stimulus (Figure 3). After being incubated in hot water (40 °C), the gel rapidly becomes opaque, expanding to 1.1 times the original length in the $\perp$ direction and contracting to 0.85 in the // direction within 5 s (Figure 3a–c). The abnormal slight expansion in the $\perp$ direction is ascribed to the increase in electrostatic permittivity of the media with more free water molecules arising from the rapid dehydration of PNIPAm above the lower critical solution temperature (LCST). After long-term storage at 40 °C, the hydrogel gradually contracts its volume by shrinking the length by a factor of 0.63 and 0.56 in $\perp$ and // direction, respectively. The long-term behavior of the gel is similar to the common PNIPAm hydrogel, which contracts at high temperature by migration of water molecules out of the gel matrix.[9a–c] For the anisotropic hydrogel in this work, volume contraction of the gel completes after ≈ 1 h.

The interlayer γ-Fe_2O_3 in MDSs endows the nanocomposite hydrogel with a wide absorption peak in the region of 400–600 nm (Figure S13) and thus high photothermal efficiency.[21] Thereby, the hydrogel can be locally heated by irradiation under a green laser (520 nm). The rising speed and amplitude of the local temperature depend on the intensity and irradiation time of the green laser (Figure 3d). With higher intensity, the temperature increases rapidly until it reaches the saturation temperature. For example, the local temperature of the gel dramatically rises from 23 to 44 °C within 4 s under the laser irradiation with the intensity of 2.34 $W\,cm^{-2}$. Cyclic laser irradiation results in dynamic modulation of the temperature, which increases when the laser is on and decreases when it is off (Figure 3e). The variations of the gel's dimensions under laser irradiation are similar to that upon heating (Figure S14). The photothermal effect of γ-Fe_2O_3 nanoparticles allows thus for a repeated modulation of the gel by laser irradiation. Therefore, the anisotropic hydrogel has multiple responses to magnetic field, temperature, and light, providing versatility in realizing programmed morphing and motion of the gel. Another advantage of the hydrogel is its superparamagnet-

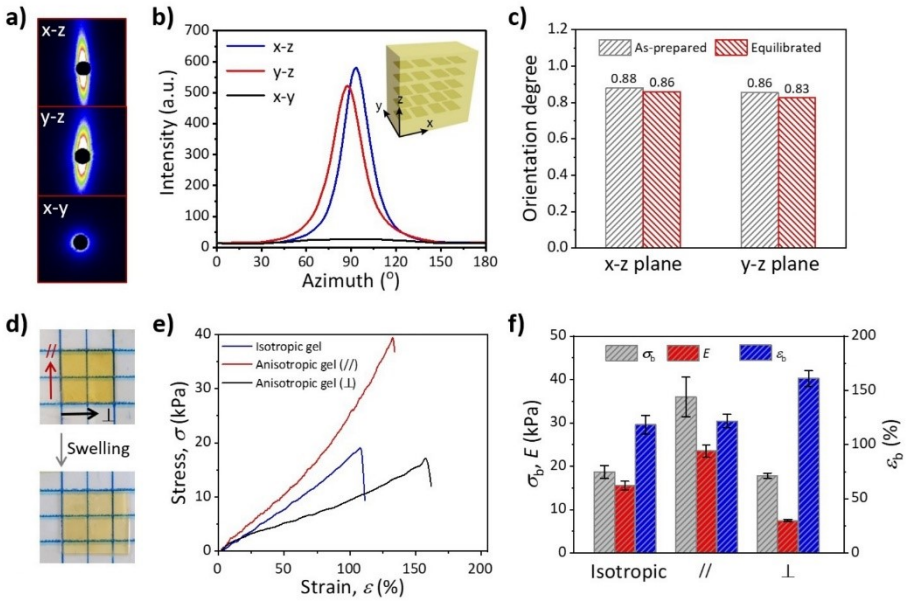

Figure 2. a–c) 2D SAXS patterns (a), scattering intensity–azimuth plots (b), and orientation degree of MDS (c) of the as-prepared hydrogel. Orientation degree of MDS in the equilibrated gel is also presented in (c). d) Photos of the anisotropic hydrogel before and after the swelling process. e) Tensile stress–strain curves of the isotropic gel and anisotropic gel stretched from // and ⊥ directions. f) Corresponding mechanical parameters of the gels, including Young's modulus E, breaking stress σ_b, and breaking strain ε_b. Error bars represent the standard deviation of the mean ($n=3$).

ism at ambient temperature, which is important for magnetic imaging and biomedical applications to monitor the location of the gel. The anisotropic structure of the hydrogel has good stability after incubation in water for more than 6 months or after ten cycles of heating–cooling treatments (Figure S15).

To afford the gel with tailored morphing ability, it is highly desired yet challenging to form sophisticated anisotropic structures so as to control the distribution of internal stresses. Here, hydrogels with patterned anisotropic structures of MDSs are developed by multi-step magnetic orientation and photolithographic polymerization. The stripe-patterned hydrogel with orthogonal orientations of MDSs shows different birefringence colors when observed under POM (Figure 4a). This gel slightly bends along the stripe direction in water due to the different swelling ratios of the stripes with orthogonal orientations of MDSs (Figure 2d); the swelling mismatch builds up internal stresses along the stripe and leads to weak out-of-plane buckling deformation. The patterned gel deforms into cylinder shape when placed in 40 °C water, which drastically enhances the swelling/contraction mismatch, internal stresses, and deformation amplitude of the gel (Figure 4b).[22] Different orientation of MDSs at specific regions can be produced by applying the rotating magnetic field and photo-polymerizing with a mask. Repeated procedures enable fabrication of composite hydrogel with complex alignments of MDSs. For example, a pear-like region is first polymerized with MDSs homotropically oriented in the southeastern direction, followed by creating an egg-like region with MDSs homotropically oriented in the eastern direction. Finally, the other region is polymerized with MDSs homogeneously oriented along the planar direction. Different birefringent patterns can be observed under POM. An orange pear-like pattern is observed when the gourd-shape is placed along the analyzer direction of the POM. After anticlockwise rotating the analyzer, polarizer, and tint plate by 22.5°, a gourd-like pattern with orange birefringence is observed. Another anticlockwise rotation by 22.5° results in an egg-like pattern with strong orange birefringence (Figure 4c); other birefringent patterns observed after further rotations are presented in Figure S16a. Similarly, birefringent patterns of digital numbers can also be encoded in the anisotropic gel. The homotropic alignments of MDSs and corresponding birefringent patterns are shown in Figure 4d and Figure S16b. Different birefringent numbers are observed in the same hydrogel, which depend on the relative position of the oriented direction of MDSs and the polarizers of POM. We should note that the patterns of the gels developed by multi-step polymerization are almost invisible under daylight (Figure S17). These properties of the patterned anisotropic hydrogels should be promising for camouflage and encryp-

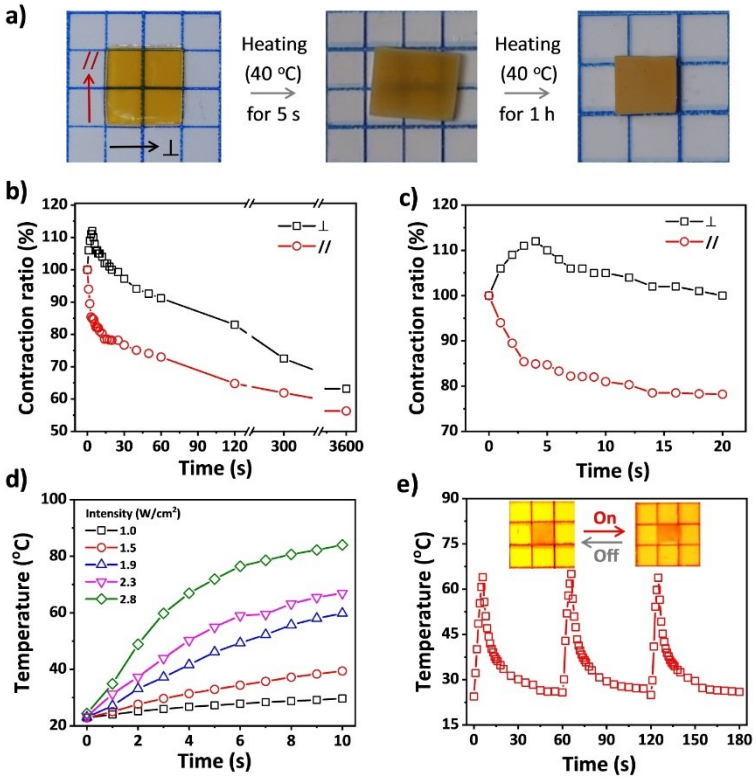

Figure 3. a) Photos showing the temperature-mediated anisotropic deformation of the hydrogel. b, c) Variations of the dimensions of the hydrogel after transferring it from 25 to 40 °C in a water bath. The initial change of the dimensions is enlarged in (c). d) Variations of local temperature of the anisotropic gel under irradiation of 520 nm light with different power intensity. e) Variations of the local temperature of the gel under cyclic irradiation of 520 nm light with the intensity of 2.34 W cm^{-2}. The insets present the anisotropic deformation of the gel under light irradiation.

tion of digital information. The resolution of the patterns in this work is ≈1 mm, which can be improved to tens of micrometers by using high-resolution masks and increasing the photopolymerization rate.[23]

The photo-responsiveness of the anisotropic hydrogel, moreover, enables local actuation for shape morphing and programmed locomotion. As a demonstration, the stripe-patterned hydrogel film previously shown in Figure 4a, which has alternating alignments of MDSs parallel or perpendicular to the stripe direction, is placed on a hydrophobic polyvinyl chloride (PVC) substrate and actuated by repeated unidirectional scanning (from left to right) of a laser beam to achieve a walking motion. Due to the swelling mismatch between the stripes with different alignments of MDSs, the patterned hydrogel slightly bends in water at room temperature.[9b,24] Localized irradiation dramatically increases the local temperature and improves the swelling/contraction mismatch, the internal stresses, and thus the bending amplitude of the stripe-patterned hydrogel.[9b] We initially expected the gel with a walking gait after cyclic directional scanning of the laser, which results in dynamic shape-changing and friction modulation of the gel against the PVC substrate by the hydrophilic-to-hydrophobic transition of PNIPAm matrix, as revealed in a previous work.[9b] However, the light-steered motion of this gel is not so efficient (Figure 5a and Movie S1), because the density of the gel (1.012 ± 0.003 g cm^{-3}) is too close to water (0.997 g cm^{-3}) at room temperature. When the laser beam scans from left to right, the hydrogel shows travelling bending with the left "foot" moving toward the middle, while the right "foot" remains static. The moving of the left "foot" in the same direction of the scanning laser results in a prolonged irradiation on the left part of the gel. The preferential moving of the left "foot" is probably because the local heating of the gel leads to upward flow of surrounding water and reduced friction of the left "foot" against the substrate. After the laser beam reaches the middle of the gel, the bending of the gel reaches the

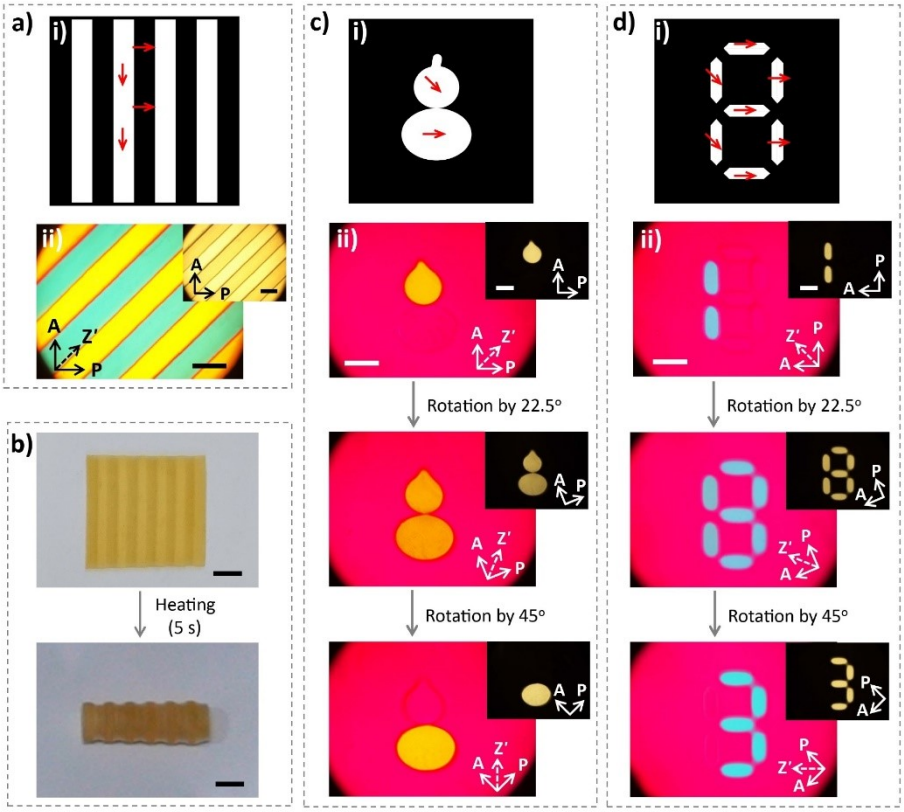

Figure 4. a) Schematic (i) and corresponding POM images (ii) of a stripe-patterned anisotropic hydrogel. b) Photos of the stripe-patterned anisotropic hydrogels before and after the shape changes upon incubation in a 40 °C warm water bath. The thickness of the sample is 0.6 mm. c,d) Schematic (i) and corresponding POM images (ii) of patterned hydrogels with different alignment of MDSs at specific regions by rotating the directions of analyzer, polarizer, and tint plate. The thickness of the samples is 0.4 mm. Scale bars in (a), (c), and (d) are 2 mm; scale bars in (b) are 5 mm.

maximum amplitude. When the laser continuously moves right, the recovery of the left part of the gel results in a movement of the left "foot" to the left. The right "foot" shows little displacement because of the much shorter time of laser irradiation. The uncontrollable friction of the "feet" against the substrate leads to negligible displacement of the intact hydrogel after one cycle of laser scanning.

To enhance the friction force so as to favor the locomotion, a magnet is placed beneath the hydrogel with a certain distance to generate magnetic force and thus to reduce the influence of buoyant force of the gel. Simulation results indicate that the hydrogel experiences magnetic force, which decreases with increasing distance between gel and magnet (Figure S18). When the magnetic force is applied with a gel-magnet distance of 2.7 mm, the gel shows a programmed walking motion under cyclic irradiation of a laser beam (Figure 5b and Movie S2). Due to the existing magnetic force, the slightly curved gel is now flattened. As the laser beam scans on the left part of the gel, the gel gradually deforms with the right "foot" moving left because the left "foot" with elevated temperature and enhanced hydrophobicity sticks on the hydrophobic substrate. As the laser moves to the right part of the gel, the left "foot" with decreased temperature moves left, and the right "foot" with elevated temperature sticks on the substrate. Such dynamic modulation of the friction force, together with the travelling bending deformation, leads to a high-efficiency directional walking motion of the hydrogel.

When the magnetic force is further increased by decreasing the gel-magnet distance to 0.3 mm, the light-steered motion is different from the aforementioned situations (Figure 5c and Movie S3). The gel cannot deform initially under the scanning laser beam because the internal stress within the gel is not sufficiently high to overcome the

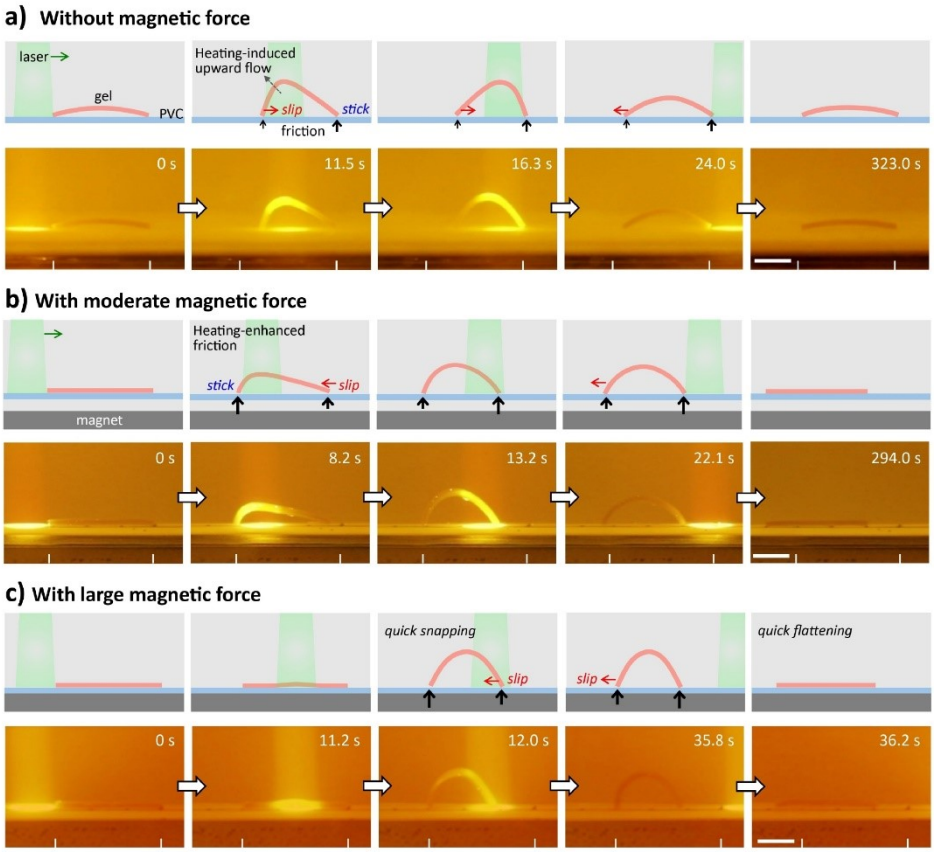

Figure 5. Snapshots showing the walking gait of the stripe-patterned anisotropic hydrogel under a scanning laser beam from left to right without magnetic force (a), with moderate magnetic force (b) and large magnetic force (c). Schematics are presented above the snapshots to show the motions of the two "feet". Gel dimensions, 15 mm × 5 mm × 0.6 mm; light intensity, 2.34 W cm^{-2}; scanning speed, 1 mm s^{-1}. Scale bar: 5 mm.

magnetic force and the friction force. As the light scanning continues, the internal stress gradually increases, which is released by a sudden move of the right "foot" of the gel to the left (completed in ≈1 s). As a consequence, the gel deforms into an arch. After switching off laser irradiation, the recovery of the gel from the arch to flat shape also completes abruptly with the gel instantly falling onto the substrate, when the gel recovers its volume and the unbending force is larger than the friction force to trigger the sliding of the "feet" on the substrate. After the occurrence of sliding, the flattening process of the gel is accelerated by the magnetic force. The sudden buckling and flattening of the hydrogel should be associated with the stick-slip transition under the competition between the internal stress and the friction force.

The distinct deformations and motions of the hydrogel manipulated by the magnetic field and photo actuation are related to the anisotropic structure and the multi-response of the MDSs. This combination of different stimulus-response properties of the hydrogels should facilitate the design and control of soft actuators and robots toward specific applications. Worth noting is that the multi-gait motions demonstrated above are different from the reported examples in terms of the kinematics (Table S1). In the achievements reported in the literatures, two strategies are usually applied to convert cyclic bending/unbending or stretching/contraction deformations into directional walking motions, i.e. by using a rachet plate or creating asymmetric shape of the gel to generate asymmetric friction against the substrate.[15] However, the hydrogel usually moves along predetermined direction, cannot move in the reverse direction or with a distinct gait. These issues have been addressed by cooperative manipulation of the magnetic field and spatiotemporal laser irradiation to afford the patterned

gel with multi-gait motions. A static magnetic field is applied to adjust the friction between the gel and the substrate, which changes the motion gait under dynamic light stimulation. The combined strategy should be informative for the design of soft actuators and robots.

Conclusion

In summary, we have developed a series of anisotropic hydrogels by using a rotating magnetic field to orient MDSs followed by polymerization of the precursor to fix the ordered structures. The resultant PNIPAm nanocomposite hydrogels with highly ordered MDSs have anisotropic optical and mechanical properties, and exhibit anisotropic responses to temperature or light irradiation. These properties are rooted in the unique attributes of MDSs with a sandwich-like structure, high aspect ratio, high charge density, and responsiveness to light and magnetic field. Hydrogels with sophisticated anisotropic structures of MDSs are further fabricated by multi-step magnetic orientation and photolithographic polymerization, which show different birefringent patterns and programmed deformations upon heating or light irradiation. Distinct motions are realized in the patterned hydrogel under spatiotemporal light irradiation with a static magnet to regulate the friction force between the gel and the substrate. The magneto-orientation-assisted fabrication of anisotropic hydrogels and the cooperative manipulation strategy for controllable motions should be informative for the design of high-performance hydrogel devices. These hydrogels with controllable anisotropic structures, multiple stimuli-responsiveness, programmable deformations and motions should find applications in biomedical and engineering fields as biomedical devices, soft actuators/robots, etc.

Acknowledgements

Z.L.W. thank the financial support from National Natural Science Foundation of China (51973189, 52173012) and Natural Science Foundation of Zhejiang Province of China (LR19E030002). Open Access funding enabled and organized by Projekt DEAL.

Conflict of Interest

The authors declare no conflict of interest.

Data Availability Statement

The data that support the findings of this study are available from the corresponding authors upon reasonable request.

Keywords: Anisotropic Hydrogels · Ferronematic Liquid Crystals · Magnetic Orientation · Nanosheets · Soft Robots

[1] a) U. G. K. Wegst, H. Bai, E. Saiz, A. P. Tomsia, R. O. Ritchie, *Nat. Mater.* **2015**, *14*, 23; b) M. Eder, S. Amini, P. Fratzl, *Science* **2018**, *362*, 543; c) D. Jiao, Q. L. Zhu, C. Y. Li, Q. Zheng, Z. L. Wu, *Acc. Chem. Res.* **2022**, *55*, 1533.

[2] a) K. Wang, J. Ren, S. Yang, H. Wang, *Adv. Mater. Technol.* **2021**, *6*, 2100158; b) Y. S. Zhang, A. Khademhosseini, *Science* **2017**, *356*, eaaf3627; c) Y. Zhao, C. Xuan, X. Qian, Y. Alsaid, M. Hua, L. Jin, X. He, *Sci. Robot.* **2019**, *4*, eaax7112.

[3] a) W. Wang, Y. Zhang, W. Liu, *Prog. Polym. Sci.* **2017**, *71*, 1; b) X. Zhao, X. Chen, H. Yuk, S. Lin, X. Liu, G. Parada, *Chem. Rev.* **2021**, *121*, 4309; c) Y. J. Wang, X. N. Zhang, Y. Song, Y. Zhao, L. Chen, F. Su, L. Li, Z. L. Wu, Q. Zheng, *Chem. Mater.* **2019**, *31*, 1430; d) C. N. Zhu, T. Bai, H. Wang, J. Ling, F. Huang, Z. L. Wu, *Adv. Mater.* **2021**, *33*, 2102023; e) Z. Jiang, M. L. Tan, M. Taheri, Q. Yan, T. Tsuzuki, M. G. Gardiner, B. Diggle, L. A. Connal, *Angew. Chem. Int. Ed.* **2020**, *59*, 7049; *Angew. Chem.* **2020**, *132*, 7115.

[4] a) M. J. Wakelam, *Biochem. J.* **1985**, *228*, 1; b) S. Jana, S. K. L. Levengood, M. Zhang, *Adv. Mater.* **2016**, *28*, 10588; c) H. N. Kim, A. Jiao, N. S. Hwang, M. S. Kim, D. H. Kang, D. H. Kim, K. Y. Suh, *Adv. Drug Delivery Rev.* **2013**, *65*, 536; d) J. G. Barber, A. M. Handorf, T. J. Allee, W. J. Li, *Tissue Eng. Part A* **2013**, *19*, 1265.

[5] a) M. T. I. Mredha, I. Jeon, *Prog. Mater. Sci.* **2022**, *124*, 100870; b) K. Sano, Y. Ishida, T. Aida, *Angew. Chem. Int. Ed.* **2018**, *57*, 2532; *Angew. Chem.* **2018**, *130*, 2558; c) N. Peng, D. Huang, C. Gong, Y. Wang, J. Zhou, C. Chang, *ACS Nano* **2020**, *14*, 16169; d) Z. Zhao, R. Fang, Q. Rong, M. Liu, *Adv. Mater.* **2017**, *29*, 1703045.

[6] a) W. Yang, S. Yamamoto, K. Sueyoshi, T. Inadomi, R. Kato, N. Miyamoto, *Angew. Chem. Int. Ed.* **2021**, *60*, 8466; *Angew. Chem.* **2021**, *133*, 8547; b) T. Inadomi, S. Ikeda, Y. Okumura, H. Hirotsugu, N. Miyamoto, *Macromol. Rapid Commun.* **2014**, *35*, 1741.

[7] a) S. Choi, J. Kim, *J. Mater. Chem. B* **2015**, *3*, 1479; b) S. H. Kim, S. K. Im, S. J. Oh, S. Jeong, E. S. Yoon, C. J. Lee, N. Choi, E. M. Hur, *Nat. Commun.* **2017**, *8*, 14346; c) P. Lin, T. Zhang, X. Wang, B. Yu, F. Zhou, *Small* **2016**, *12*, 4386.

[8] a) B. D. Wall, S. R. Diegelmann, S. Zhang, T. J. Dawidczyk, W. L. Wilson, H. E. Katz, H. Q. Mao, J. D. Tovar, *Adv. Mater.* **2011**, *23*, 5009; b) N. Miyamoto, M. Shintate, S. Ikeda, Y. Hoshida, Y. Yamauchi, R. Motokawa, M. Annaka, *Chem. Commun.* **2013**, *49*, 1082; c) Z. Zhu, Y. Li, H. Xu, X. Peng, Y. N. Chen, C. Shang, Q. Zhang, J. Liu, H. Wang, *ACS Appl. Mater. Interfaces* **2016**, *8*, 15637; d) K. Shikinaka, K. Kaneda, S. Mori, T. Maki, H. Masunaga, Y. Osada, K. Shigehara, *Small* **2014**, *10*, 1813.

[9] a) Q. L. Zhu, C. Du, Y. Dai, M. Daab, M. Matejdes, J. Breu, W. Hong, Q. Zheng, Z. L. Wu, *Nat. Commun.* **2020**, *11*, 5166; b) Q. L. Zhu, C. F. Dai, D. Wagner, M. Daab, W. Hong, J. Breu, Q. Zheng, Z. L. Wu, *Adv. Mater.* **2020**, *32*, 2005567; c) Q. L. Zhu, C. F. Dai, D. Wagner, O. Khoruzhenko, W. Hong, J. Breu, Q. Zheng, Z. L. Wu, *Adv. Sci.* **2021**, *8*, 2102353; d) Y. Guo, Y. Chen, E. Wang, M. Cakmak, *ACS Appl. Mater. Interfaces* **2017**, *9*, 919; e) M. Yang, Y. Xu, X. Zhang, H. K. Bisoyi, P. Xue, Y. Yang, X. Yang, C. Valenzuela, Y. Chen, L. Wang, W. Feng, Q. Li, *Adv. Funct. Mater.* **2022**, *32*, 2201884; f) T. Inadomi, K. Urayama, N. Miyamoto, *ACS Appl. Polym. Mater.* **2022**, https://doi.org/10.1021/acsapm.2c00103; g) P. Xue, H. K. Bisoyi, Y. Chen, H. Zeng, J. Yang, X. Yang, P. Lv, X. Zhang, A. Priimagi, L. Wang, X. Xu, Q. Li, *Angew. Chem. Int. Ed.* **2021**, *60*, 3390; *Angew. Chem.* **2021**, *133*, 3432.

[10] a) W. Shi, J. Huang, R. Fang, M. Liu, *ACS Appl. Mater. Interfaces* **2020**, *12*, 5177; b) K. Li, J. Xu, P. Li, Y. Fan, *Composites Part B* **2022**, *228*, 109401.

[11] a) J. Kim, S. E. Chung, S. E. Choi, H. Lee, J. Kim, S. Kwon, *Nat. Mater.* **2011**, *10*, 747; b) K. Hu, J. Sun, Z. Guo, P. Wang, Q. Chen, M. Ma, N. Gu, *Adv. Mater.* **2015**, *27*, 2507; c) S. R. Goudu, I. C. Yasa, X. Hu, H. Ceylan, W. Hu, M. Sitti, *Adv. Funct. Mater.* **2020**, *30*, 2004975; d) C. Li, G. C. Lau, H. Yuan, A. Aggarwal, V. L. Dominguez, S. Liu, H. Sai, L. C. Palmer, N. A. Sather, T. J. Pearson, D. E. Freedman, P. K. Amiri, M. O. de la Cruz, S. I. Stupp, *Sci. Robot.* **2020**, *5*, eabb9822.

[12] a) L. Wu, M. Ohtani, M. Takata, A. Saeki, S. Seki, Y. Ishida, T. Aida, *ACS Nano* **2014**, *8*, 4640; b) T. Lan, B. Ding, Z. Huang, F. Bian, Y. Pan, H. M. Cheng, B. Liu, *J. Am. Chem. Soc.* **2021**, *143*, 12886; c) S. Yook, S. Shams Es-Haghi, A. Yildirim, Z. Mutlu, M. Cakmak, *Soft Matter* **2019**, *15*, 9733; d) F. Lin, Z. Zhu, X. Zhou, W. Qiu, C. Niu, J. Hu, K. Dahal, Y. Wang, Z. Zhao, Z. Ren, D. Litvinov, Z. Liu, Z. M. Wang, J. Bao, *Adv. Mater.* **2017**, *29*, 1604453.

[13] a) R. M. Erb, J. S. Sander, R. Grisch, A. R. Studart, *Nat. Commun.* **2013**, *4*, 1712; b) R. M. Erb, R. Libanori, N. Rothfuchs, A. R. Studart, *Science* **2012**, *335*, 199; c) H. Le Ferrand, F. Bouville, T. P. Niebel, A. R. Studart, *Nat. Mater.* **2015**, *14*, 1172; d) E. Poloni, A. Rafsanjani, V. Place, D. Ferretti, A. R. Studart, *Adv. Mater.* **2022**, *34*, 2104874.

[14] a) M. Liu, Y. Ishida, Y. Ebina, T. Sasaki, T. Hikima, M. Takata, T. Aida, *Nature* **2015**, *517*, 68; b) Z. Sun, Y. Yamauchi, F. Araoka, Y. S. Kim, J. Bergueiro, Y. Ishida, Y. Ebina, T. Sasaki, T. Hikima, T. Aida, *Angew. Chem. Int. Ed.* **2018**, *57*, 15772; *Angew. Chem.* **2018**, *130*, 15998; c) K. Sano, Y. O. Arazoe, Y. Ishida, Y. Ebina, M. Osada, T. Sasaki, T. Hikima, T. Aida, *Angew. Chem. Int. Ed.* **2018**, *57*, 12508; *Angew. Chem.* **2018**, *130*, 12688; d) Y. S. Kim, M. Liu, Y. Ishida, Y. Ebina, M. Osada, T. Sasaki, T. Hikima, M. Takata, T. Aida, *Nat. Mater.* **2015**, *14*, 1002.

[15] a) H. Shahsavan, A. Aghakhani, H. Zeng, Y. Guo, Z. S. Davidson, A. Priimagi, M. Sitti, *Proc. Natl. Acad. Sci. USA* **2020**, *117*, 5125; b) Z.-C. Jiang, Y.-Y. Xiao, X. Tong, Y. Zhao, *Angew. Chem. Int. Ed.* **2019**, *58*, 5332; *Angew. Chem.* **2019**, *131*, 5386.

[16] a) O. Khoruzhenko, D. R. Wagner, S. Mangelsen, M. Dulle, S. Förster, S. Rosenfeldt, V. Dudko, K. Ottermann, G. Papastavrou, W. Bensch, J. Breu, *J. Mater. Chem. C* **2021**, *9*, 12732; b) K. Ament, D. R. Wagner, F. E. Meij, F. E. Wagner, J. Breu, *Z. Anorg. Allg. Chem.* **2020**, *646*, 1110.

[17] a) S. Rosenfeldt, M. Stöter, M. Schlenk, T. Martin, R. Q. Albuquerque, S. Förster, J. Breu, *Langmuir* **2016**, *32*, 10582; b) M. Daab, S. Rosenfeldt, H. Kalo, M. Stöter, B. Bojer, R. Siegel, S. Förster, J. Senker, J. Breu, *Langmuir* **2017**, *33*, 4816; c) M. Stöter, S. Godrich, P. Peicht, S. Rosenfeldt, H. Thurn, J. W. Neubauer, M. Seuss, P. Lindner, H. Kalo, M. Moller, A. Fery, S. Porster, G. Papastavrou, J. Breu, *Angew. Chem. Int. Ed.* **2016**, *55*, 7398; *Angew. Chem.* **2016**, *128*, 7524.

[18] L. Qiao, C. Du, J. P. Gong, Z. L. Wu, Q. Zheng, *Adv. Mater. Technol.* **2019**, *4*, 1900665.

[19] a) R. M. Erb, J. Segmehl, M. Schaffner, A. R. Studart, *Soft Matter* **2013**, *9*, 498; b) H. Le Ferrand, A. F. Arrieta, *Soft Matter* **2022**, *18*, 1054.

[20] H. Qin, T. Zhang, N. Li, H. Cong, S. Yu, *Nat. Commun.* **2019**, *10*, 2202.

[21] a) K. Li, H. Nejadnik, H. E. Daldrup-Link, *Drug Discovery Today* **2017**, *22*, 1421; b) M. Saeed, W. Ren, A. Wu, *Biomater. Sci.* **2018**, *6*, 708; c) P. Martinkova, M. Brtnicky, J. Kynicky, M. Pohanka, *Adv. Healthcare Mater.* **2018**, *7*, 1700932.

[22] H. Aharoni, Y. Xia, X. Zhang, R. D. Kamien, S. Yang, *Proc. Natl. Acad. Sci. USA* **2018**, *115*, 7206.

[23] a) S.-J. Jeon, A. W. Hauser, R. C. Hayward, *Acc. Chem. Res.* **2017**, *50*, 161; b) A. Cangialosi, C. Yoon, J. Liu, Q. Huang, J. Guo, T. D. Nguyen, D. H. Gracias, R. Schulman, *Science* **2017**, *357*, 1126; c) F. Huang, M. Chen, Z. Zhou, R. Duan, F. Xia, I. Willner, *Nat. Commun.* **2021**, *12*, 2364.

[24] a) Z. L. Wu, M. Moshe, J. Greener, H. Therien-Aubin, Z. Nie, E. Sharon, E. Kumacheva, *Nat. Commun.* **2013**, *4*, 1586; b) C. N. Zhu, C. Y. Li, H. Wang, W. Hong, F. Huang, Q. Zheng, Z. L. Wu, *Adv. Mater.* **2021**, *33*, 2008057; c) C. Y. Li, S. Y. Zheng, X. P. Hao, W. Hong, Q. Zheng, Z. L. Wu, *Sci. Adv.* **2022**, *8*, eabm9608.

Manuscript received: May 17, 2022
Accepted manuscript online: June 24, 2022
Version of record online: July 14, 2022

Angewandte Chemie
Eine Zeitschrift der Gesellschaft Deutscher Chemiker

Supporting Information

Magneto-Orientation of Magnetic Double Stacks for Patterned Anisotropic Hydrogels with Multiple Responses and Modulable Motions

C. F. Dai, O. Khoruzhenko, C. Zhang, Q. L. Zhu, D. Jiao, M. Du, J. Breu, P. Zhao*, Q. Zheng*, Z. L. Wu**

Experimental Section

Materials

N-isopropylacrylamide (NIPAm) was used as received from Tokyo Chemical Industry Co., Ltd. *N*,*N*′-methylenebis(acrylamide) (MBAA) was purchased from Aladdin Chemistry Co., Ltd. Lithium phenyl-2,4,6-trimethylbenzoylphosphinate (LAP) was synthesized according to the reported process.[S1] MDS was synthesized by adapting the reported procedure.[S2] The content of γ-Fe_2O_3 was fixed at 16.6 wt%. Aqueous suspensions of MDS (1 wt%) were prepared by adding prescribed amount of MDS power to water. The mixture was oscillated with a speed of 120 r.p.m. for 24 h at room temperature, which led to repulsive osmotic delamination into a ferronematic suspension consisting of singular MDSs with a sandwich-like structure. Millipore deionized water was used in all the experiments.

Synthesis of magnetic anisotropic hydrogels

The precursor suspension was prepared by dissolving a prescribed amount of NIPAm (1 mol/L), MBAA (3 mol%, relative to NIPAm), and LAP (6 mol%, relative to NIPAm) in the homogeneous suspension of MDS (1 wt%). After injecting the aqueous precursor suspension into the reaction cell consisting of a pair of parallel glass substrates with silicon spacer of a specific thickness, a static or rotating magnetic field was applied to direct the alignment of MDSs. After the magnetic orientation for a short while, the reaction cell was immediately exposed to UV light for 10 s to initiate the polymerization and crosslinking to obtain the anisotropic hydrogel.

The isotropic hydrogel containing randomly dispersed MDSs was prepared according to a similar protocol. After injection of the precursor, the reaction cell was oscillated with a speed of 60 rpm for 2 h at an elevated temperature to accelerate the structural relaxation of the shear-induced alignment of MDSs. Then, the reaction cell was cooled down to room temperature and placed under UV light irradiation for 10 s to trigger the polymerization. The obtained hydrogel was incubated in water to achieve the equilibrium state.

Patterned anisotropic hydrogels with complex ordered structures were fabricated by a multi-step magnetic orientation of MDSs and photolithographic polymerization. After the magnetic orientation of MDSs in the precursor suspension, the reaction cell was exposed to UV light for 10 s through a photo mask. After rotating the reaction cell to a certain angle, the rotating magnetic field was applied for 20 s, and the sample covered with another photo mask (or without photo mask) was exposed to

UV light for 10 s, resulting in polymerization of the precursor at specific regions. The process was repeated until the whole precursor suspension was polymerized to fix the ordered structures of the MDSs. The obtained patterned hydrogel was incubated into a large amount of water for several days to remove the residuals and achieve the equilibrium state.

Locomotion of the stripe-patterned hydrogels

Motions of the stripe-patterned hydrogel were realized under cyclic scanning of a laser beam (wavelength: 520 nm; intensity: 2.34 W/cm^2; spot diameter: 7 mm) from left to right of the rectangular hydrogel film (dimensions: 15 mm × 5 mm × 0.6 mm) placed on the polyvinyl chloride (PVC) substrate. The magnetic force was applied and adjusted by placing a N52 magnet (dimensions: 10 cm × 1 cm × 0.5 cm) under the PVC substrate with a specific distance. The locomotion was recorded by a digital camera with a cut-off filter (550–1100 nm) to filter out the strong green light.

Characterizations

The surface topography of MDSs was determined by atomic force microscopic (AFM) measurements. The image was acquired with a Dimension Icon (Bruker Nano Inc.) in PeakForce tapping mode in air. Magnetic hysteresis loops of γ-Fe_2O_3 nanoparticles, MDS powders, MDS suspension, and nanocomposite hydrogel were measured at room temperature by a Superconducting Quantum Interference Device (MPMS-XL-5) with the maximum applied magnetic field of 20000 Oe (Figure S19). The distribution of magnetic force of the nanocomposite hydrogel atop the elongated magnet was obtained by COMSOL simulation.

Absorption spectra were obtained by a UV-1800 spectrometer (Shimadzu Corp., Japan) at room temperature. The anisotropic gel was kept in a quartz cuvette with an optical path of 1 mm for measurement. To monitor the photothermal effect of the hydrogel, the localized temperature under irradiation of green light (520 nm) was measured by an infrared imager (Fotric 285).

The birefringent photos of MDS suspensions (1 wt %) were taken under a pair of polarizing films. The anisotropic hydrogels were observed under a POM (LV100N POL, Nikon) with and without a 530 nm tint plate. The gels with thickness of 0.5 mm were cut into strips with a width of ~0.5 mm for the cross-section observations. SAXS measurements were conducted on Xeuss SAXS system (Xenocs SA) with X-ray wavelength of 0.154 nm and beam spot of 172 × 172 μm^2. The distance between the sample and the detector was 1371 mm. The orientation degree (π) of MDSs in the hydrogel was calculated according to the equation of $\pi = (180–H)/180$, where H is the half width

of the peak of the azimuthal plot from the selected equatorial reflection.

The variations in // and ⊥ direction of the hydrogel prepared with rotating magnetic field are calculated as $S(//) = L_1/L_0$, and $S(\perp) = W_1/W_0$, respectively, in which L and W are the dimension in // and ⊥ directions. The subscript numbers 1 and 0 correspond to the deformed state and the original equilibrated state, respectively. The dimensions of hydrogels were analyzed from the snapshots of a movie that recorded the fast shape deformation of the gel after being transferred from a 25 °C water bath into a 40 °C water bath or being directly irradiated under 520 nm green light (intensity, 2.34 W/cm^2) at room temperature.

The mechanical properties of anisotropic and isotropic hydrogels containing MDSs were measured at room temperature using a tensile tester (Instron 3343). The anisotropic gel was cut into dumbbell-shaped samples, with a gauge length of 12 mm and a width of 2 mm, along the // or ⊥ direction. The isotropic hydrogel (without long-range orientation of MDSs) was also tested for comparison. Tensile tests were performed at a stretching rate of 100 mm/min. Young's modulus (E) (calculated with a strain below 7%), tensile breaking stress (σ_b), and breaking strain (ε_b) were obtained from three parallel measurements.

References

[S1] a) E. Majima, W. Schnabel, W. Weber, *Macromol. Chem. Phys.* **1991**, *192*, 2307; b) B. D. Fairbanks, M. P. Schwartz, C. N. Bowman, K. S. Anseth, *Biomaterials* **2009**, *30*, 6702.

[S2] O. Khoruzhenko, D. R. Wagner, S. Mangelsen, M. Dulle, S. Förster, S. Rosenfeldt, V. Dudko, K. Ottermann, G. Papastavrou, W. Bensch, J. Breu, *J. Mater. Chem. C* **2021**, *9*, 12732.

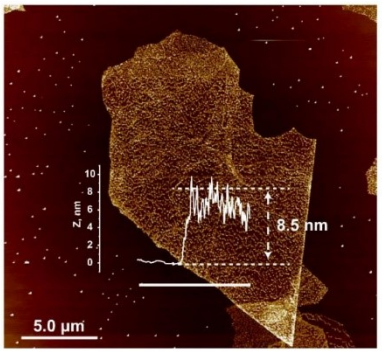

Figure S1. Topographical atomic force microscope (AFM) image and the height-length curves of an MDS.

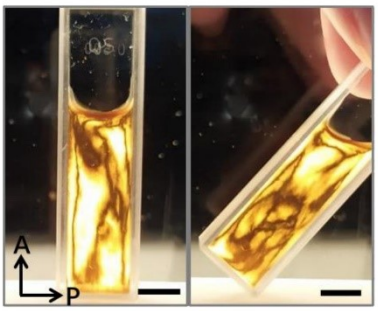

Figure S2. Photos of a ferronematic aqueous suspension with 1 wt% of MDS under crossed polarizing films. A: analyzer; P: polarizer. Scale bar: 5 mm.

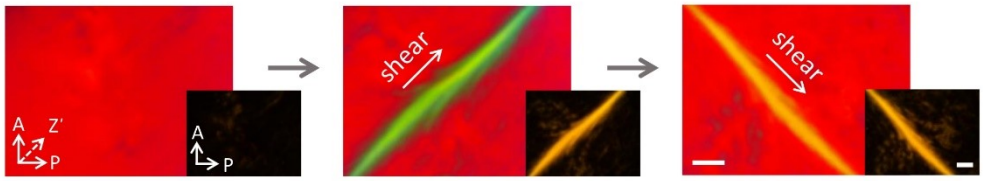

Figure S3. Mechanical shear-induced orientation of MDSs in suspension. Aqueous suspension with 1 wt% of MDS was dripped on a glass substrate, and a mechanical shear was applied to the suspension by using a syringe needle, which resulted in local orientation of MDSs along the shearing direction and strong birefringence under POM. A: analyzer; P: polarizer; Z′: slow axis of the 530 nm tint plate. Scale bar: 1 mm.

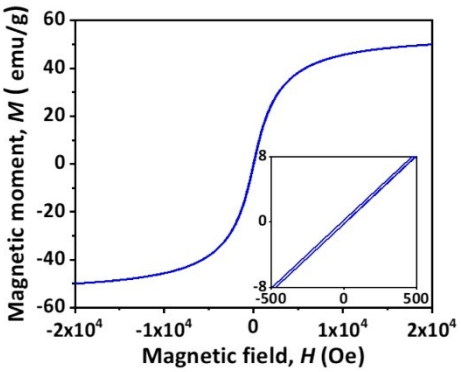

Figure S4. Magnetic hysteresis loop of γ-Fe_2O_3 nanoparticles. The diameter of γ-Fe_2O_3 nanoparticles is 5.5 ± 1.1 nm.

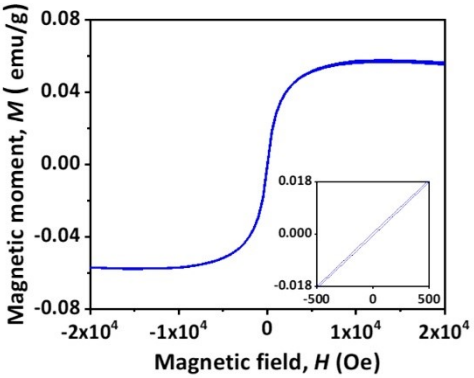

Figure S5. Magnetic hysteresis loop of aqueous suspension with 1 wt% of MDS.

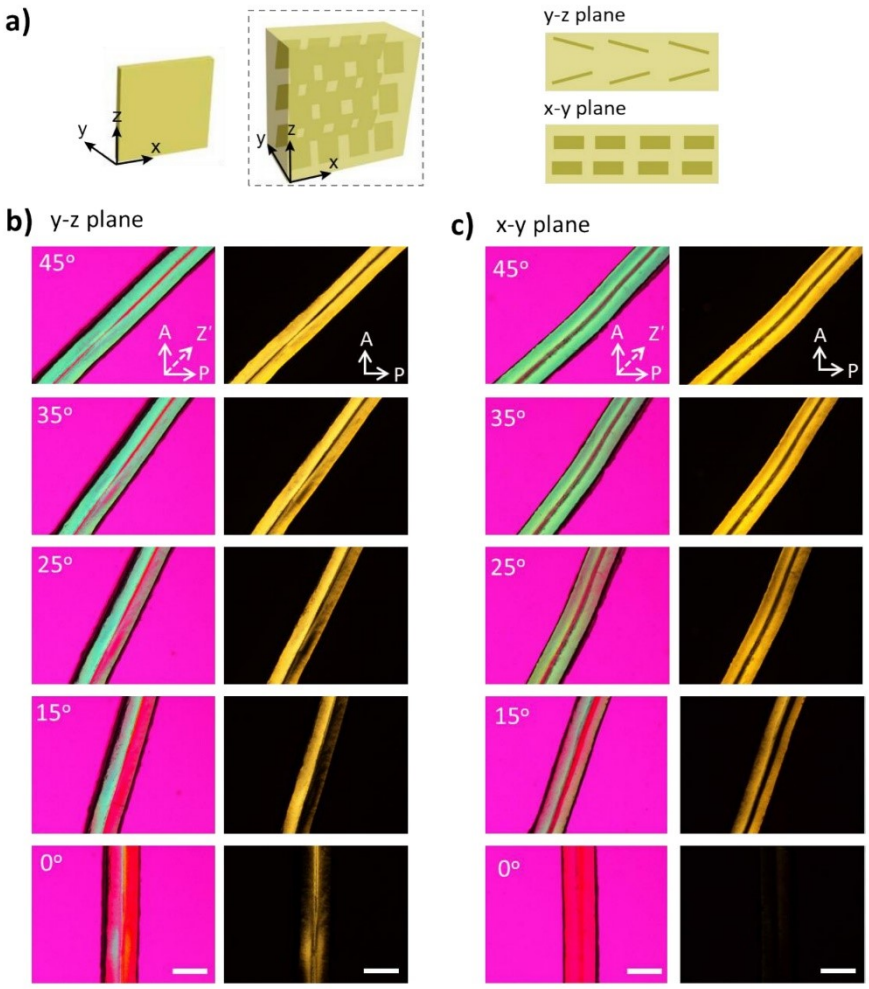

Figure S6. (a) Schematic showing the alignments of MDSs in the hydrogel prepared in the absence of magnetic fields. (b,c) POM images of the hydrogel observed from different directions: (b) y-z plane; (c) x-y plane. The sample was gradually rotated and then observed under POM with and without tint plate. The angle between the hydrogel and the analyzer is given in the POM image. Scale bar: 1 mm.

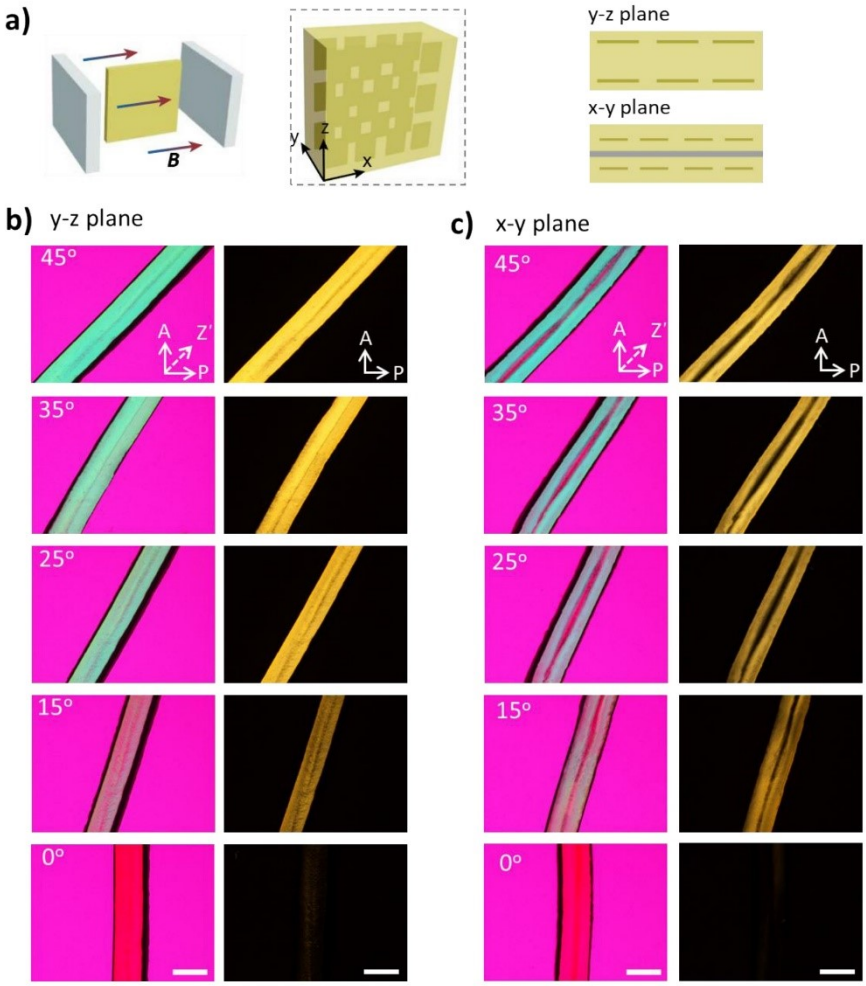

Figure S7. (a) Schematic showing the alignments of MDSs in the hydrogel prepared with static magnetic fields applied. (b,c) POM images of the hydrogel observed from different directions: (b) y-z plane; (c) x-y plane. The sample was gradually rotated and then observed under POM with and without tint plate. The angle between the hydrogel and the analyzer is given in the POM image. Scale bar: 1 mm.

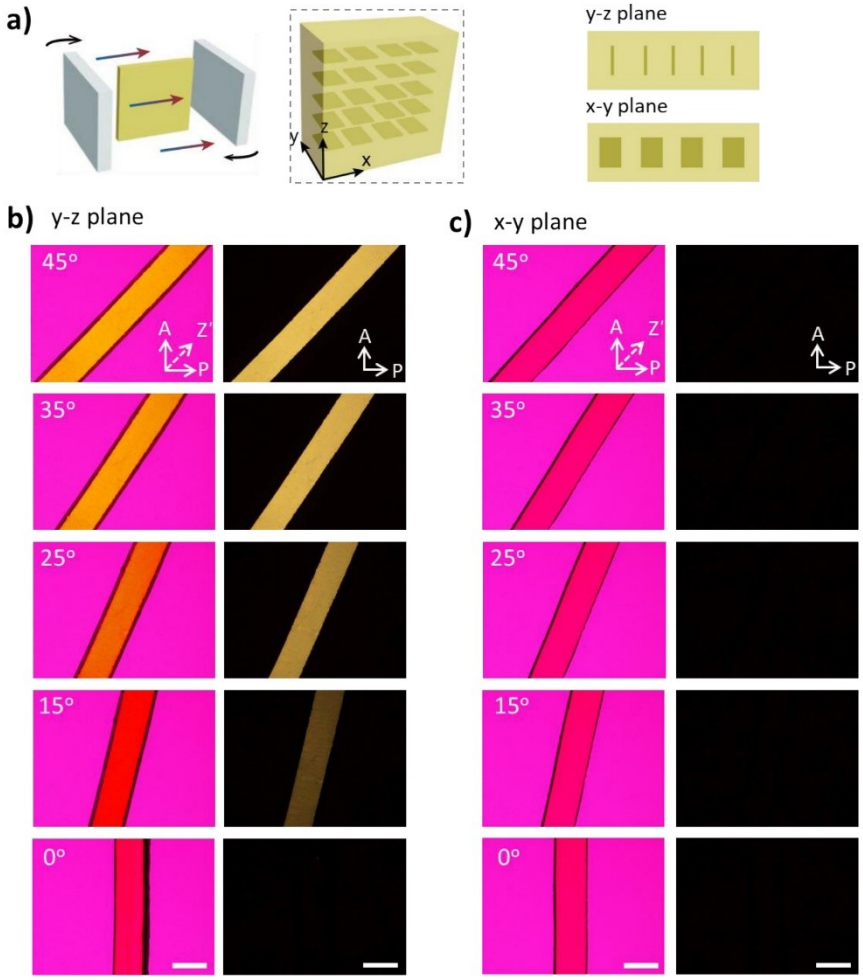

Figure S8. (a) Schematic showing the alignments of MDSs in the hydrogel prepared with rotating magnetic fields. (b,c) POM images of the hydrogel observed from different directions: (b) y-z plane; (c) x-y plane. The sample was gradually rotated and then observed under POM with and without tint plate. The angle between the hydrogel and the analyzer is given in the POM image. Scale bar: 1 mm.

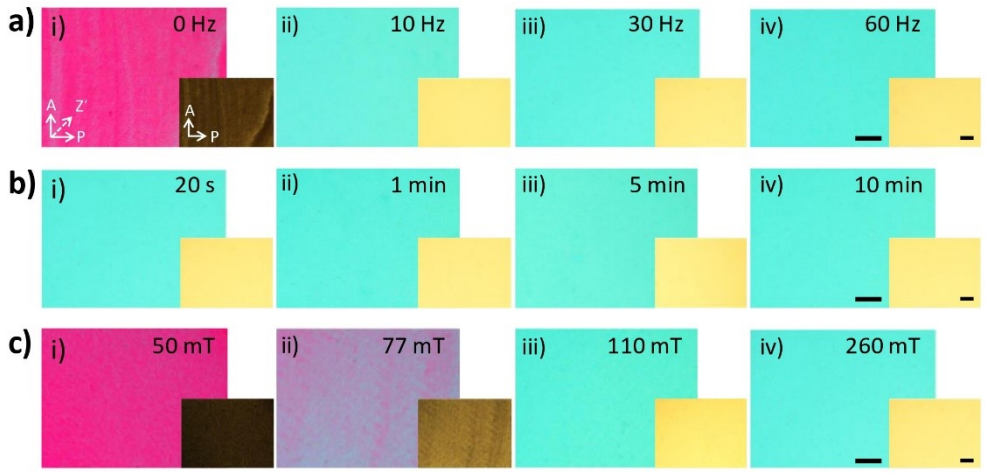

Figure S9. Anisotropic nanocomposite gel prepared with rotating magnetic fields under different experimental conditions. The experimental conditions were optimized by examining the birefringence of the gel with varying rotating frequency (a), action time (b) and magnetic strength (c). The experiments are designed by changing one parameter each time. The optimum was found with the following parameter set: rotating frequency of 30 Hz, action time of 20 s, intensity of magnetization of 260 mT. Scale bar: 2 mm.

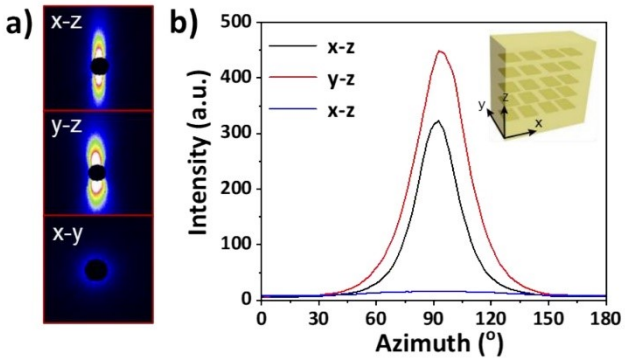

Figure S10. 2D SAXS patterns (a) and scattering intensity-azimuth plots (b) of the equilibrated hydrogel prepared with rotating magnetic fields.

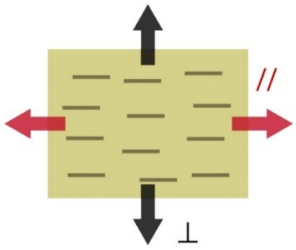

Figure S11. Schematic of the tensile directions of the equilibrated hydrogel prepared with rotating magnetic fields.

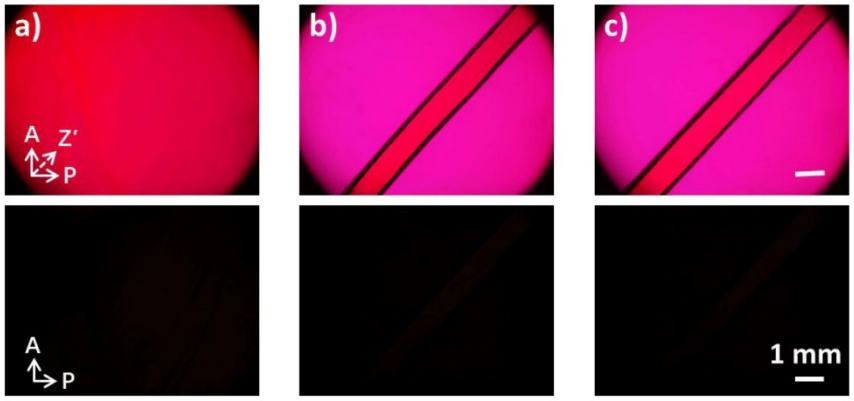

Figure S12. POM images of the MDS-containing isotropic hydrogel sheet observed from the top (a) and two orthogonal cross-sections (b, c). Thickness of gel: 1 mm. For the synthesis of isotropic gel, the reaction cell containing the precursor is oscillated with a speed of 60 rpm for 2 h at an elevated temperature to accelerate the structural relaxation of the shear-induced alignment of MDSs, which is followed by cooling to room temperature and then polymerizing under UV light irradiation.

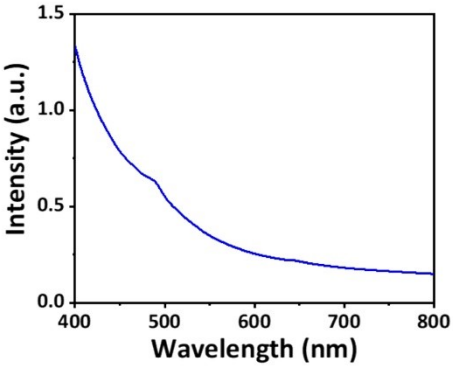

Figure S13. Absorption spectra of the hydrogel with 1 wt% of MDS prepared with rotating magnetic fields.

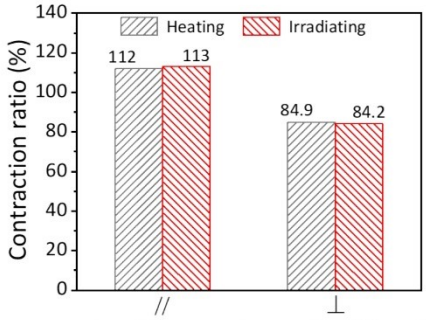

Figure S14. The maximum contraction difference in parallel (//) and perpendicular (⊥) direction incubated in warm water (40 °C) or irradiated by a green laser.

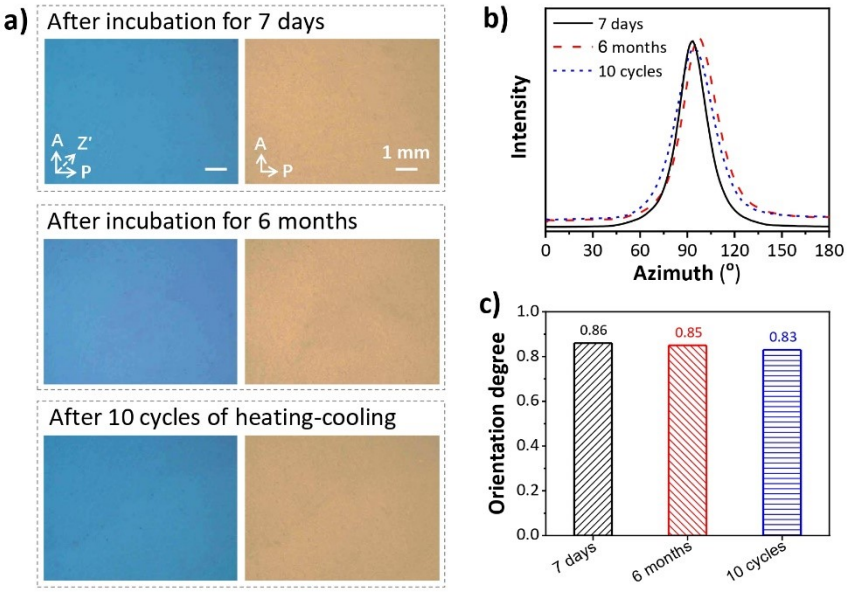

Figure S15. POM images (a), scattering intensity-azimuth plots (b), and orientation degree of MDSs in the anisotropic hydrogel after incubation in water for 7 days and 6 months, as well as after 10 cycles of heating-cooling treatments. Thickness of gel: 1 mm.

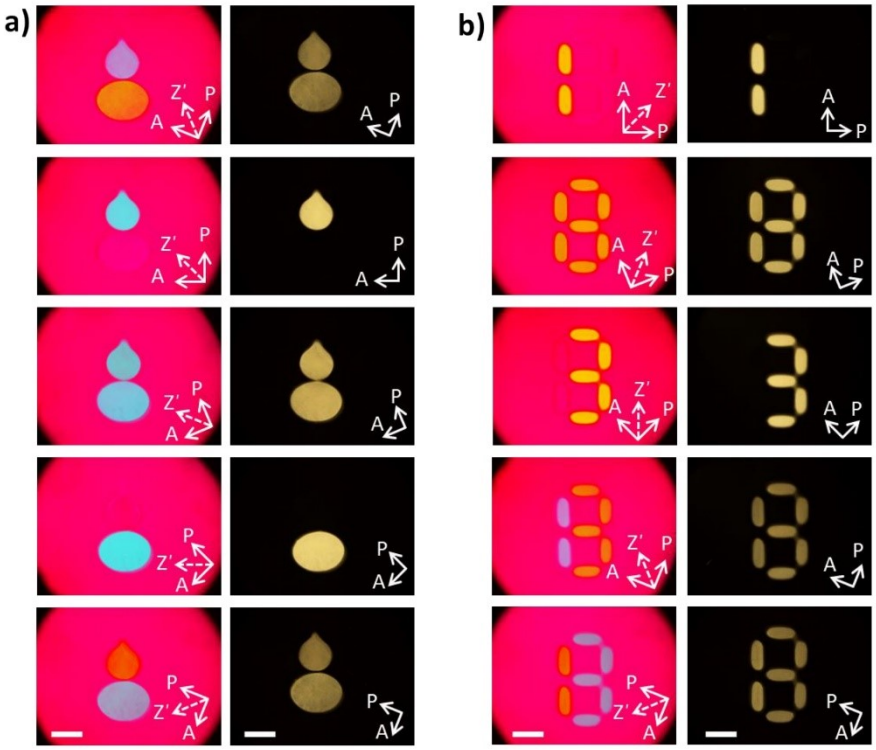

Figure S16. Additional POM images (ii) of patterned hydrogels with different alignment of MDSs at specific regions by rotating the directions of analyzer, polarizer, and tint plate. The thickness of the samples is 0.4 mm. Scale bar: 2 mm.

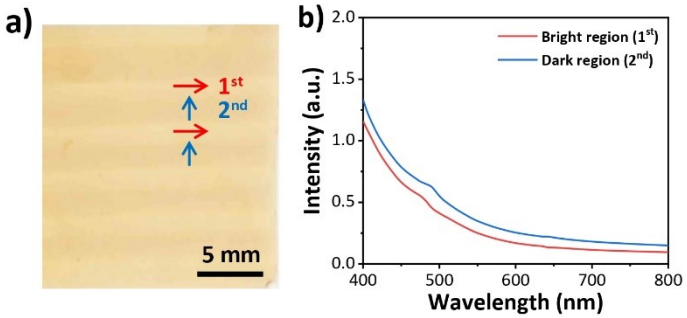

Figure S17. (a) Digital photo of stripe-patterned hydrogel under daylight. The relatively bright and dark stripes with orthogonal alignments of MDSs are synthesized multi-step photopolymerization. (b) UV-vis absorption spectra of the bright and dark regions of the patterned gel.

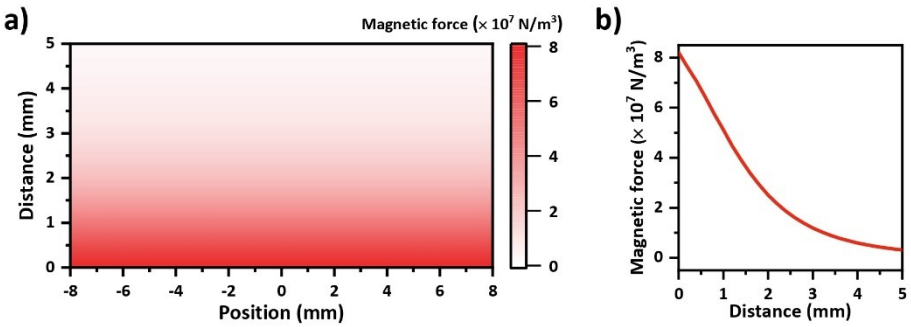

Figure S18. (a) Simulation result of the relationship between the exerted magnetic force and the position and distance of the hydrogel placed above an elongated magnet. (b) Variation of the exerted magnetic force as a function of the distance between the gel and the magnet.

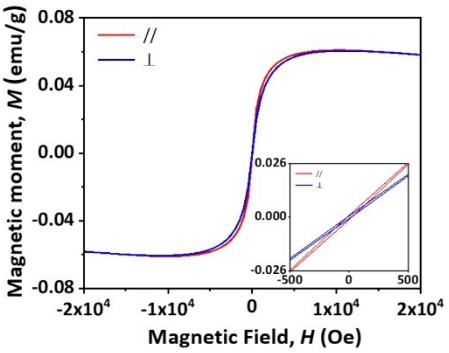

Figure S19. Magnetic hysteresis loops of gel in parallel (//) (a) and perpendicular (⊥) (b) direction.

Table S1. Comparison of responsive anisotropic hydrogels containing nanofillers as soft actuators and robots.

Material systems	Strategies for orientation of nanofillers	Achievements	Limitations	Ref.
PNIPAm hydrogel embedded with oriented titanate nanosheets (TiNSs)	Magneto-orientation by using a superconducting magnet (10 T)	Directional walking of gel with asymmetric shape by cyclic heating-cooling	The gel cannot move in the reverse direction; it took time to switch the heating and cooling.	S3
PNIPAm hydrogel embedded with oriented TiNSs and randomly dispersed AuNPs	Magneto-orientation by using a superconducting magnet (10 T)	Crawling of cylinder gel in a confined tube under scanning of a laser beam	A confined space was needed for the motion; the AuNPs might be leaked out of the gel matrix.	S4
PNIPAm hydrogel embedded with oriented alumina platelets decorated with Fe_3O_4 nanoparticles	Magneto-orientation under a rotating magnetic field using a rare-earth magnet	Programmed deformation of the gel with a bilayer structure upon heating	Deformations were slow and limited by water diffusion; it was difficult to develop anisotropic gel with sophisticated structures.	S5
Photo-responsive hydrogel embedded with oriented nickel nanowires	Magneto-orientation under static magnetic field using NdFeB rare-earth magnet	Locomotion by cooperative manipulation of light and magnetic field.	Precise manipulation of dynamic magnetic field was required; it was difficult to develop sophisticated anisotropic structures.	S6
PNIPAm hydrogel with oriented fluorohectorite nanosheets	Electro-orientation under an alternating electric field	Programmed deformation of the gel upon heating	Deformation cannot be locally and remotely triggered; it took time to switch the heating and cooling.	S7
PNIPAm hydrogel with spatially distributed MXene nanosheets	Electric field-directed electrophoresis of nanosheets	Programmed deformation of the gel upon near-infrared light irradiation	The orientation degree of nanosheets was relatively low; locomotion had not been investigated.	S8

References

[S3] Y. S. Kim, M. Liu, Y. Ishida, Y. Ebina, M. Osada, T. Sasaki, T. Hikima, M. Takata, T. Aida, *Nat. Mater.* **2015**, *14*, 1002.

[S4] Z. Sun, Y. Yamauchi, F. Araoka, Y. S. Kim, J. Bergueiro, Y. Ishida, Y. Ebina, T. Sasaki, T. Hikima, T. Aida, *Angew. Chem. Int. Ed.* **2018**, *57*, 15772.

[S5] R. M. Erb, J. S. Sander, R. Grisch, A. R. Studart, *Nat. Commun.* **2013**, *4*, 1712.

[S6] C. Li, G. C. Lau, H. Yuan, A. Aggarwal, V. L. Dominguez, S. Liu, H. Sai, L. C. Palmer, N. A.

Sather, T. J. Pearson, D. E. Freedman, P. K. Amiri, M. O. de la Cruz, S. I. Stupp, *Sci. Robot.* **2020**, *5*, eabb9822.
[S7] T. Inadomi, K. Urayama, N. Miyamoto, *ACS Appl. Polym. Mater.* **2022**, DOI: 10.1021/acsapm.2c00103.
[S8] P. Xue, K. Bisoyi, Y. Chen, H. Zeng, J. Yang, X. Yang, P. Lv, X. Zhang, A. Priimagi, L. Wang, X. Xu, Q. Li, *Angew. Chem. Int. Ed.* **2021**, *60*, 3390.

Legends for supplementary movies

Movie S1. Inefficient walking of the patterned hydrogel strip under scanning light without the magnetic force. Gel dimensions: 15 mm × 5 mm × 0.6 mm; light intensity: 2.34 W/cm^2; scanning speed: 1 mm/s. Movie speed, 5×.

Movie S2. Walking of the patterned hydrogel strip under scanning light with moderate magnetic force. Gel dimensions: 15 mm × 5 mm × 0.6 mm; light intensity: 2.34 W/cm^2; scanning speed: 1 mm/s. Movie speed, 5×.

Movie S3. Walking of the patterned hydrogel strip under light scanning with large magnetic force. Gel dimensions: 15 mm × 5 mm × 0.6 mm; light intensity: 2.34 W/cm^2; scanning speed: 1 mm/s. Movie speed, 5×.

FABRICATING DEFOGGING METASURFACES VIA A WATER-BASED COLLOIDAL ROUTE

Olena Khoruzhenko,[a] Volodymyr Dudko,[a] Sabine Rosenfeldt,[a] and Josef Breu,[a]*

* Corresponding authors

[a] Department of Chemistry and Bavarian Polymer Institute, University of Bayreuth, Universitätsstr. 30, 95440 Bayreuth, Germany

Submitted to Material Horizons 2023

ARTICLE

Fabricating defogging metasurfaces via a water-based colloidal route

Received 00th January 20xx,
Accepted 00th January 20xx

DOI: 10.1039/x0xx00000x

Olena Khoruzhenko,[a] Volodymyr Dudko,[a] Sabine Rosenfeldt,[a] and Josef Breu *[a]

Metamaterials possess exotic properties that do not occur in nature and have attracted significant attention in research and engineering. Two decades ago, the field of metamaterials emerged from linear electromagnetism, and today it encompasses a wide range of aspects related to solid matter, including electromagnetic and optical, mechanical and acoustic, as well as unusual thermal or mass transport phenomena. Combining different material properties can lead to emergent synergistic functions applicable in everyday life. Nevertheless, making such metamaterials in a robust, facile, and scalable manner is still challenging. This paper presents an effective protocol allowing for metasurfaces offering a synergy between optical and thermal properties. It utilizes liquid crystalline suspensions of nanosheets comprising two transparent silicate monolayers in a double stack, where gold nanoparticles are sandwiched between the two silicate monolayers. The colloidally stable suspension of nanosheets was applied in nanometre-thick coatings onto various substrates. The transparent coatings serve as absorbers in the infrared spectrum allowing for efficient conversion of sunlight into heat. The peculiar metasurface couples plasmon-enhanced adsorption with anisotropic heat conduction in the plane of the coating, both at the nanoscale. Processing of the coating is based on scalable and affordable wet colloidal processing instead of having to apply physical deposition in high vacuum or lithographic techniques. Upon solar irradiation, the colloidal metasurface is quickly (60% faster compared to the non-coated glass) heated to the level where complete defogging is assured without sacrificing transparency in the visible range. The protocol is generally applicable allowing for intercalation of any nanoparticles covering a range of physical properties that are then inherited to colloidal nanosheets. Because of their large aspect ratio the nanosheets will inevitably orient parallel to any surface. This will allow for a toolbox capable of mimicking metamaterial properties while assuring facile processing via dip coating or spray coating.

Introduction

Over the last decade metamaterials have received ever increasing attention [1]. Metamaterials are structures intentionally created applying nanoscopic building blocks at the mesoscale resulting in extraordinary properties not found in nature [2, 3].
The latest metamaterials referred to as 4.0 generation, increasingly amend physical methods by chemical concepts into their design to achieve functions beyond what can be achieved through traditional nanofabrication and engineering methods [4]. The metamaterials 4.0 benefit from surface modification, chemical tunability, and materials chemistry to trigger or enhance their response to external stimuli. They aim to overcome the limits set by conventional high precision, but difficult to scale, fabrication and should be compatible with more robust and affordable manufacturing approaches [5, 6].
Traditionally metamaterials focused on high-precision optical materials that can be subdivided into two categories based on their building blocks: plasmonic metasurfaces and dielectric metasurfaces [7]. Combining both categories for a synergistic performance in a facile and robust fashion imposes significant challenges [6]. Usually, this challenge is met by applying high vacuum technics like PVD, CVD, ALD, *etc*. [8-11]. Faster, better scalable, and more affordable protocols need to be established to allow for a widespread application of metasurfaces in everyday life. Such protocols will aim at wafer-scale growth and they might imply transfer of high-quality 2D materials to realize fabrication of metasurfaces in an industrially benign process [6, 12]. Involving assemblies of colloidal particles as building blocks in colloid-assisted lithography [13-15], represents a significant step in that direction but it still requires sophisticated conditions for nanoparticle assembly. The direct usage of colloidal suspensions requires a patterned substrate, whereupon deposition of the solution, particles are trapped in the pre-designed mold [16, 17]. This in turn limits the range of substrate types. More accessible methods rely on the direct assembly of metal nanoparticles, where the packaging density and particle concentration are controlled by polymer chains or ligands applied as placeholders keeping particles at distance [18-20].
We believe that sandwiching of nanoparticles (NP) between two large aspect ratio nanosheets (double stack, DS; Fig. 1g) could replace these placeholders while offering additional benefits: The large aspect ratio imparts an anisotropic nature and

[a] *Department of Chemistry and Bavarian Polymer Institute, University of Bayreuth, Universitätsstr. 30, 95440 Bayreuth, Germany*
* Corresponding author.

Electronic Supplementary Information (ESI) available: [details of any supplementary information available should be included here]. See DOI: 10.1039/x0xx00000x

liquid crystals (LC) of these DS are responsive to external magnetic or electric fields allowing for lasting orientation [21]. Merging functional nanoparticles with the liquid crystalline state opens new avenues for fabricating metamaterials based on a combination of the two features [22]. Suspensions of spherical NP will be isotropic but once being sandwiched, the LC feature of the encapsulating host will transduce its anisotropy to the metastructure [23, 24]. Moreover, the sandwich will improve the stability of nanoparticles, *e.g.* hamper Ostwald ripening and due to the large aspect ratio of the DS wet coating is straightforward [25-27]. On planar substrates the DS will moreover arrange coplanar to the surface and the anisotropy of the LC will thus be inherited by the coating.

Previously, we have shown that the collective magnetic response of the nanoparticles sandwiched between two hectorite nanosheets can be easily tuned by varying the ratio between components [24]. This in turn allows to modify the response times of the ferronematic suspension to magnetic fields. Those functionalized LC further were used for producing multi-response anisotropic hydrogels [28].

Recently Haechler and al.[29] have presented an antifogging metasurface based on a percolating ultrathin gold nanolayer placed between two dielectric layers of TiO_2. The three-layer laminate totalled to a thickness of 10 nm. Sputtering was applied for layer deposition. The layer of gold acts as a near-infrared (NIR) absorber transforming the NIR radiation into efficient anisotropic electric and phonic heat conduction, while preserving transparency in the visible range.

Here we present a wet colloid chemistry-based mimic to fabricate such a thin laminate coating. For this we prepare a liquid crystalline, electrostatically stabilized suspension of DS (Fig. 1f). DS are comprised by spherical gold nanoparticles (≈ 6 nm diameter) sandwiched between two dielectric 1 nm thick silicate nanosheets (Fig. 1g). The DS can then be self-assembled on a planar substrate in a defined orientation yielding anisotropic heat conductivity without the need of a patterned surface. The absorbance of the metasurface is tuneable by modulating the plasmonic coupling via a variation of NP loading. Thin and transparent coatings allow for a fast defogging and defrosting under NIR irradiation.

Results and discussion

Synthesis of a IR-absorbing nanosheet suspension

Synthetic sodium fluorohectorite (Na-hectorite, $[Na_{0.5}]^{inter}[Mg_{2.5}Li_{0.5}]^{oct}[Si_4]^{tet}O_{10}F_2$) belongs to a handful of layered compounds that show the rare phenomenon of thermodynamically driven, spontaneous delamination via 1D dissolution [30]. The highly-charged anionic nanosheets with a huge aspect ratio (≈ 20000 nm diameter, 1 nm thickness) [31] are separated to a uniform distance when immersed into deionized water [32, 33]. Even very dilute suspensions of such high aspect ratio nanosheets are not isotropic but represent nematic phases. For instance, at 0.3 wt% the separation of adjacent nanosheets amounts to a huge gap of ≈ 200 nm [34], which nevertheless is orders of magnitude smaller than the diameter and therefore rotation of individual nanosheets is hindered.

At this state, the dilute nematic phases of Na-hectorite can be loaded with nanoparticles like maghemite (γ-Fe_2O_3) [35] or palladium [36] carrying a positive surface charge in a quasi-ion exchange. Upon intercalation of the polycationic nanoparticles, the nematic structure collapses leading to an encapsulation of the nanoparticles.

1D dissolution critically depends on various entropic and enthalpic factors like ionic strength, hydration enthalpy of the interlayer cation or the distribution of them into inner and outer Helmholtz layers [30]. Therefore, by the choice of interlayer cation, it can be selectively activated or deactivated. Moreover, for synthetic hectorites characterized by a homogeneous charge density, partial ion exchange can be directed towards heterostructures, where in a strictly alternating periodicity ordered interstratifications are produced of interlayers that are activated and deactivated towards 1D dissolution (Fig. 1b) [31, 37-40].

The heterostructures can still be delaminated by immersing them into water. As every other interlayer is blocked from 1D dissolution, instead of monolayers, however, DS are obtained, where two silicate monolayers are glued together by a cation deactivating 1D dissolution (Fig. 1c). As the diameter of the DS still is huge compared to the separation even in dilute suspensions, the suspensions of DS also represent nematic liquid crystalline phases.

Here we partially ion exchange Na^+ for NH_4^+. As the latter is less hydrated, the two cations segregate into interlayers of different gallery height. As a 1D periodic arrangement of the two types of interlayers is favoured by the Madelung factor over a random arrangement, the segregation occurs in a strictly alternating fashion (Fig. 1b, and S4) [37]. During ion exchange, the ionic strength is at a level, where 1D dissolution of all types of interlayers is impeded. Once the ionic strength is lowered by repeated washing, eventually 1D dissolution sets in but it is restricted to the Na^+ interlayers producing the a nematic phase of DS with NH_4^+ acting as glue for two silicate layers (Fig. 1c). Depending on concentration adjacent DS are separated to tens of nanometers in the nematic suspension allowing for incorporation of nanoparticles with positive surface potential via a quasi-ion exchange (Fig. 1e). Upon incorporation of the polycationic nanoparticles, the nematic phases collapse by electrostatic attraction. As the individual nanosheets in the nematic suspension had been held in coplanar orientation, the collapse again produces heterostructures, where interlayers of nanoparticles and NH_4^+ alternate.

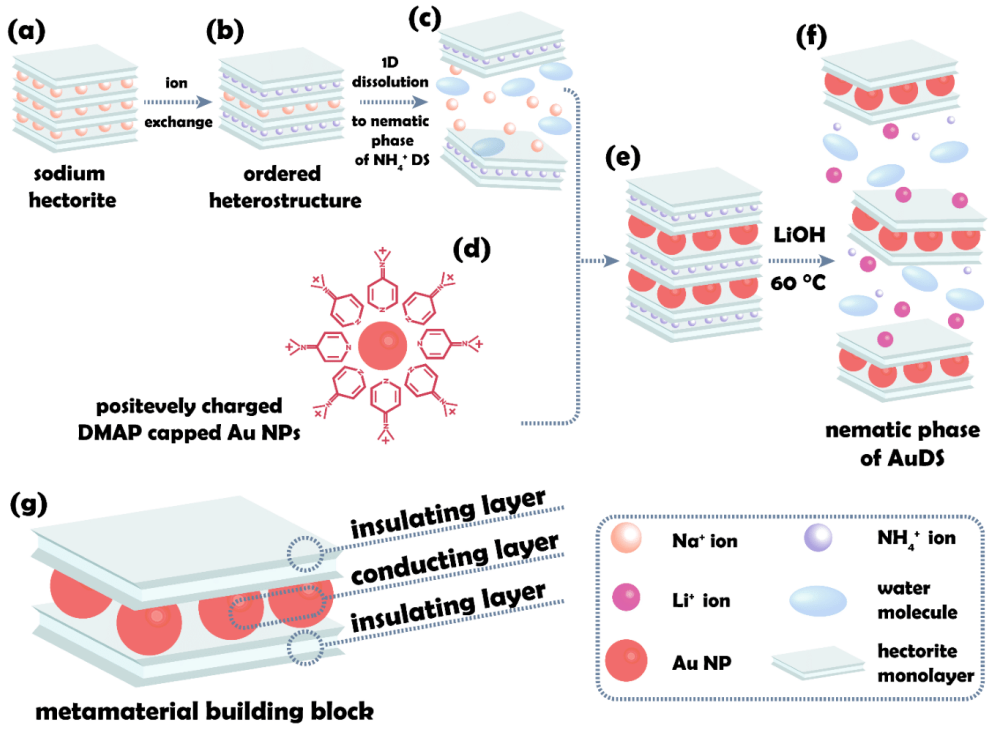

Figure 1. Synthesis of double stacks with Au nanoparticles sandwiched between hectorite monolayers (AuDS): **a** Pristine sodium hectorite with only sodium as the interlayer cation. **b** Partial ion exchange yields an ordered heterostructure of Na^+- and NH_4^+- occupied interlayers. Spontaneous delamination of the heterostructure by 1D dissolution yielding a nematic liquid crystalline suspension of NH_4^+-DS. **d** Monodisperse aqueous dispersion of positively charged DMAP capped Au NPs. **e** Intercalation of Au NPs between NH_4^+-DS separated to > 100 nm in the nematic phase. By hetero-coagulation ordered heterostructures of AuNP- and NH_4-occupied interlayers are obtained. **f** Cleavage of the heterostructure along the NH_4^+-occupied interlayers. Replacement of NH_4^+ by Li^+ activates the NH_4^+ interlayers for delamination by 1D dissolution producing a nematic suspension of AuDS. **g** Schematic representation of the nano/micro-metamaterial building block consisting of insulating hectorite monolayers sandwiching a light-absorbing layer of Au NPs.

The majority of established synthetic procedures yield negatively charged Au NPs. The capping ligand 4-dimethylaminopyridine (DMAP) was previously identified to yield Pd NPs [41] with positive ζ-potential. Direct synthesis of Au NPs applying this capping ligand, however, failed. Therefore, first negatively charged, citrate-capped Au NPs were synthesised (Fig. S1a) [42]. Spherical particles of 5.9 ± 1.1 nm in diameter as indicated by transmission electron microscopy (TEM) (Fig. S2a) were obtained. Because of the shell of solvated capping ligands, they appear slightly larger in dynamic light scattering measurement (DLS; 6.5±1 nm). Due to the anionic capping ligand, at pH 7 a ζ-potential of -31 mV was obtained (Fig. S2c and d, respectively). As a direct reversion of the sign of the ζ-potential from negative to positive values by replacement of the capping ligand is impossible in suspensions with high NP concentration, a two-step phase transfer was applied (Fig. S1b). The Au-citrate particles were transferred into a toluene phase using tetraoctylammonium bromide (TOAB) and back into water via 4-dimethylaminopyridine (DMAP) [43, 44]. This phase transfer reversed the value of the ζ-potential to +28 mV at pH 12.5 (Fig. S2d) without significantly affecting the size (6.5±0.9 nm by TEM and 7.9± 1.3 nm by DLS) (Fig. S2b and c, respectively) or polydispersity.

The now positively charged Au NPs could readily be intercalated between DS at the state of the nematic suspension (Fig. 1c). To achieve the incorporation of Au NPs, first, the pH of a 1 wt% aqueous dispersion of DS was adjusted to 12 with NaOH, and then it was quickly injected into a vigorously stirred Au NPs suspension (0.03 wt%). The volume of the Au NPs dispersion was varied to obtain the desired weight compositions. The large separation between individual DS (≈ 200 nm at 1 wt%) [34] allows for fast diffusion and incorporation of the positively charged Au NPs while triggering hetero-coagulation into dense heterostructures where NH_4^+ and Au NPs interlayers strictly alternate (Fig. 1e).

In the next step, we convert these hetero-coagulated aggregates into dispersed DS, where the Au NPs are sandwiched between two silicate layers. This is accomplished by slicing along the NH_4^+ interlayers, which requires the activation of these interlayers for 1D dissolution. This activation is achieved by ion

exchange of NH_4^+ for Li^+. As the selectivity of NH_4^+ for the interlayer site is higher than the one of Li^+, NH_4^+ needs to be deprotonated by LiOH (pH > 10.5 and slightly elevated temperatures (60 °C), moreover, help to remove NH_3 from the equilibrium by evaporation. At this point, Li^+ is exchanged into the former NH_4^+ interlayers but given the high ionic strength the Li^+ interlayers do not delaminate instantaneously. After repeated centrifugation and redispersion reducing the ionic strength, the ordered Li^+/Au NPs heterostructure eventually delaminates into a nematic suspension of gold intercalated DS (AuDS) where Au NPs are sandwiched between two silicate layers (Fig. 1f). The outer basal surfaces of individual AuDS nanosheets carry a diffuse double layer of Li^+ and are therefore electrostatically stabilized. The nematic suspensions of AuDS are therefore stable over months (Fig. 2a).

In the AuDS an IR absorbing NP layer is sandwiched between two dielectric insulating layers, similar to the physically deposited three layer laminate of Haechler et al. [29] of an ultrathin gold nanolayer placed between two dielectric layers of TiO_2 as mentioned in the introduction. One of the major differences to this published structure is the observation of plasmonic coupling. The loading of Au NPs is high enough to reduce the separation of the electrostatically repelling positive colloids to distances small enough to allow such coupling.

The composition of AuDS was determined using inductively coupled plasma atomic absorption spectroscopy (ICP-OES). We have prepared 3 sets of samples with low, moderate, and high wt% of Au NPs. The chemical compositions as indicated by ICP-OES were $(Au)_{0.12}Li_{0.31}(Mg_{2.5}Li_{0.5}Si_4O_{10}F_2)$, $(Au)_{0.68}Li_{0.31}(Mg_{2.5}Li_{0.5}Si_4O_{10}F_2)$, and $(Au)_{2.5}Li_{0.31}(Mg_{2.5}Li_{0.5}Si_4O_{10}F_2)$ for the samples with a nominal loading of 5 wt%, 30 wt%, and 60 wt% of Au NPs, respectively (referred to as AuDS 5, AuDS 30 and AuDS 60). Experimentally determined and nominal compositions are in close agreement indicating complete incorporation of all Au NPs offered in the quasi ion exchange (Table S1). This is further corroborated by clear supernatants obtained after centrifugation.

Impact of NPs distribution on localized surface plasmonic resonance

The variation in Au NPs loading influences the optical properties of the resulting nematic LC phases. The color changes from red to purple and finally to violet with increasing NPs content (Fig 2a, top) indicating a localized surface plasmonic resonance (LSPR) that varies with average Au NPs distance at different loading levels. Moreover, the intensity of the color changes substantially. Under cross-polarized light (Fig. 2a, bottom), all suspensions show the characteristic birefringence of a liquid crystalline state.

The absorption maxima of the UV-vis spectra (Fig.2b), attributed to the LSPR peak, show a red shift with increasing Au NPs loading (521, 531, 550 nm for AuDS 5, AuDS 30, and AuDS 60, respectively), which is a clear sign of changing electronic states of NP [45]. With the shifting of LSPR position, also the width of the peak changes. The original data was deconvoluted into two peaks (Fig.2c) attributed to different states of Au NPs in AuDS: isolated, when the distance between two neighbouring particles is too large so that interparticle interactions are negligible, and coupled, when NPs have a strong interparticle interaction [46]. For AuDS 5, isolated particles dominate the spectrum, with 95% of the total number of particles, while for AuDS 60,

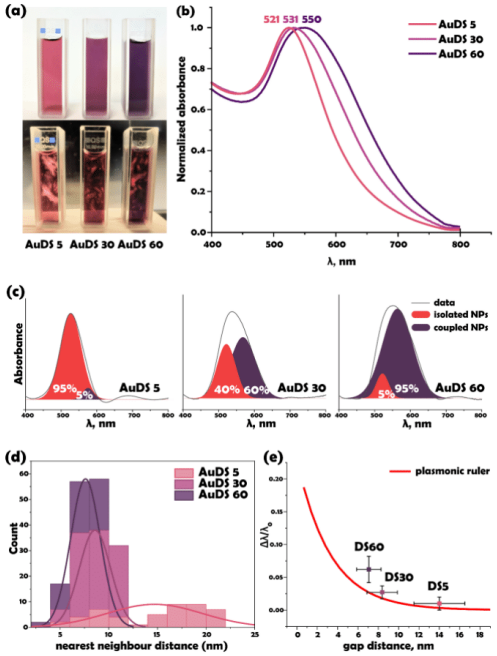

Figure 2. Plasmonic absorption of AuDS. a Aqueous liquid crystalline AuDS suspensions in daylight (top) and cross-polarised light (bottom) showing the birefringent nature. **b** UV-vis spectra of AuDS with different Au loadings showing a gradual red shift. **c** Deconvoluted UV-vis spectra of AuDS 5, AuDS 30 and AuDS 60. **d** Nearest neighbor distance as determined by TEM micrographs in AuDS 5, AuDS 30 and AuDS 60. **e** Shift of the plasmonic band by coupling in the AuDS 5, AuDS 30 and AuDS 60 as a function of nearest neighbour distance and plasmonic ruler in red.[47, 48]

95% of the nanoparticle population is in the coupled state. In this line, we can control the number of coupled particles (from 5% to 95% of the total number of NPs) and "freeze" an energetically unfavourable coupled state for intercalated particles.

To confirm this observation, we took top-view TEM micrographs of AuDS 5, AuDS 30, and AuDS 60 (Fig. S5) and extracted the average nearest neighbour distance between the NPs within the nanosheet. As the content of Au NPs within the nanosheet increases, the nearest neighbor distance decreases from roughly 14.2±2.5 nm for AuDS 5 to 8.4±1.5 nm for AuDS 30, and finally to 7.1±1.2 nm for AuDS 60 (Fig. 2d). The LSPR peak of Au NPs [46] was shown to depend on the interparticle spacing (i.e., the nearest neighbor distance) and can be measured using a so-called plasmonic ruler [47, 48]. This ruler was used to calculate the expected LSPR shift for our nearest neighbor distance using the formula (1).

Please do not adjust margins

$$\frac{\Delta\lambda}{\lambda 0} = ae^{-x/\tau}$$

Where λ_0 represents the LSPR peak position of a single Au NP sphere, $\Delta\lambda$ represents the shift in the LSPR peak positions of Au NPs, x represents the particle gap distance per particle diameter, *a* represents the particle coupling strength, and τ represents the decay constant. We applied τ = 0.47 and *a* = 0.23, which assumes an idealized hexagonal array of NPs and provides the best fit to the data [49]. The plasmonic ruler accurately describes the LSPR shift (Fig. 2e).

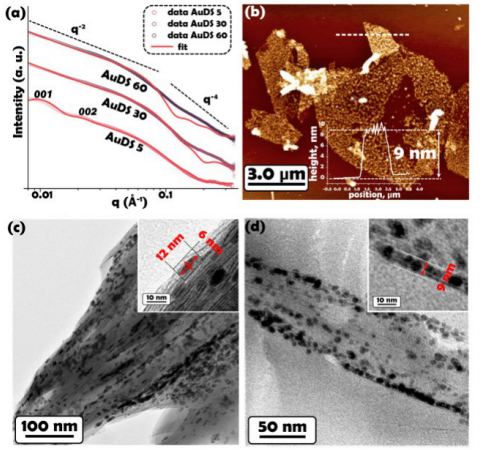

Figure 3. Structural characterisation of liquid crystalline suspensions and individual AuDS. a SAXS curves of AuDS 5, AuDS 30 and AuDS 60. **b** AFM of a AuDS 60, showing a thickness of 9 nm. **c** TEM image of a cross section of a restacked multilayer film of AuDS 60 dried without precaution showing a flattening of spherical Au NPs triggered by sample preparation. **d** TEM image of a cross section of AuDS 60 prepared by converting the aqueous dispersion into a hydrogel that then was freeze dried. This way the pristine spherical shape of Au NPs in the sandwich is preserved.

The distance between Au NPs in the hexagonal arrays as derived applying the plasmonic ruler, is, however, substantially smaller than the distance expected if the Au NPs concentration would be uniform throughout the sandwich. This indicates that in the AuDS domains with higher loadings coexist next to domains with lower loading showing no LSPR. This heterogeneity was already indicated by the deconvolution of the LSPR peaks. By variation of the total loading of AuDS the packaging density within the LSPR-domains may nevertheless be systematically tuned and by this the absorbance can be tuned.

Characterization of AuDS

AuDS are composed of the Au nanoparticles sandwiched between the two silicate monolayers; consequently, the SAXS pattern of AuDS LC will have form factors contribution from both lamellar DS nanosheets and spherical gold nanoparticles. Gold has, however, a substantially higher scattering length density (8.34×10^{-5} 1/Å^2) than hectorite (2.22×10^{-5} 1/Å^2) and therefore contributes more to the scattering even at low loading, which increases further at higher loading. To account for this different weighting, we fit the data applying a sum that reflects the appropriate weighting factors for the contribution of spherical and lamellar form factors.

AuDS 5 has the highest contribution of the lamellar form factor yielding very weak *00l peaks* (marked in Fig. 3a) due to a decently defined separation of AuDS in suspension. The *001* peak is observed at q = 0.012 Å^{-1} and indicates a separation of 54±3 nm between adjacent AuDS nanosheets at 4 wt%. As expected for nanosheets, in the range of intermediate q values (0.01 to 0.07 Å^{-1}) the intensity I(q) is proportional to q^{-2}, where q is the magnitude of the scattering vector and -2 is the exponent value characteristic of 2D scattering objects. At higher q values ranging from 0.07 to 0.11 Å^{-1} the intensity, however, decreases with the slope close to -4 as expected for a spherical scatterer.

SAXS patterns of AuDS 30 and AuDS 60 have a much higher contribution from scattering of spherical Au NPs. Unlike AuDS 5, for AuDS 30 and AuDS 60 the oscillations of the *00l* series are therefore no longer visible, while at intermediate q-values still a -2 scaling is observed. For AuDS 30 and AuDS 60 with the much increased weighting of the contribution of Au NPs to scattering, the slope at higher q-values (-3.1, -3.6 and -3.7 for AuDS 5, AuDS 30 and AuDS 60, respectively; Table S2) approaches the -4 value. In summary, the SAXS data thus confirm both the 2D nature of AuDS and the lamellar liquid crystalline nature of the suspensions with a higher contribution of the spherical form factor of Au NPs to the total scattering upon increasing loading of Au NPs.

AFM images (Fig. 3b) of individual AuDS 60 DS nanosheets gave a thickness of 9 nm, which is in good agreement with the sum of Au NP diameters (7 nm) and the thickness of 2 silicate monolayers (2 x 1 nm). Casting multilayer films of AuDS 60 and drying them allows for preparation of cross sections of self-standing films of restacked DS. TEM images of such cross sections (Fig. 3c) suggest that upon drying the spherical nanoparticles are strongly deformed to a more elliptical shape. Interestingly, concomitantly the color changes from red to blue (movie S1) during suspension drying. This LSPR is in line with elongated gold nanoparticles with an aspect ratio of 2 [50, 51]. This is indeed a typical aspect ratio observed in TEM images (Fig. 3c). As to the reason of this deformation we can only speculate. The elastic modulus of Au NPs of that size has been reported to be 1.3 GPa [52] as compared to 78 GPa [53] for bulk gold. We hypothesise that the pressure exerted by the electrostatic attraction of negatively charged hectorite layers and positively charged Au NPs in a dry, restacked film is sufficient to trigger the deformation.

In order to visualize the pristine AuDS, we therefore first mixed the suspension with acrylamide monomer followed by photopolymerisation. The hydrogels were then frozen and TEM samples were cut with a microtome before being freeze-dried. In this way, we minimize capillary stress, which might be another contribution to particle deformation. Comparing TEM images (Fig. 3d) of the AuDS 60 embedded in a gel corroborate that the elongation described above is clearly an artefact due to the sample preparation by drying without any precaution. In ac-

cordance with the optical spectra (Fig. 2b), the pristine AuDS indeed contain undeformed, spherical Au NPs. The deformation triggered by careless drying of films of AuDS is corroborated by a significant difference of thickness of AuDS observed in TEM images. For the gel embedded drying, we observed 9 nm (Fig. 3d, insert), which is in a good agreement with the AFM results (Fig. 3b). Upon deformation of the spherical Au NPs this shrinks substantially to 6 nm (Fig. 3c, insert).

Defogging metasurface

The enormous aspect ratio of AuDS will inevitably orient individual nanosheets parallel to a planar substrate of low roughness as for instance glass surfaces [54, 55]. Given the huge aspect ratio, preferred orientation is therefore given for free in a self-assembly. As most physical properties of AuDS will intrinsically be of 2D character, coatings fabricated from AuDS suspensions will thus be inherently anisotropic. Moreover, as the AuDS are only 9 nm, fabrication of thin coatings is straightforward, and the thickness may be controlled by the concentration and volume of the suspension applied and the processing method chosen. Finally, the AuDS carry a negative surface charge -44 mV (Fig. S2d) that facilitates robust bonding to substrates by electrostatic attraction.

Given the above features monolayer coatings of AuDS were prepared on glass substrates simply by dip coating into AuDS suspensions (0.01 wt%). As glass surfaces as well as AuDS carry a negative surface charge, the glass substrate was covered first with a layer of positively charged polymer – polyethylenimin (PEI, 0.1 wt %), followed by a monolayer of AuDS.

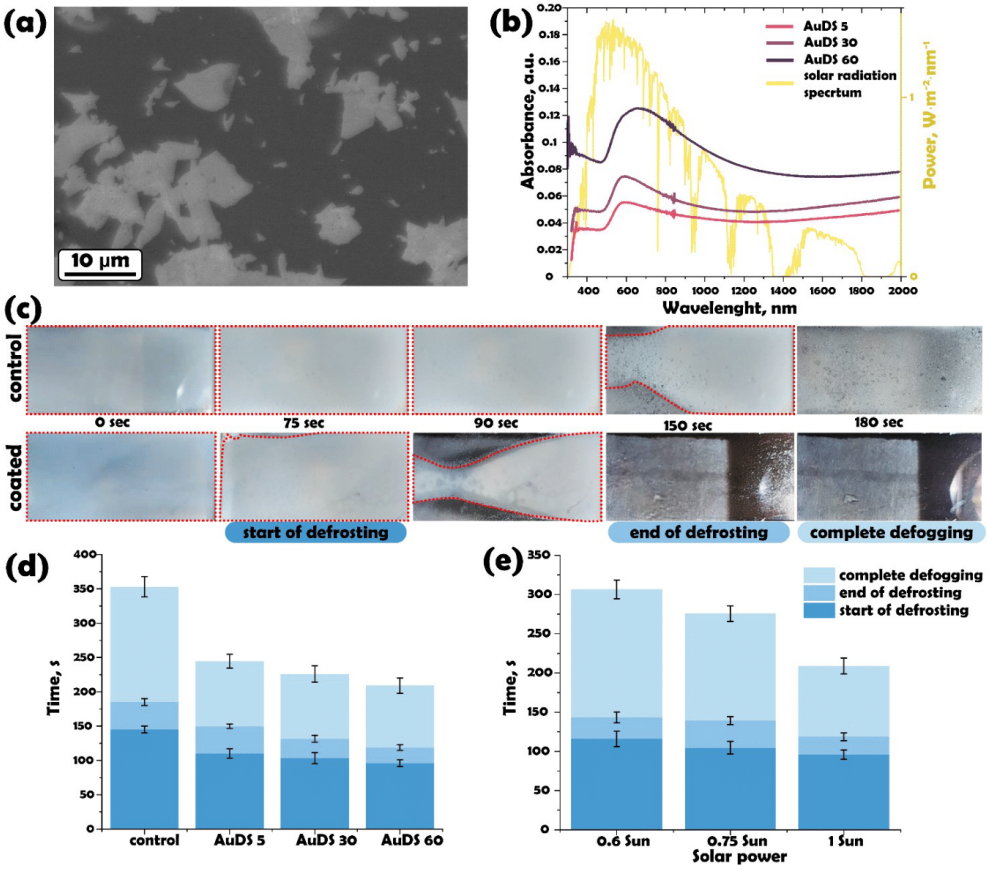

Figure 4. Defrosting and defogging performance of AuDS coated glass slides. **a** SEM image of the AuDS coated surface. SEM imaging suggests incomplete mostly monolayer coverage. **b** Absorbance spectra of AuDS coated metasurfaces. The solar spectrum is included for reference in yellow (ASTM G173-03 Reference Spectra). **c** Sequence of images following the defrosting and defogging of an uncoated and a AuDS 60 coated glass slide over time under 1 sun solar irradiation. **d** Time dependency histogram of defrosting and defogging for different AuDS coatings measured under 1 sun irradiation. **e** Time dependency histogram of defrosting and defogging for a AuDS 60 coated glass slide measured under different irradiation power.

SEM images of the coated glass suggest partial coverage of the substrate surface with a mostly monolayer coverage of AuDS (Fig.4a).

The thin coatings showed characteristic absorbance spectra resembling that of AuDS suspensions (Fig. 4b) but with significantly lower absorptivity. Because of the nanometre thickness of the coating, with naked eye the coated glass appears transparent despite some absorbance in the visible range (Fig. S7). The substantial absorption in the IR and NIR range of the solar spectrum, nevertheless, warrants efficient heating by sunlight. The heat is, moreover, transferred to the encompassing hectorite layers, which homogeneously spreads it over its large surface area due to its relatively high and anisotropic thermal conductivity [56-58], allowing the whole glass surface to heat up uniformly and efficiently.

As the absorption spectrum of AuDS is substantially red shifted with increasing Au NPs loading, higher loadings absorb stronger in the IR and NIR spectral region and therefore will heat up faster (Fig. 4b). The similarity of the spectra of coatings with the spectra measured in suspensions of AuDS, moreover, suggests that in monolayer coatings on glass slides deformation of spherical Au NPs as observed for dried multilayer coatings (Fig. 3c) does not occur.

The efficient and preferred absorption in the IR and NIR range may be applied for defrosting and defogging (Fig. S9). To demonstrate this, coated and uncoated glass slides were first immersed into liquid nitrogen to cool down to the temperature of 77K. After taking it out, it quickly formed a frosted layer of condensed water vapor on the surface. The glass slides were then illuminated with simulated solar radiation and the time required for complete defrosting and eventually defogging were recorded (Fig. 4d). The procedure was repeated 10 times for each sample and the average time was calculated. After 145±7 s, the uncoated glass surface started to defrost and defrosting was completed after 185±6 s. Water droplets of molten ice stayed on the surface until it completely evaporated (defogged) after 355±10s. Start, end of defrosting and complete defogging were converted into a color code in Fig. 4d facilitating a visual comparison with the coated samples.

All coated glass slides showed much faster defrosting and defogging (Fig.4d and movies S2 and S3). As expected, AuDS 60 with the most red shifted absorption spectrum performed best. Compared to the uncoated glass slide, the AuDS 60 coating substantially shortens the start of defrosting from 145±7 s to 96±5 s, the end of defrosting from 185±6 s to 120±4 s, and complete defogging ends to 210±8 instead of 355±10 s, representing an overall 60% reduction in required time.

A control coating with NH_4^+-DS (Fid. 1c) showed no effect on defogging time (Fig. S8a). The same applies to glass slides dip coated with suspensions of free Au NPs (0.03 wt%) not sandwiched in DS (Fig. S8a). As non-sandwiched Au NPs tend to aggregate on the glass surface, moreover, a patchy, non-uniform defogging pattern was observed of Au NPs coated glass slides (Fig. S6).

The type of coating technique seems to be irrelevant for the effect. Spray coating AuDS 60 suspensions on glass gave comparable defrosting and defogging performances to dip coated samples (Fig. S8b). This suggests that the coplanar orientation of AuDS on the substrate surface is achieved regardless of the application technique.

Not surprisingly, defrosting and defogging times decrease with photon flux. We tested power densities equivalent to 0.6, 0.75, and 1 sun illumination (600, 750, and 1000 W/m^2, respectively). For AuDS 60, the time to complete defogging is shortened from 305±12 s for 0.6, to 275±10 s for 0.75, and to 210±10 s for 1 sun (see Fig. 4d). A similar trend is observed for samples AuDS 30 and AuDS 5 (see Fig. S8c and d).

Experimental

Synthesis of sodium hectorite

Sodium hectorite ($[Na_{0.5}]^{inter}[Mg_{2.5}Li_{0.5}]^{oct}[Si_4]^{tet}O_{10}F_2$, Na-hectorite) was obtained by melt synthesis followed by long-term annealing according to a published procedure [31]. The material featured a cation exchange capacity (CEC) of 1.27 mmol/g and a density of 2.73 g/cm^3.

Synthesis of ordered heterostructures

Ordered heterostructures were synthesized according to a published procedure [37]. First, 1.5 g Na-hectorite was immersed in 250 ml of a water-ethanol mixture (75 vol% ethanol) for 12 h at room temperature in an overhead shaker. Then, 70.3 mg of NH_4Cl, corresponding to 69% of the CEC of Na-hectorite, were dissolved in 100 ml of a water-ethanol mixture (75 vol% ethanol) and added to the Na-hectorite under vigorous stirring followed by equilibration in the overhead shaker overnight at room temperature. The heterostructures was then washed five times with the same ethanol-water mixture and collected via centrifugation at 8000 rpm for 10 min. The ordered heterostructures is indicated by a rational superstructure *00l* series with a basal spacing of 23.0 Å. at 43 % relative humidity (Fig. S4). When immersed in deionized water the heterostructures delaminates into NH_4^+-DS and a birefringent gel is formed (Fig. 1c).

Synthesis of gold nanoparticles

Au NPs were synthesized according to a slightly modified published procedure [42]. 1 ml of 0.1875 M $HAuCl_4$ solution was injected into a 70 °C warm solution of 2.2 mM citric acid, 0.0125 mM tannic acid and 0.75 mM K_2CO_3 in 150 ml water (Fig. S1a).

For phase transfer 0.5 g of tetraoctylammonium bromide (TOAB) was dissolved in 50 ml of toluene. The citrate capped Au NPs suspension was added at room temperature to the TOAB solution and shacked intensively and then the aqueous phase was separated in a funnel. Next, the TOAB capped Au NPs suspended in toluene were washed several times with water and the aqueous phase was each time separated in a funnel.

For the phase transfer into water, 1.5 g of 4-dimethylaminopyridine (DMAP) was dissolved in 50 ml of deionized water and the pH was adjusted to 12.5 with NaOH solution. This DMAP solution was added to the TOAB capped Au NPs suspension in toluene and then left overnight without stirring (Fig. S1b) while the then DMAP capped Au NPs. Particles are transferred into the

aqueous phase. This is then separated applying a funnel and filtered through a polyester syringe filter with 0.2 µm pore size to remove potential aggregates.
$HAuCl_4$ (49%) was purchased from Alfa Aesar. Sodium citrate tribasic dehydrate (≥ 99 %), tannic acid, 4-(Dimethylamino)pyridine (≥ 99 %), tetraoctylammonium bromide (≥ 98 %), anhydrous toluene (≥ 99.8%) were purchased from Sigma-Aldrich. The water used was of MilliQ quality (18.2 MΩ).

Synthesis of Au double stacks

The delaminated suspensions (1 wt%) of NH_4^+-DS was adjusted to pH 12.5 with NaOH. Then this nematic suspension of DS was rapidly added to a dispersion of Au NPs (0.03 wt%) under stirring. Three different volumes of AuNP dispersions were used to vary the loadings (50 ml, 100 ml, and 150 ml for AuDS 5, AuDS 30 and AuDS 60, respectively). The flocculates were collected via centrifugation and washed several times by redispersing it into water. Then 400 ml of freshly prepared LiOH solution with a pH 10.5 was added to the flocculate, and the dispersion was mixed in an overhead shaker for 15 minutes. This procedure was repeated twice with fresh LiOH solution. Finally, the flocculate was transferred into an Erlenmeyer flask with 600 ml of LiOH (pH 10.5) and heated to 60°C over night under argon flow, whereupon a heterostructure with alternating AuNP loaded and Li^+ loaded interlayers is obtained. Reducing the ionic strength via washing several times with water eventually triggers delamination into nematic liquid crystalline suspensions of AuDS.

Powder X-ray diffraction measurements (PXRD)

Ordered interstratification were recorded on a Bragg-Brentano type diffractometer (Empyrean, PANalytical) with nickel filter and CuKα radiation (λ = 1.54187 Å).

Transmission electron microscopy (TEM)

TEM micrographs were taken with a JEOL JEM-2200FS field emission energy filtering transmission electron microscope (FE-EFTEM) at an acceleration voltage of 200 kV. A bottom-mounted CMOS camera system (OneView; Gatan) was used for recording zero-loss filtered micrographs (ΔE~0 eV). Micrographs were processed with DM 3.3 image processing software (Gatan). Au NPs only samples were prepared by simple drop-casting a dilute dispersion onto carbon-coated copper grids (Fig. S2). Two types of sample preparations were done for AuDS: 1. Dispersions were cast on glass slides and then dried ate 60 °C. Flakes were then pealed of the substrate, embedded in a polymer matrix before being cut with a Leica Ultramicrotome UC7+FC7. This type of sample preparation turned out to trigger a deformation of Au NPs. 2. To mitigate this drying artefact, the nematic AuDS suspensions (0.1wt%) were first transformed into a hydrogel by adding 10 wt% acrylamide monomer (AA) (Sigma-Aldrich). After addition of 0.1 mol% N,N-Methylenebisacrylamide (Sigma-Aldrich, 146072) as crosslinker and 1% wt% of 2-Hydroxy-4′-(2-hydroxyethoxy)-2-methylpropiophenone (Sigma-Aldrich 410896) as photoinitiator, the suspension was deoxygenated by purging it with argon and cast into a polydimethylsiloxane mold. Then photopolymerization was initiated with UV-light (302 nm wavelength). After polymerization, the hydrogel was frozen by immersing it into liquid nitrogen before being cut with the Leica Ultramikrotom UC7+FC7 equipped with a cryo-chamber. The slices were sandwiched between two copper grids and then freeze dried to remove the water from hydrogel.

Scanning electron microscopy (SEM)

SEM images were recorded using a ZEISS LEO 1530 (Carl Zeiss AG, Germany) operating at 3 kV.

Dynamic light scattering (DLS)

The particle size distribution of Au NPs was determined by DLS applying a Zetasizer Nano ZS (Malvern Panalytical). The same instrument was used to measure ζ-potentials.

Atomic force microscopy (AFM)

The surface topography was determined by atomic force microscopy. The images were acquired with a Dimension Icon (Bruker Nano Inc.) in PeakForce tapping mode in air. A ScanAsyst Air cantilever (Bruker Nano Inc.) with a typical spring constant of 0.4 N/m and a resonant frequency of 70 kHz was used. The PeakForce amplitude was 60 nm, and the PeakForce frequency was 2 kHz. The AFM images were processed with a NanoScope Analysis 1.80 (Bruker Nano Inc.). The topography was flattened by subtracting the first-order polynomial background using a threshold to exclude platelets from flattening. Platelet heights were determined using the "step tool" in NanoScope Analysis software. The samples for AFM were prepared by slow evaporation of a few drops of a diluted suspension (0.02 g/L) on a Si wafer under ambient conditions.

Inductively Couples Plasma Atomic Absorption Spectroscopy (ICP-AAS)

To determine the elemental composition, ≈ 20 mg of the samples were digested in an MLS 1200 Mega microwave digestion apparatus for 6.5 min at 600 W (MLS GmbH) after adding a mixture of 1.5 mL 30 wt% HCl (Merck), 0.5 mL of 85 wt% H_3PO_4 (Merck), 0.5 mL 65 wt% HNO_3 (Merck), and 1 mL of 48 wt% HBF_4 (Merck). The clear solution was then allowed to cool to room temperature, before being diluted to 100 mL and analyzed with a Varian Vista-Pro radial ICP-OES.

Small Angle X-ray Scattering (SAXS)

SAXS data were collected with a "Double Ganesha AIR" (SAXSLAB, Denmark). In this laboratory-based system, a microfocused X-ray beam is provided by a rotating copper anode (MicoMax 007HF, Rigaku Corporation, Japan). A position-sensitive detector (PILATUS 300 K, Dectris) was used in different positions to cover the full range of the scattering vectors q = 0.004–0.6 $Å^{-1}$. Before the measurement, the nanosheet suspensions were filled in 1 mm glass capillaries (Hilgenberg, code 4007610). The circularly averaged data were normalized to the incident beam, sample thickness, and measurement time.

UV-vis measurement

UV-Vis spectra were recorded by Cary 300 Scan spectrometer in quartz cuvettes (1 cm). Diluted dispersion of AuDS with concentration of 0.1 wt% (AuDS 5) or 0.01 wt% (AuDS 30 and AuDS 60)

were measured from 250 to 800 nm. IR spectroscopy was performed with a Cary 5000 spectrometer (Agilent Technologies, Germany) for the wavelength range from 300–2000 nm.

Spectra deconvolution

The UV-vis spectra were deconvoluted into two components: the contribution of individual nanoparticles and the contribution of plasmonically coupled nanoparticles. For the individual nanoparticle contribution, we used the fixed parameters extracted from spectrum of DMAP capped Au NPs suspensions (Fig. S3). The parameters of the plasmonically coupled component were then determined by the best fit with the overlayed spectrum using Fytik 1.3.1 [59].

Fabrication of metasurface

PEI (0.1 wt %) was dissolved in deionized water over night. AuDS dispersions were diluted to 0.01 wt%. Before deposition, glass slides were carefully cleaned by corona treatment (Zepto from Low-Pressure Plasma Systems). Then the substrates were rinsed with deionized water and ethanol, followed by drying with filtered air. The cleaned glass slides were then first dipped into the PEI solution for 5 min, rinsed with deionized water, and dried. Next the coatings were applied by an identical dipping, rinsing, and drying procedure with the different AuDS suspensions. For each coating, 10 individual samples were prepared.

Defrosting and defogging experiments

In a typical experiment the coated glass slide was placed on a polystyrene form for thermal insulation and then immersed into liquid nitrogen. After cooling equilibration at 77 K, the sample resting on the foam was placed under lamp simulating a solar spectrum (300-W Xenon arc lamp from LOT Quantum Design, AM1.5 filter, 1000 W m^{-2}) and the time count starts. The start and the end of defrosting and defogging processes was determined by the visual observation. Relative humidity was kept at 43 % and the ambient temperature was 21 C°.

Author Contributions

J.B., O.Kh., and V.D. conceived the project and designed the experiments. O.Kh. performed the synthesis and sample characterization. V.D. and S.R. assisted with the SAXS part of the manuscript. All authors read and contributed to the manuscript preparations.

Conflicts of interest

There are no conflicts to declare.

Conclusions

Sandwiching nanoparticles between nanosheets gives access to functional double stacks with an inherent anisotropic property portfolio. The loading and thus the average in-plane separation of nanoparticles may be varied to the limit where adjacent nanoparticles start communicating. In this line, for instance with gold nanoparticles the degree of plasmonic coupling may be tuned leading to a tuneable red shift of the absorbance spectra. With appreciable aspect ratio, nanometre thin, but laterally micron-sized 2D colloidal building blocks are obtained. The double stacks are consequently easy to be oriented on planar substrates resulting in highly anisotropic coatings. This opens an alternative avenue to nanometre thin coatings, which offers economic and technical advantages over established physical and chemical vapor deposition methods. The sandwiching host layers extend over large areas as compared to the nanoscopic guests. This allows for a combination of the best of two worlds: nanoscopic effects like plasmonic excitation and plasmonic coupling and a uniformity at the micro- and macro-range assured for instance by the thermal conductivity of the encompassing layers.

As a proof of principle, we here present the fabrication of metasurfaces via a water-based colloidal route applying gold nanoparticles sandwiched between two silicate monolayers. These metasurfaces allow for a fast and efficient defrosting and defogging of glass substrates. Plasmonic coupling at high nanoparticles loadings leads to a red shift of the absorption spectrum of double stacks that quickly and uniformly heats the glass surface by an efficient absorbance of IR and NIR radiation. As a consequence, defrosting and defogging can be substantially accelerated by a 9 nm coating of individual double stacks, which is not affecting the transparency of the glass substrate.

The approach can be transferred to most other functional nanoparticles that will benefit by the layered preorganization in the sandwich and that then can be applied as nanometre thin functional coatings on various substrates.

Acknowledgements

The authors acknowledge F. Puchtler for synthesizing the synthetic hectorite, M. Schwarzmann for electron microscopy images and ICP-OES analysis, and M. Thelen for AFM measurements. We appreciate the support of the Keylabs for Polymer Additives and Fillers, for Optical and Electron Microscopy, for Mesoscale Characterization: Scattering Techniques, and for Surface and Interface Characterization of the Bavarian Polymer Institute (BPI).

Notes and references

1. M. Kadic, G. W. Milton, M. van Hecke and M. Wegener, *Nat. Rev. Phys.*, 2019, **1**, 198–210.
2. D. R. Smith, J. B. Pendry and M. C. K. Wiltshire, *Science*, 2004, **305**, 788–792.
3. K. Sun, R. Fan, X. Zhang, Z. Zhang, Z. Shi, N. Wang, P. Xie, Z. Wang, G. Fan, H. Liu, C. Liu, T. Li, C. Yan and Z. Guo, *J. Mater. Chem. C*, 2018, **6**, 2925–2943.
4. C.-W. Qiu and T. W. Odom, *Chem. Rev.*, 2022, **122**, 14987–14989.
5. S. Y. Chou, P. R. Krauss and P. J. Renstrom, *Science*, 1996, **272**, 85–87.
6. J. Guan, J.-E. Park, S. Deng, M. J. H. Tan, J. Hu and T. W. Odom, *Chem. Rev.*, 2022, **122**, 15177–15203.

7. E. Cortés, F. J. Wendisch, L. Sortino, A. Mancini, S. Ezendam, S. Saris, L. de S. Menezes, A. Tittl, H. Ren and S. A. Maier, *Chem. Rev.*, 2022, **122**, 15082–15176.
8. Z. Chen, X. Wang, Y. Qi, S. Yang, J. A. N. T. Soares, B. A. Apgar, R. Gao, R. Xu, Y. Lee, X. Zhang, J. Yao and L. W. Martin, *ACS Nano*, 2016, **10**, 10237–10244.
9. J. L. Ocana-Pujol, L. Forster, R. Spolenak and H. Galinski, *Adv. Opt. Mater.*, 2022, **10**, 2201749.
10. K. J. Dorsey, T. G. Pearson, E. Esposito, S. Russell, B. Bircan, Y. Han, M. Z. Miskin, D. A. Muller, I. Cohen and P. L. McEuen, *Adv. Mater.*, 2019, **31**, 1901944.
11. F. Valmorra, G. Scalari, C. Maissen, W. Fu, C. Schönenberger, J. W. Choi, H. G. Park, M. Beck and J. Faist, *Nano Lett.*, 2013, **13**, 3193–3198.
12. L. Hüttenhofer, M. Golibrzuch, O. Bienek, F. J. Wendisch, R. Lin, M. Becherer, I. D. Sharp, S. A. Maier and E. Cortés, *Adv. Energy Mater.*, 2021, **11**, 2102877.
13. A. Nemiroski, M. Gonidec, J. M. Fox, P. Jean-Remy, E. Turnage and G. M. Whitesides, *ACS Nano*, 2014, **8**, 11061–11070.
14. B. Fuhrmann, H. S. Leipner, H.-R. Höche, L. Schubert, P. Werner and U. Gösele, *Nano Lett.*, 2005, **5**, 2524–2527.
15. V. Lotito and T. Zambelli, *Adv. Colloid Interface Sci.*, 2022, **299**, 102538.
16. P. Molet, N. Passarelli, L. A. Pérez, L. Scarabelli and A. Mihi, *Adv. Opt. Mater.*, 2021, **9**, 2100761.
17. C. Hanske, G. González-Rubio, C. Hamon, P. Formentín, E. Modin, A. Chuvilin, A. Guerrero-Martínez, L. F. Marsal and L. M. Liz-Marzán, *J. Phys. Chem. C*, 2017, **121**, 10899–10906.
18. M. J. Rozin, D. A. Rosen, T. J. Dill and A. R. Tao, *Nat. Commun.*, 2015, **6**, 1–7.
19. A. Tao, P. Sinsermsuksakul and P. Yang, *Nat. Nanotechnol.*, 2007, **2**, 435–440.
20. M. Mayer, M. J. Schnepf, T. A. F. König and A. Fery, *Adv. Opt. Mater.*, 2019, **7**, 1800564.
21. H. K. Bisoyi and Q. Li, *Chem. Rev.*, 2022, **122**, 4887–4926.
22. J. Uchida, B. Soberats, M. Gupta and T. Kato, *Adv. Mater.*, 2022, **34**, 2109063.
23. J. Müller, C. Sönnichsen, H. von Poschinger, G. von Plessen, T. A. Klar and J. Feldmann, *Appl. Phys. Lett.*, 2002, **81**, 171–173.
24. O. Khoruzhenko, D. R. Wagner, S. Mangelsen, M. Dulle, S. Förster, S. Rosenfeldt, V. Dudko, K. Ottermann, G. Papastavrou, W. Bensch and J. Breu, *J. Mater. Chem. C*, 2021, **9**, 12732–12740.
25. Y. J. Liu, G. Y. Si, E. S. P. Leong, N. Xiang, A. J. Danner and J. H. Teng, *Adv. Mater.*, 2012, **24**, OP131–OP135.
26. Q. L. Zhu, C. F. Dai, D. Wagner, M. Daab, W. Hong, J. Breu, Q. Zheng and Z. L. Wu, *Adv. Mater.*, 2020, **32**, 2005567.
27. Z. L. Wu, M. Moshe, J. Greener, H. Therien-Aubin, Z. Nie, E. Sharon and E. Kumacheva, *Nat. Commun.*, 2013, **4**, 1–7.
28. C. F. Dai, O. Khoruzhenko, C. Zhang, Q. L. Zhu, D. Jiao, M. Du, J. Breu, P. Zhao, Q. Zheng and Z. L. Wu, *Angew. Chem. Int. Ed.*, 2022, **61**, e202207272.
29. I. Haechler, N. Ferru, G. Schnoering, E. Mitridis, T. M. Schutzius and D. Poulikakos, *Nat. Nanotechnol.*, 2023, **18**, 137–144.
30. V. Dudko, O. Khoruzhenko, S. Weiß, M. Daab, P. Loch, W. Schwieger and J. Breu, *Adv. Mater. Technol.*, 2023, **8**, 2200553.
31. M. Stöter, D. A. Kunz, M. Schmidt, D. Hirsemann, H. Kalo, B. Putz, J. Senker and J. Breu, *Langmuir*, 2013, **29**, 1280–1285.
32. M. Daab, N. J. Eichstaedt, C. Habel, S. Rosenfeldt, H. Kalo, H. Schießling, S. Förster and J. Breu, *Langmuir*, 2018, **34**, 8215–8222.
33. M. Daab, N. J. Eichstaedt, A. Edenharter, S. Rosenfeldt and J. Breu, *RSC Adv.*, 2018, **8**, 28797–28803.
34. S. Rosenfeldt, M. Stöter, M. Schlenk, T. Martin, R. Q. Albuquerque, S. Förster and J. Breu, *Langmuir*, 2016, **32**, 10582–10588.
35. K. Ament, D. R. Wagner, F. E. Meij, F. E. Wagner and J. Breu, *Z. Anorg. Allg. Chem.*, 2020, **646**, 1110–1115.
36. K. Ament, N. Köwitsch, D. Hou, T. Götsch, J. Kröhnert, C. J. Heard, A. Trunschke, T. Lunkenbein, M. Armbrüster and J. Breu, *Angew. Chem. Int. Ed.*, 2021, **60**, 5890–5897.
37. M. Stöter, S. Gödrich, P. Feicht, S. Rosenfeldt, H. Thurn, J. W. Neubauer, M. Seuss, P. Lindner, H. Kalo, M. Möller, A. Fery, S. Förster, G. Papastavrou and J. Breu, *Angew. Chem.*, 2016, **128**, 7524–7528.
38. M. Stöter, B. Biersack, S. Rosenfeldt, M. J. Leitl, H. Kalo, R. Schobert, H. Yersin, G. A. Ozin, S. Förster and J. Breu, *Angew. Chem. Int. Ed.*, 2015, **54**, 4963–4967.
39. M. Matejdes, M. Stöter, R. Czerwieniec, M. Leitl, S. Rosenfeldt, T. Schumacher, J. Albert, M. Lippitz, H. Yersin and J. Breu, *Adv. Opt. Mater.*, 2021, **9**, 2100516.
40. P. H. Michels-Brito, V. Dudko, D. Wagner, P. Markus, G. Papastavrou, L. Michels, J. Breu and J. O. Fossum, *Sci. Adv.*, 2022, **8**, eabl8147.
41. K. Ament, N. Köwitsch, D. Hou, T. Götsch, J. Kröhnert, C. J. Heard, A. Trunschke, T. Lunkenbein, M. Armbrüster and J. Breu, *Angew. Chem. Int. Ed.*, 2020, **n/a**.
42. J. Piella, N. G. Bastús and V. Puntes, *Chem. Mater.*, 2016, **28**, 1066–1075.
43. V. J. Gandubert and R. B. Lennox, *Langmuir*, 2005, **21**, 6532–6539.
44. D. I. Gittins and F. Caruso, *Angew. Chem. Int. Ed.*, 2001, **40**, 3001–3004.
45. V. Amendola, R. Pilot, M. Frasconi, O. M. Maragò and M. A. Iatì, *J. Phys.: Condens. Matter*, 2017, **29**, 203002.
46. A. Choudhary, G. Singh and A. M. Biradar, *Nanoscale*, 2014, **6**, 7743–7756.
47. R. T. Hill, J. J. Mock, A. Hucknall, S. D. Wolter, N. M. Jokerst, D. R. Smith and A. Chilkoti, *ACS Nano*, 2012, **6**, 9237–9246.
48. X. Ben and H. S. Park, *J. Phys. Chem. C*, 2011, **115**, 15915–15926.
49. E. J. Robertson and C. Tran Minh, *Langmuir*, 2022, **38**, 13206–13216.
50. R. Kumar, L. Binetti, T. H. Nguyen, L. S. M. Alwis, A. Agrawal, T. Sun and K. T. V. Grattan, *Sci. Rep.*, 2019, **9**, 1–10.
51. X. Ye, L. Jin, H. Caglayan, J. Chen, G. Xing, C. Zheng, V. Doan-Nguyen, Y. Kang, N. Engheta, C. R. Kagan and C. B. Murray, *ACS Nano*, 2012, **6**, 2804–2817.
52. H. P. Wampler and A. Ivanisevic, *Micron*, 2009, **40**, 444–448.
53. L. Sun, R. Riedel, S. G. Stanciu, F. Yang, N. Hampp, L. Xu and A. Wu, *J. Mater. Chem. B*, 2018, **6**, 2960–2971.
54. M. Schlenk, E. Hofmann, S. Seibt, S. Rosenfeldt, L. Schrack, M. Drechsler, A. Rothkirch, W. Ohm, J. Breu, S. Gekle and S. Förster, *Langmuir*, 2018, **34**, 4843–4851.

55. M. Röhrl, J. H. Mettke, S. Rosenfeldt, H. Schmalz, U. Mansfeld, R. L. Timmins, C. Habel, J. Breu and F. Durst, *J. Coat. Technol. Res.*, 2022, **19**, 487–495.
56. T. Dörres, M. Bartkiewicz, K. Herrmann, M. Schöttle, D. Wagner, Z. Wang, O. Ikkala, M. Retsch, G. Fytas and J. Breu, *ACS Appl. Nano Mater.*, 2022, **5**, 4119–4129.
57. A. Philipp, P. Hummel, T. Schilling, P. Feicht, S. Rosenfeldt, M. Ertl, M. Schöttle, A. M. Lechner, Z. Xu, C. Gao, J. Breu and M. Retsch, *ACS Appl. Mater. Interfaces*, 2020, **12**, 18785–18791.
58. Z. Wang, K. Rolle, T. Schilling, P. Hummel, A. Philipp, B. A. F. Kopera, A. M. Lechner, M. Retsch, J. Breu and G. Fytas, *Angew. Chem. Int. Ed.*, 2020, **59**, 1286–1294.
59. M. Wojdyr, *J. Appl. Crystallogr.*, 2010, **43**, 1126–1128.

SUPPORTING INFORMATION

Title: Fabricating defogging metasurfaces via a water-based colloidal route

Author(s): Olena Khoruzhenko, Volodymyr Dudko, Sabine Rosenfeldt and Josef Breu*

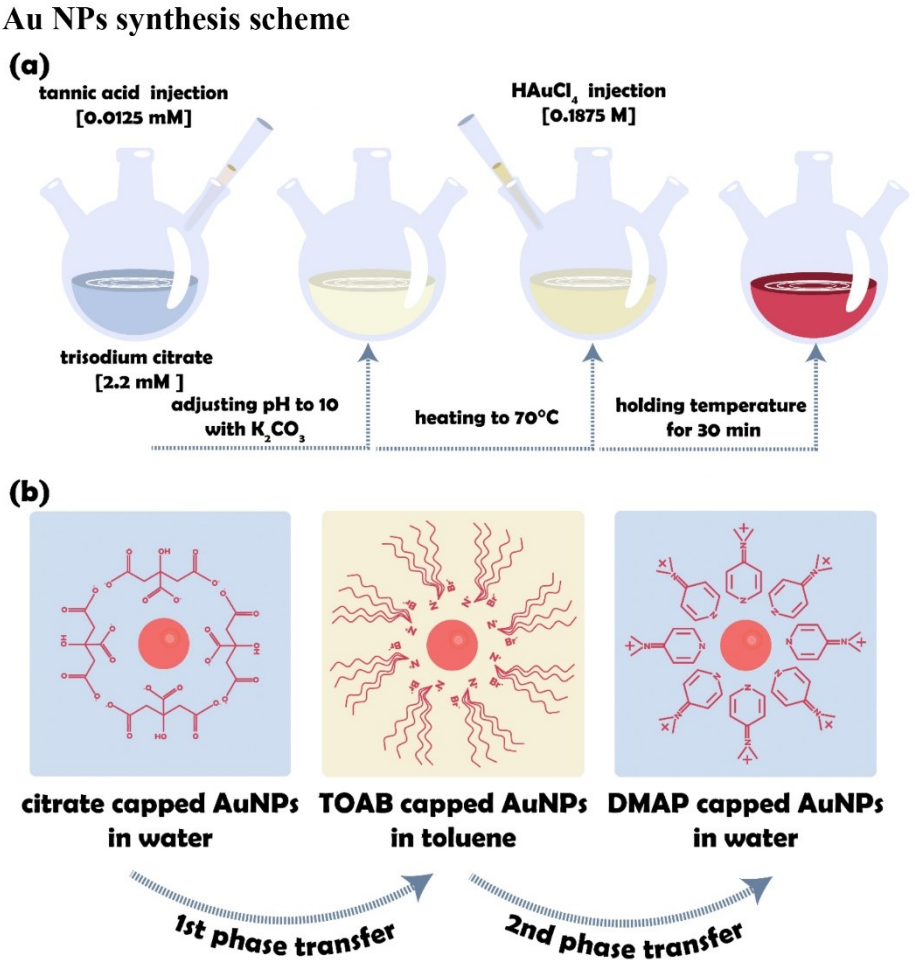

Figure S1. Scheme of Au NPs synthesis. **a** Step by step scheme of citrate capped Au NPs synthesis. **b** Two steps phase transfer of Au NPs into organic and back to aqueous phases DMAP capped Au NPs.

Size distribution and zeta potential measurments

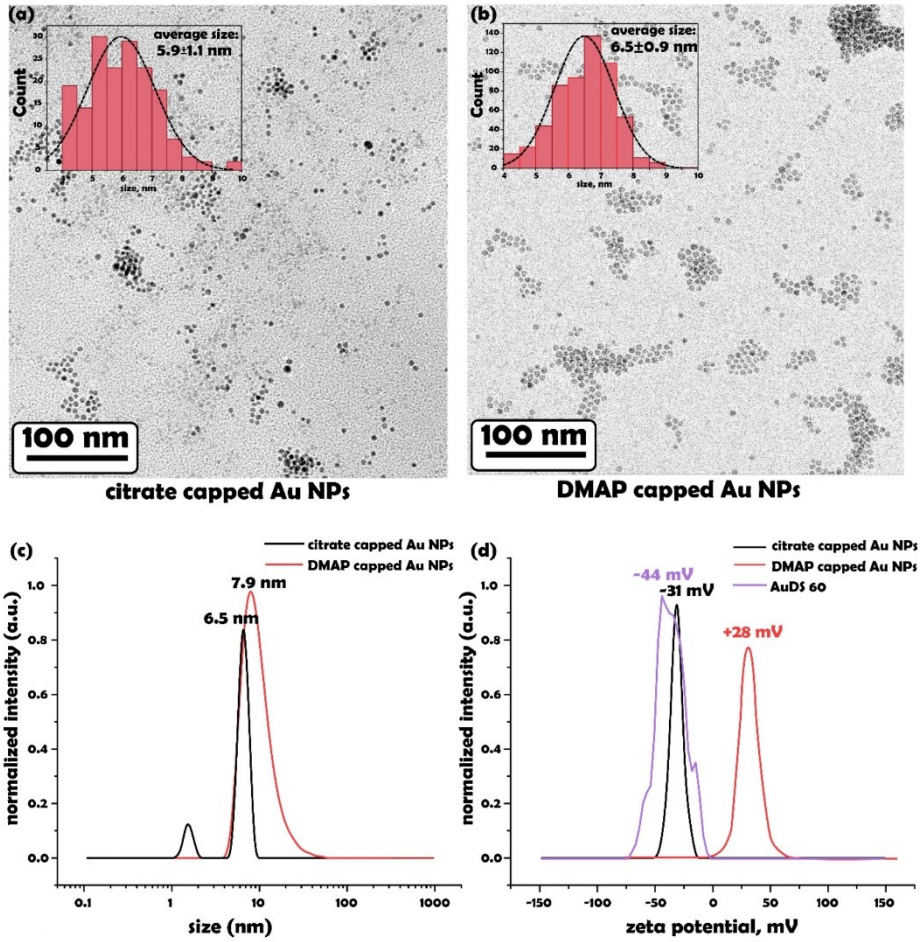

Figure S2. Size and charge characterization of nanomaterials. **a** TEM image of citrate capped Au NPs. Inserted histogram of the diameter distribution of 150 particles. **b** TEM image of DMAP capped AuNPs. Inserted histogram of the diameter distribution of 400 particles. **c** Hydrodynamic diameter according to DLS measurement. **d** Zeta potential for citrate capped Au NPs, for AuDS 60 at pH 7, and for DMAP capped Au NPs at pH 12.5.

UV-Vis spectra of Au NPs

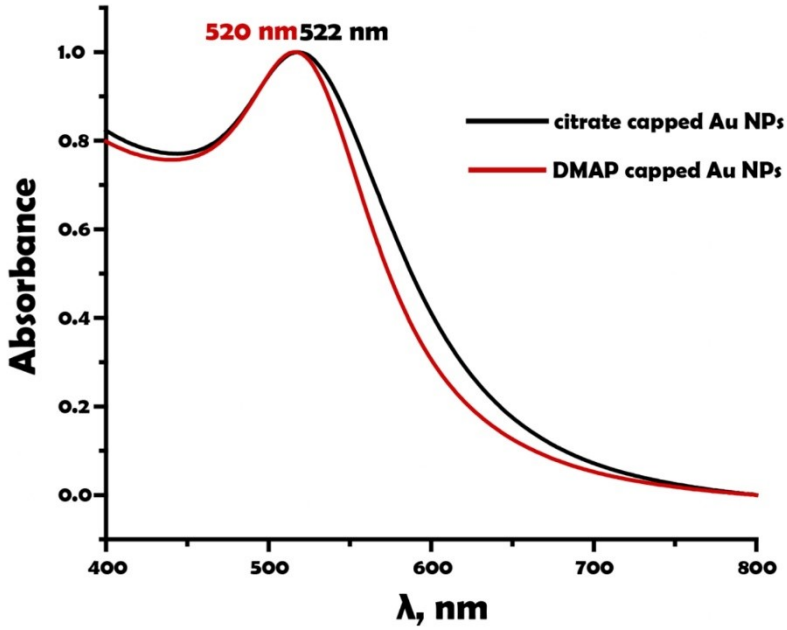

Figure S3. Characteristic UV-Vis spectra for aqueous suspensions of citrate and DMAP capped Au NPs and LSPR peaks positions.

XRD pattern of NH_4^+/Na^+ ordered heterostructures

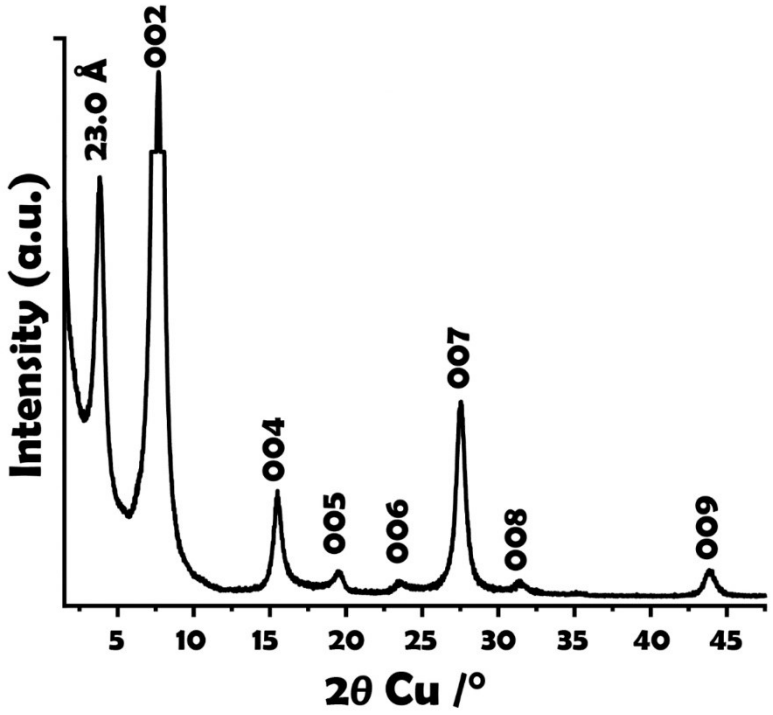

Figure S4. PXRD of the ordered interstratification of strictly alternating Na^+ and NH_4^+ layers in synthetic hectorite. The sample was equilibrated in an atmosphere with 43% relative humidity.

ICP-OES

Table S1. Elemental composition according to ICP-OES.

Element	**Weight fraction of the element [%]**		
Nominal Au	*5 wt%*	*30 wt%*	*60 wt%*
Au	6	25	57
Mg	15.3	12.3	7
Nominal Formula[a]	**$(Au)_{0.12}$ $Li_{0.31}(Mg_{2.5}Li_{0.5}Si_4O_{10}F_2)$**	**$(Au)_{0.68}$ $Li_{0.31}(Mg_{2.5}Li_{0.5}Si_4O_{10}F_2)$**	**$(Au)_{2.5}$ $Li_{0.31}(Mg_{2.5}Li_{0.5}Si_4O_{10}F_2)$**

[a]The nominal formula was calculated to be $(Au)_x$ $Li_{0.31}(Mg_{2.5}Li_{0.5}Si_4O_{10}F_2)$. Si was not detected directly via ICP-AAS. The amount of Si was rather calculated assuming the atomic ratio of Mg to Si of 2.5:4 as required by the hectorite-composition.

SAXS modelling

To fit SAXS curves, a linear combination of a spherical model[1] (sphere) and lamellar stack[2] with appropriate weighted factors accounting for the varying volume ratios of the constituents (hectorite and Au NPs) was applied.

I(q)=scale*(A*sphere+B*lammelar) + background

Table S2. Model parameters of SAXS fitting

Parameter	AuDS 5	AuDS 30	AuDS 60	Physical meaning
Scale	0.003	0.0011	0.000878	Source intensity
Background	0.015	0.0044	0.01	Source background
A	0.002	0.026	0.0544	Weighted factor of nanoparticle
Scattering length density	$83.4*10^{-6}Å^{-2}$	$83.4*10^{-6}Å^{-2}$	$83.4*10^{-6}Å^{-2}$	nanoparticles scattering length density
Radius	35.8 Å	35	38.5	Radius of nanoparticle
B	2.8	0.6933	1.1669	Weighted factor of nanosheets
Scattering length density	$22.2*10^{-6}Å^{-2}$	$22.2*10^{-6}Å^{-2}$	$22.2*10^{-6}Å^{-2}$	nanosheets scattering length density
Thickness	24.4 Å	33	44.3	Thickness of nanosheet
Spacing	530 Å	None	None	Separation between nanosheets

Please note that the contribution of the Au NPs to the total scattering increases due to the larger weighting factor of the spherical scatterer concomitantly with the increasing loading of Au NPs amounting to 0.7, 5.5 and 16.8 vol% for AuDS 5, AuDS 30 and AuDS 60 respectively. Additionally, the apparent thickness of the double stacks increases.

Top-view TEM images of AuDS

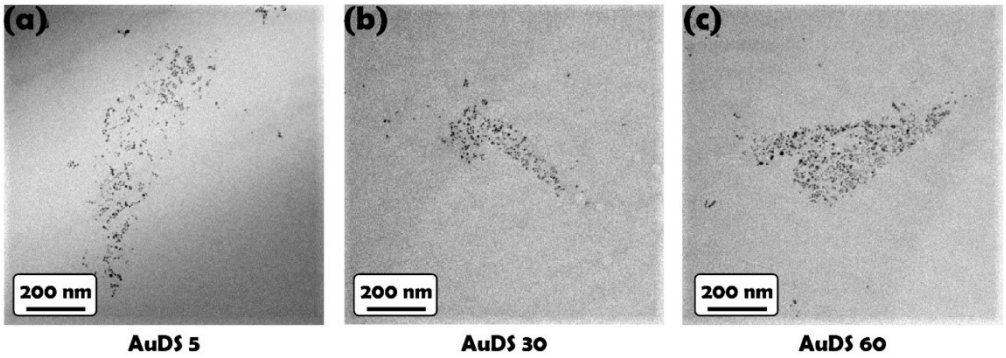

Figure S5. TEM images of AuDS with different Au NPs loading used for determining the interparticle distance. **a** Top-view TEM image of AuDS 5. **b** Top-view TEM image of AuDS 30. **c** Top-view TEM image of AuDS 60

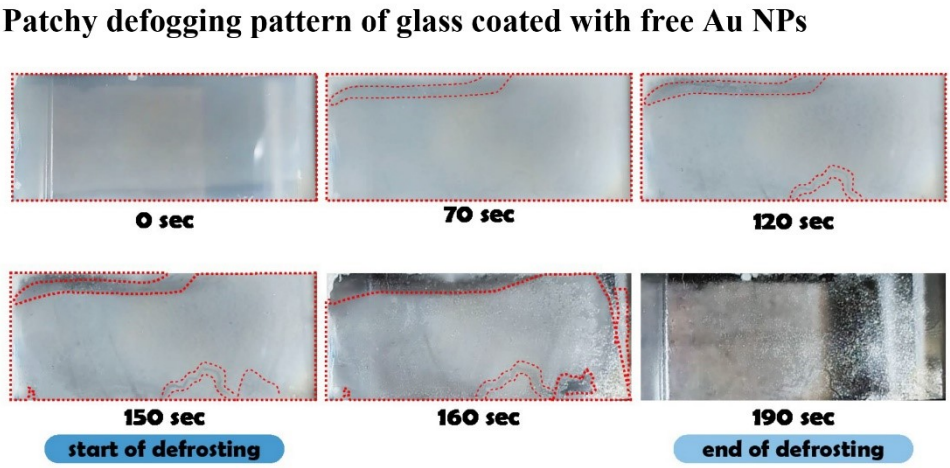

Figure S6. Sequence of images following the defrosting of a glass slide coated with DMAP capped Au NPs over time under 1 sun solar irradiation shows the patchy character of defogging pattern.

Photos of samples

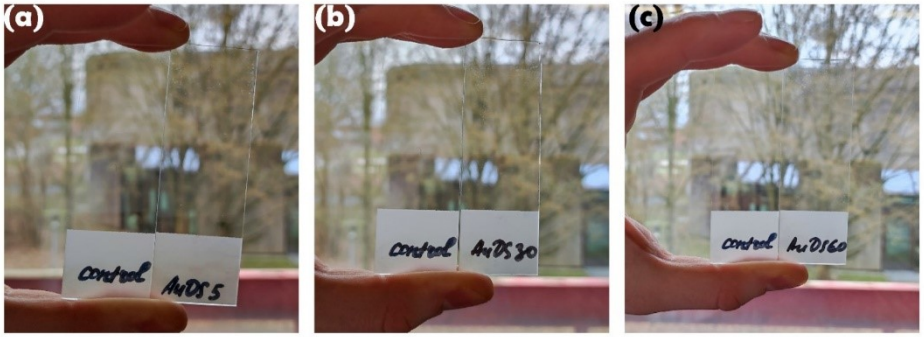

Figure S7. Comparison of transparency of an uncoated glass slide (left) and samples with applied metasurface (right) fabricated by dip coating showing the high transparency of the coating. **a** AuDS 5. **b** AuDS 30. **c** AuDS 60.

Defogging and defrosting tests

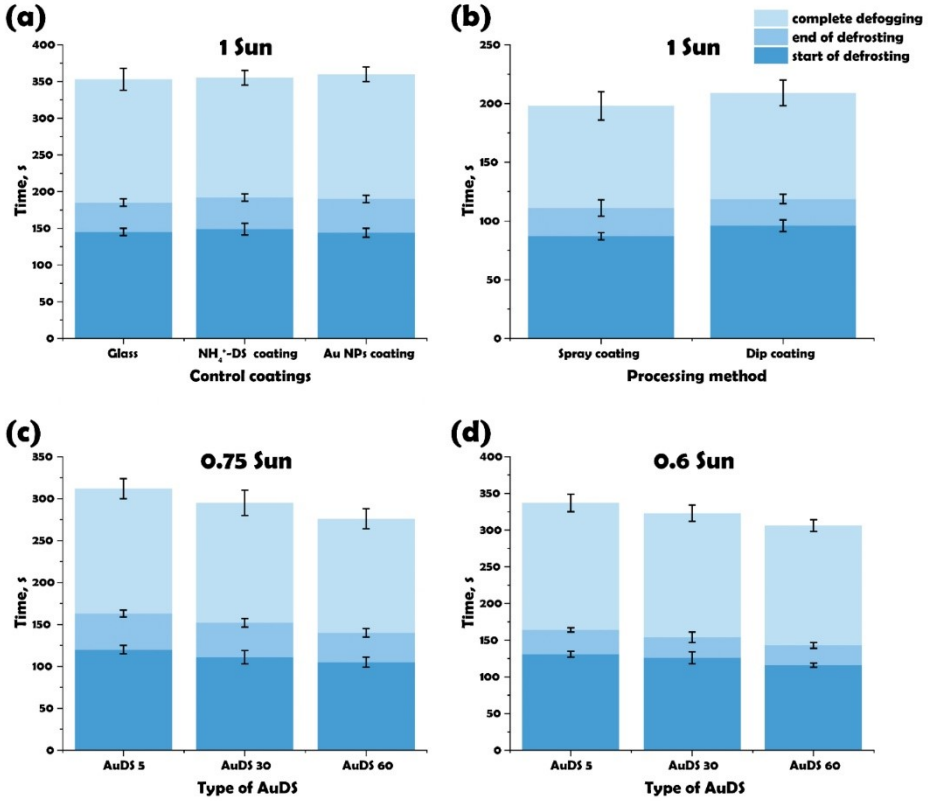

Figure S8. Defogging and defrosting tests. **a** Time dependency histogram of defogging for uncoated glass, glass coated with NH_4^+-DS and glass coated with free DMAP capped Au NPs. **b** Time dependency histogram comparing different coating methods of AuDS 60 coated glass slides. **c** Time dependency histogram of defogging measured under 0.75 sun irradiation. **d** Time dependency histogram of defogging measured under 0.6 sun irradiation.

References:

1. A. Guinier, G. Fournet, C. B. Walker and G. Vineyard, *Phys. Today*, 1956.
2. F. Nallet, R. Laversanne and D. Roux, *J. Phys. II*, 1993, **3**, 487–502.

LIST OF PUBLICATIONS AND CONFERENCES

Publications and Manuscripts

Publication and Manuscripts used in the dissertation

- Khoruzhenko, O., Wagner, D. R., Mangelsen, S., Dulle, M., Förster, S., Rosenfeldt, S., ...Breu, J. (2021). Colloidally stable, magnetoresponsive liquid crystals based on clay nanosheets. J. Mater. Chem. C, 9(37), 12732–12740. doi: 10.1039/D1TC02927D
- Dai, C. F., Khoruzhenko, O., Zhang, C., Zhu, Q. L., Jiao, D., Du, M., ...Wu, Z. L. (2022). Magneto-Orientation of Magnetic Double Stacks for Patterned Anisotropic Hydrogels with Multiple Responses and Modulable Motions. Angew. Chem. Int. Ed., 61(35), e202207272. doi: 10.1002/anie.202207272
- Khoruzhenko, O., Dudko, V., Rosenfeldt, S., Breu, J., Fabricating defogging metasurfaces via a water-based colloidal route (2023) Submitted to Material horizons.

Other manuscripts I participated

- Dudko, V., Khoruzhenko, O., Weiß, S., Daab, M., Loch, P., Schwieger, W., & Breu, J. (2023). Repulsive Osmotic Delamination: 1D Dissolution of 2D Materials. Adv. Mater. Technol., 8(3), 2200553. doi: 10.1002/admt.202200553
- Dudko, V., Timmins, R. L., Khoruzhenko, O., Röhrl, M., Greve, C., Rosenfeldt, S., ...Breu, J. (2022). Spontaneous delamination of affordable natural vermiculite as a high barrier filler for biodegradable food packaging. Mater. Adv., 3(24), 9052–9062. doi: 10.1039/D2MA00734G
- Zhu, Q. L., Dai, C. F., Wagner, D., Khoruzhenko, O., Hong, W., Breu, J., ...Wu, Z. L. (2021). Patterned Electrode Assisted One-Step Fabrication of Biomimetic Morphing Hydrogels with Sophisticated Anisotropic Structures. Adv. Sci., 8(24), 2102353. doi: 10.1002/advs.202102353
- Liang, C., Dudko, V., Khoruzhenko, O., Hong, X., Zhong-Peng Lv , Breu, J., Zhang, H., Ikkala, O., Stiff and self-healing hydrogels by polymer entanglements in co-planar nanoconfinement, (2023) Submitted to Nature

ACKNOWLEDGMENTS

I would like to express my deepest gratitude to all people without whom this work would never see this world. The ICE^2 team (former AC1) at Bayreuth University, especially my supervisor – Prof. Dr. Josef Breu, who always showed a great belief in me, gave freedom to grow as a scientist, a chance to work on very exciting topics and develop myself in artistic vector at the same time.

I would like to express my deepest appreciation to all collaborators, especially the Aalto University team, who inspired me with the highest quality of scientific research, openness to discussions, and great support. I am very grateful to you Hang Zhang, Chen Liang, and Prof. Dr. Olli Ikkala.

Special thanks to Prof. Dr. Liang Wu and his team – our collaboration taught me a lot and enriched my scientific worldview. Additionally, I would like to thank Sabine Rosenfeldt for the SAXS expertise.

Thanks should also go to our technical fairies – Marco Schwarzmann and Florian Puchtler. Without you, any research cannot happen in this chair.

I had the pleasure to share the working space with kind and friendly people – thank you, Michael Thelen, Lukas Federer, and Daniel Friedrich for the warm atmosphere.

All the people who were there for me during that stormy times – Renee Timmins, Gihoon Cha, Marian Matjedes.

Finally, from the bottom of my heart, thanks to my husband Volodymyr, my beloved parents, and my dear sister Olha. I would like to extend my sincere thanks to very dear friends – Daryna Diment and Sebastian Weiß. Your support made me believe I can conquer that mountain.

(Eidesstattliche) Versicherungen und Erklärungen

(§ 8 Satz 2 Nr. 3 PromO Fakultät)

Hiermit versichere ich eidesstattlich, dass ich die Arbeit selbstständig verfasst und keine anderen als die von mir angegebenen Quellen und Hilfsmittel benutzt habe (vgl. Art. 64 Abs. 1 Satz 6 BayHSchG).

(§ 8 Satz 2 Nr. 3 PromO Fakultät)

Hiermit erkläre ich, dass ich die Dissertation nicht bereits zur Erlangung eines akademischen Grades eingereicht habe und dass ich nicht bereits diese oder eine gleichartige Doktorprüfung endgültig nicht bestanden habe.

(§ 8 Satz 2 Nr. 4 PromO Fakultät)

Hiermit erkläre ich, dass ich Hilfe von gewerblichen Promotionsberatern bzw. -vermittlern oder ähnlichen Dienstleistern weder bisher in Anspruch genommen habe noch künftig in Anspruch nehmen werde.

(§ 8 Satz 2 Nr. 7 PromO Fakultät)

Hiermit erkläre ich mein Einverständnis, dass die elektronische Fassung meiner Dissertation unter Wahrung meiner Urheberrechte und des Datenschutzes einer gesonderten Überprüfung unterzogen werden kann.

(§ 8 Satz 2 Nr. 8 PromO Fakultät)

Hiermit erkläre ich mein Einverständnis, dass bei Verdacht wissenschaftlichen Fehlverhaltens Ermittlungen durch universitätsinterne Organe der wissenschaftlichen Selbstkontrolle stattfinden können.

…….

Ort, Datum, Unterschrift